THE EVOLUTION AND PULSATION OF CRYSTALLIZING WHITE DWARF STARS

by

MICHAEL HOUSTON MONTGOMERY, B.S., M.A.

DISSERTATION

Presented to the Faculty of the Graduate School of

The University of Texas at Austin

in Partial Fulfillment

of the Requirements

for the Degree of

DOCTOR OF PHILOSOPHY

THE UNIVERSITY OF TEXAS AT AUSTIN

December 2000

THE EVOLUTION AND PULSATION OF CRYSTALLIZING WHITE DWARF STARS

APPROVED BY
DISSERTATION COMMITTEE:

Supervisor: ____________________

Acknowledgements

I would like to thank Don and Ed for providing the environment and atmosphere of the WET lab. Their open approach to doing science is a model which others would do well to follow. From Ed I have learned the difference between models and reality, which I continually try not to forget. From Don I have learned how to have ideas and how to develop them, and that sometimes the craziest ideas are the best. The rest of my committee, Ethan, Craig, and Carl, have also been a valuable source of ideas and advice.

The students in the WET lab, both past and present, are equally responsible for the productivity of the group. Paul Bradley and Matt Wood have both made valuable contributions to my education, as well as to the calculations in this thesis. They each deserve the title of "honorary Ph.D. committee member." Steve Kawaler also provided me with useful advice regarding the white dwarf evolution code, and evolution codes in general.

The former students which I had significant overlap with while they were still at Texas are Judi, Chuck, Chris, Scot, and Antônio, all of whom have helped me and all of whom continue to be active in the field. Scot in particular has helped me understand the nature of the observations and of the stars themselves, even though we still have more questions than answers in that regard. He also taught me the basics of system administration on Unix machines, although my understanding of the inner workings of these systems is still fairly rudimentary. Antônio and I have had dozens of discussions ranging from the observations to the theory to the instrumentation (gasp). He is not content with the simple pat answers, but must actually *understand*. Consequently, it took hours to answer some of his questions, during which time I went from confidence to doubt and despair and finally to a renewed and better understanding of the problem. Of course, sometimes we started not knowing the answer and matters only got worse. But in the end, we were *certain* that we did not know!

Atsuko and I joined the lab at the same time and were two of the most junior graduate students for many years. She has made the lab a better and a brighter place not just for me, but for everyone else. Now that we are the "senior" graduate students, we are agreed upon one thing: it's no good being senior if there aren't junior students around to do the work!

Eric did his second-year project as part of our group. In fact, the work on phase separation in Chapter 2 of this thesis is an extension of his Master's thesis. He has continued to be a collaborator and a good friend, and I hope that our friendship can continue to grow in the future.

Travis is the most recent addition to the WET group. He has helped me with many computer-related problems and he promises to bring more modern computational techniques to the process of white dwarf model fitting.

On a technical note, I would like to thank M. Salaris for generously providing the oxygen profile shown in Figure 2.4.

Finally, I would like to thank my friends and family for their support and encouragement over the years. My parents have been particularly understanding of the various impractical choices I have made and of the large amount of time I have spent in school. My friends, being less practical themselves, have also been of great help. Thank you to all of you.

While not being religious myself, I find it hard not to view the Universe itself as an 'entity.' Consequently, I am grateful to the Universe for being understandable in a human sense, or at least being polite enough to give the appearance of being so. Hopefully, we will always be just smart enough to figure out some of its secrets.

THE EVOLUTION AND PULSATION OF CRYSTALLIZING WHITE DWARF STARS

Publication No. ____________

Michael Houston Montgomery, Ph.D.
The University of Texas at Austin, 2000

Supervisor: D. E. Winget

This thesis addresses the physics relevant in crystallizing white dwarf stars. This problem is not merely of academic interest, since white dwarf stars provide us with one of the best methods for estimating for the age of the local Galactic disk. In addition, understanding these stars allows us to probe the physics of matter at temperatures and densities otherwise inaccessible in present-day laboratories.

In the first part of my thesis, I explore the effect which phase separation of Carbon and Oxygen can have on the ages of white dwarf stars. I find that this additional energy source can lengthen white dwarf ages by at most ~ 1.5 Gyr, with more likely values being in the range 0.4–0.6 Gyr. The most important factors influencing the size of this delay are the total stellar mass, the initial composition profile, and the phase diagram assumed for crystallization. These relatively small age delays are consistent with recent results that the oldest globular clusters may only be ~ 2 Gyr older than the local Galactic disk.

In the second part of my thesis, I consider the effect which a crystalline core has on the pulsations of white dwarf stars. From global calculations of g-mode eigenfunctions which include the response of the crystalline core, I find that the amplitudes of the g-modes are greatly reduced in the solid region. As a result, the g-mode oscillations can be accurately modeled by a modified boundary condition in which the g-modes are excluded from the solid core.

As the white dwarf models become more crystallized, the mean period spacing and the periods themselves are lengthened, and can increase by as much as 30% for a model which is 90% crystallized by mass. I also show how mode trapping information can be used to disentangle the effects due to the hydrogen layer mass from those due to crystallization. If we are able to obtain mode identifications for enough modes in the DAV BPM 37093, then we may be able to "empirically" measure the degree of crystallization which is present in this object, and thereby test the theory of crystallization itself, now more than 30 years old.

The simplicity of white dwarf stars makes them ideal targets of study, since we believe we can adequately model the physical processes occurring inside them. In addition, 98% of all stars are believed to end their lives as white dwarf stars. If we can understand these stars, then we can provide final boundary conditions for evolution of post-main sequence models. In this sense, they are fundamental objects.

Table of Contents

Table of Tables

List of Figures

Chapter 1

Overview

1. Introduction

The study of stars extends far into our scientific past, and the field of Astronomy arguably holds the title of the oldest "science." Since the time of the ancient Greeks and Babylonians, astronomers have built models of varying complexity which attempted to describe the heavens. By modern standards these models were ad hoc in that they only applied to objects in the heavens, and even then each object had to be treated as a special case. This changed, however, when Newton deduced a small set of physical laws which governed the motions of the Sun and planets *as well as* the motions of objects here on Earth. Thus, he opened the way for us to "understand" the universe in the modern sense, by modeling it in terms of theories and concepts which in principle apply everywhere. In this way, the universe itself became the laboratory in which new models and theories could be tested.

The first serious efforts at modeling the internal structure of stars were made in the mid-1800's, and these efforts were naturally first focussed on understanding the Sun. A paradox ensued, since at the time there was no known energy source capable of sustaining the Sun for the period of time it was believed to have existed on the basis of geological evidence. This remained a mystery until the 1930's, when nuclear fusion and fission were discovered. In this way, the theory of stellar evolution had foreshadowed these discoveries by approximately half a century.

The relatively recent rise of numerical computing allows us to attack stellar modeling in a much more detailed and realistic way than the analytical analyses of the past; we use equations of state and opacities which depend on quantum mechanical properties of individual elements as well as on the ionization equilibrium between many different chemical species. Much of the physics which we use in our models has been calculated theoretically but not verified experimentally, since the temperatures and densities cannot at present be reached in terrestrial laboratories. One goal of stellar astronomy is to use the stars themselves as the laboratories to test our understanding of matter at these temperatures and densities. In order for this process to be effective, we need to have models which are already fairly accurate in describing the physics in the stars.

2. Why We Study White Dwarf Stars

2.1. Physics

White dwarf stars offer us the best opportunity for progress because their structure does not depend as sensitively on poorly known physics as do models of other stars. For instance, since they are supported by degenerate electron pressure, their mechanical structure is essentially separate from their thermal structure, which greatly simplifies the calculations of how they cool. Also, nuclear reactions presumably play no role, at least in the cool white dwarfs, so uncertainties in nuclear reaction rates do not add “theoretical noise” to the models. In addition, convection, while present, never affects more than the outer 10^{-6} in mass of the models. Finally, the high surface gravities ($\log g \sim 8$) ensure that spherical symmetry is a very good approximation, even in the presence of moderate rotation rates or strong magnetic fields.

White dwarf stars have one further characteristic which makes them more meaningful to model: they pulsate when in certain temperature ranges, called instability strips. This allows us to learn about their internal structure by matching the observed frequencies to particular pulsational models of these stars. We call this field “asteroseismology” since it is analogous to the seismological analyses which geologists use to learn about the internal structure of the Earth. This technique allows us to “see inside the stars” in a way which is forbidden to spectroscopy and photometry, which can only measure conditions at the photosphere. If we make the reasonable assumption that these pulsating white dwarfs are representative of the rest of the white dwarf population, then we are better able to constrain our models of these other white dwarfs.

2.2. Astrophysical Relevance

The above arguments convince us that our ability to model white dwarf stars is quite good. More importantly, however, white dwarfs allow us to address issues which are critical to the larger astronomical community.

According to standard Big Bang cosmology, the universe, and therefore the Galaxy, has a finite age. As a result, the oldest white dwarfs should date from the time just after star formation began. Because white dwarf evolution consists of cooling from hotter to cooler temperatures, these oldest white dwarfs should also be the coolest and faintest. This argument predicts that we should find no white dwarfs fainter than a certain minimum luminosity, since there has not been sufficient time since the earliest epochs of star formation for these stars to cool further. Such a luminosity cutoff has indeed been observed (Liebert, Dahn, & Monet 1988; Oswalt et al. 1996).

In order to make use of this faint luminosity cutoff, we must model the cooling of these white dwarfs to determine how long it has taken them to reach their present luminosities. To do this, we need to know what parameters describe the population as a whole. Two of the most important parameters for this are the surface hydrogen and helium layer masses. Recent asteroseismological determinations suggest that these masses are "thick," having fractional stellar masses of $M_{\mathrm{He}}/\mathrm{M}_\star = 10^{-2}$ and $M_{\mathrm{H}}/\mathrm{M}_\star = 10^{-4}$ (Clemens 1993). This knowledge is crucial, since each order of magnitude increase in M_{He} systematically results in a 0.75 Gyr decrease in the ages of white dwarf models at the observed luminosity cutoff (Wood 1990; Wood 1992).

At the present time, the largest systematic source of uncertainty in white dwarf ages, and hence the derived age for the local Galactic disk, arises from potentially unknown physics. This physics is related to the crystallization of the dense plasma in the interiors of cooling white dwarfs. Crystallization, through the release of latent heat, adds approximately 1 Gyr to the cooling times of these models. The process of phase separation of carbon and oxygen, possible during crystallization, has been calculated to add anywhere from 1 to 5 Gyr to these ages. As such, phase separation represents the single largest systematic uncertainty in the theory of white dwarf cooling. While crystallization itself rests on a relatively firm *theoretical* basis, neither it nor phase separation have ever been tested in the laboratory under conditions appropriate to white dwarf interiors.

3. Overview of Thesis

It is the goal of this thesis to address both aspects of this problem. In the first part, we explore the range of age delays which the phenomenon of phase separation can produce in our models. We do this by varying the parameters of our models as well as by varying the prescription used for phase separation. This allows us to assess the main source of uncertainty in the age of the Galactic disk as derived from the observed white dwarf luminosity function.

In the second part of this thesis, we develop the theory of pulsations for white dwarfs with a crystallized core. In so doing, we lay the foundations for the interpretation of data from crystallized white dwarf pulsators. This exploration is not just an academic exercise since we now know of one member which fits into this (hopefully growing) class of objects. The white dwarf BPM 37093, which was recently discovered to be a pulsator (Kanaan et al. 1992), should be substantially crystallized in its interior (Winget et al. 1997), and may provide the first observational test of the theory of crystallization in dense stellar plasmas.

4. Coda

There are two relatively new aspects of the investigation of white dwarf stars which are worthy of mention, since they illustrate the utility of studying white dwarfs. The first is in the context of stellar evolution.

White dwarfs are believed to be the product of processes which take stars on the main sequence and evolve them through the Giant Branch (GB) and Asymptotic Giant Branch (GB), eventually leaving behind a remnant which we identify as the white dwarf. These phases of evolution on the GB and the AGB are relatively poorly understood theoretically, so we are at present unable to model the internal structure of these stars with reliability. Our models of white dwarfs, however, do provide a final boundary condition in time for these post-main sequence models to match.

As an example, Provencal et al. (1998) used Hipparcos data to test the Mass-Radius relationship in white dwarfs. When they compared their data to the zero-temperature Mass-Radius relation calculated by Hamada & Salpeter (1961), they found that the only models which fitted the data for Procyon B had iron in their cores. While they caution that their conclusions are still tentative, this result could have major repercussions concerning our understanding of post-main sequence stellar evolution.

As a final example, supernovae type Ia (SNIa) are believed to result from systems which contain white dwarf stars accreting matter. This accretion increases the mass of the white dwarf model to the point that it triggers a thermonuclear runaway, which we identify as the SN. Recently, Garnavich et al. (1998) have used SNIa's to infer a nonzero value for the cosmological constant Ω. They do this by assuming that SNIa's have an absolute luminosity which is a fixed function of the luminosity profile. They then measure discrepancies in the observed and predicted brightnesses of these supernovae as a function of redshift, and interpret these discrepancies in terms of a nonzero Ω.

In so doing, they are ignoring any potential systematic differences in these supernovae. For instance, a change in the metallicity of the white dwarf from solar abundance to 0.1 solar changes the SN brightness by 0.2 magnitudes, which is comparable to their measured trend suggesting a nonzero Ω (Höflich, Wheeler, & Thielemann 1998; Riess et al. 1998). In addition, phase separation of carbon and oxygen in white dwarfs, if it occurs, would also affect the luminosity of the resulting SN (see Höflich, Wheeler, & Thielemann 1998 for a discussion of SN modeling). Both the metallicity and the amount of phase separation which has occurred in a given white dwarf should be correlated with the age of the white dwarf relative to the onset of star formation in each galaxy. Since galaxies at higher redshifts are systematically younger, their white dwarf populations should show lower metallicities and less phase separation. This will produce a systematic bias as a function of redshift in the SNIa progenitors, and possibly in the supernovae themselves. Garnavich et al. (1998) have not explicitly considered such effects in their analysis.

As we have seen, white dwarf stars provide a fertile astrophysical laboratory in which we may hope to answer many of the larger questions in the field. With the increasing availability of larger telescopes and more sensitive detectors, more and more of these stars will be found and it will be possible to study them in greater detail than ever before. With this increased scrutiny, we hope to discover what secrets these stars hold, and what answers they provide about the universe as a whole.

Chapter 2

Phase Separation

1. Introduction

In this chapter, we present an exploration of the significance of Carbon/Oxygen phase separation in white dwarf stars in the context of self-consistent evolutionary calculations. Because phase separation can potentially increase the calculated ages of the oldest white dwarfs, it can affect the age of the Galactic disk as derived from the downturn in the white dwarf luminosity function. The largest possible increase in ages due to phase separation is $\sim$1.5 Gyr and the smallest is $\sim$0.2 Gyr, with a most likely value in the range of 0.4–0.6 Gyr, depending on the parameters of our white dwarf models.

2. Astrophysical Context

The phenomenon of phase separation and crystallization exists within the larger context of white dwarf cooling. Since the time of Mestel's original treatment (Mestel 1952), much work has been done, both to improve the input physics of the models and to make more complete observations of the white dwarf luminosity function (WDLF). In 1987, Winget et al. showed that the observed downturn in the WDLF could be understood in terms of a finite age for the

Galactic disk, and that the WDLF could therefore in principle be used to determine an age for the local Galactic disk. Using the preliminary results from Liebert, Dahn, & Monet (1988, hereafter LDM) for the observed WDLF, they obtained an age for the local Galactic disk in the range 7–10 Gyr. Since then, Wood has made more detailed calculations using improved input physics, Galactic evolution models, and WD parameters to constrain this age even further Wood (1990, 1992, 1995). Historically, these developments were foreshadowed by Schwarzschild (1958), Schmidt (1959), and D'Antona & Mazzitelli (1978), all of whom considered white dwarf evolution in a Galactic context.

Two observational surveys within the last ten years stand out in their importance to the field. First, Liebert et al. (1988) produced a WDLF containing 43 cool field WD's, which was the largest such sample size up to that point in time. More recently, Oswalt et al. (1996) produced a WDLF of 50 cool WD's in wide binaries. Using the models of Wood, the LDM sample yields an age for the Galactic Disk of $\sim 7.5 \pm 1$ Gyr (Wood 1995), while the Oswalt et al. (1996) sample gives an age of $9.5^{+1.1}_{-0.8}$ Gyr. Taking the error estimates at face value, these results differ by 2σ. Wood & Oswalt (1998) conducted Monte Carlo simulations and found that it is unlikely that both samples are consistent with the same parent population.

In addition to the uncertainties in the observed WDLF, the way we treat various physical processes in white dwarf interiors greatly affects the ages which we derive for them. After the prediction in the early 1960's that white dwarfs should undergo a phase transition and crystallize as they cool (Abrikosov 1960; Kirzhnits 1960; Salpeter 1961), Mestel & Ruderman (1967) and Van Horn (1968) estimated that the associated release of latent heat during this process would be large enough to delay the cooling of white dwarfs significantly. Lamb & Van Horn (1975) included this energy release as part of their evolutionary calculations of a 1 $M_{\odot}$ pure carbon white dwarf.

Stevenson (1977) was the first to propose a phase separation model that might affect white dwarf cooling times by providing an additional source of energy analogous to the release of latent heat. This model had a carbon core with trace amounts of iron. In a later model, Stevenson (1980) suggested that a uniform mixture of carbon and oxygen would become chemically differentiated as a result of the crystallization process. Because such a redistribution of elements could lower the binding (non-thermal) energy of the star, the change in energy would be added to the thermal energy, and hence the luminosity, of the star. This would increase the time for a white dwarf to cool to a given luminosity, and would extend the apparent age of the Galactic disk as derived from the WDLF.

Estimates of the amount by which the age of the local Galactic disk might be extended have ranged from 0.5 Gyr to 6 Gyr (Mochkovitch 1983; Barrat, Hansen, & Mochkovitch 1988; García-Berro et al. 1988; Chabrier et al. 1993; Segretain & Chabrier 1993; Hernanz et al. 1994; Segretain et al. 1994; Isern et al. 1997; Salaris et al. 1997), although recent estimates have been on the smaller end of this range, e.g., Salaris et al. (1997) calculate a delay of ~ 1.0 Gyr. Most of this spread in calculated age delays comes from differences in the assumed phase diagram, although the assumed C/O profile also has a large effect.

In the context of Galactic evolution, recent mean age estimates for the oldest Galactic globular clusters are smaller now than ever before (11.5 $\pm$ 1.3

Gyr), while estimates of the age of the Galactic disk from the observed white dwarf luminosity function (ignoring phase separation) are only slightly less ($9.5^{+1.1}_{-0.8}$ Gyr). If the above age estimates for globular clusters and the Galactic disk are correct, then any effects due to phase separation cannot be much larger than 1–2 Gyr.

In this chapter, we examine the sensitivity of this calculated age delay to the various physical assumptions by varying the initial C/O profile of the white dwarf models, their total mass, and their H and He surface layer masses. In addition, we examine the effect of using two different published phase diagrams for the phase separation process, that of Segretain & Chabrier (1993) and that of Ichimaru, Iyetomi, & Ogata (1988). We demonstrate through self-consistent evolutionary calculations that previous approaches to this problem (e.g., Salaris et al. 1997) are valid.

3. The Physics of Phase separation

3.1. Chemical Redistribution

Our present physical picture for the phenomenon of phase separation in white dwarf stars is as follows. As a white dwarf cools, it eventually reaches a temperature when its central regions begin to crystallize. This occurs when the thermal energy of the ions becomes much smaller than the energy of the Coulomb interaction between neighboring ions. As a result, the ions settle into lattice sites and lose the ability to move freely in three dimensions.

If the white dwarf interior is initially a mixture of C and O, then recent calculations indicate that the solid which crystallizes will have a higher O content than the fluid from which it formed (Ichimaru et al. 1988; Segretain & Chabrier 1993). Thus the crystallizing region of the white dwarf becomes O-enhanced and the fluid layer overlying this region becomes C-enhanced. Since the C is slightly less dense than the O at a given pressure, this C-enhanced fluid layer is mixed via a Rayleigh-Taylor instability (Mochkovitch 1983, Isern et al. 1997) with the layers above, and C is transported outward from the center. As the white dwarf continues to crystallize, the O-enhanced crystalline core also continues to grow, with the net result that O is transported inward in the white dwarf and C is transported outward. Thus, the chemical profile after significant crystallization has occurred is different from the profile before crystallization.

Just how different this profile is depends on the particular phase diagram which is adopted for the process. In a "spindle" diagram, the solid which forms always has an enhanced concentration of the higher charge element (in this case oxygen), and the temperature of crystallization of the mixture lies between that of the individual elements. An "azeotropic" diagram differs from this in that there is a range of concentrations for which crystallization takes place *below* the temperature of crystallization of either of the pure elements. This is somewhat analogous to the phenomenon of "supercooling". Finally, a "eutectic" phase diagram is one in which there is near total separation of the higher and lower charged ions upon crystallization, resulting in a segregation of the two chemical species.

Stevenson's original phase diagram (Stevenson 1980) was a eutectic phase diagram with C and O being immiscible in the solid phase, with the result that a pure O core would be formed in the models during crystallization.

Using a density functional approach, Barrat et al. (1988) calculated a phase diagram of spindle type. In this case, the solid which forms is a C/O alloy, but with the O content of the solid enhanced relative to that of the fluid out of which it formed.

This problem was revisited by Ichimaru et al. (1988). They found that Stevenson's initial prediction of a eutectic phase diagram was an artifact of his use of the random-alloy mixing (RAM) model for the internal energies in the solid phase. By comparison with Monte Carlo simulations, they found that the linear mixing formula is more accurate for the solid phase. They then used density-functional theory to derive a phase diagram of azeotropic type, which is shown as the dashed line in Figure 2.1. This diagram is similar to the spindle diagram, with the exception that there is a range of compositions for which the crystallization temperature is less than the crystallization temperature for either of the pure compositions.

Most recently, Segretain & Chabrier (1993) used a density-functional approach to derive phase diagrams for arbitrary binary-ionic mixtures, as a function of Z_1/Z_2, where Z_1 and Z_2 are the nuclear charges of the two chemical species. For C and O ($Z_1/Z_2 = 0.75$), they obtain a phase diagram of spindle type, which is shown as the solid line in Figure 2.1.

As shown in Figure 2.1, these diagrams of Ichimaru et al. and Segretain & Chabrier differ slightly in the composition changes during crystallization, as well as in the temperatures at which crystallization takes place. As a result, they produce different chemical profiles after crystallization and different age delays.

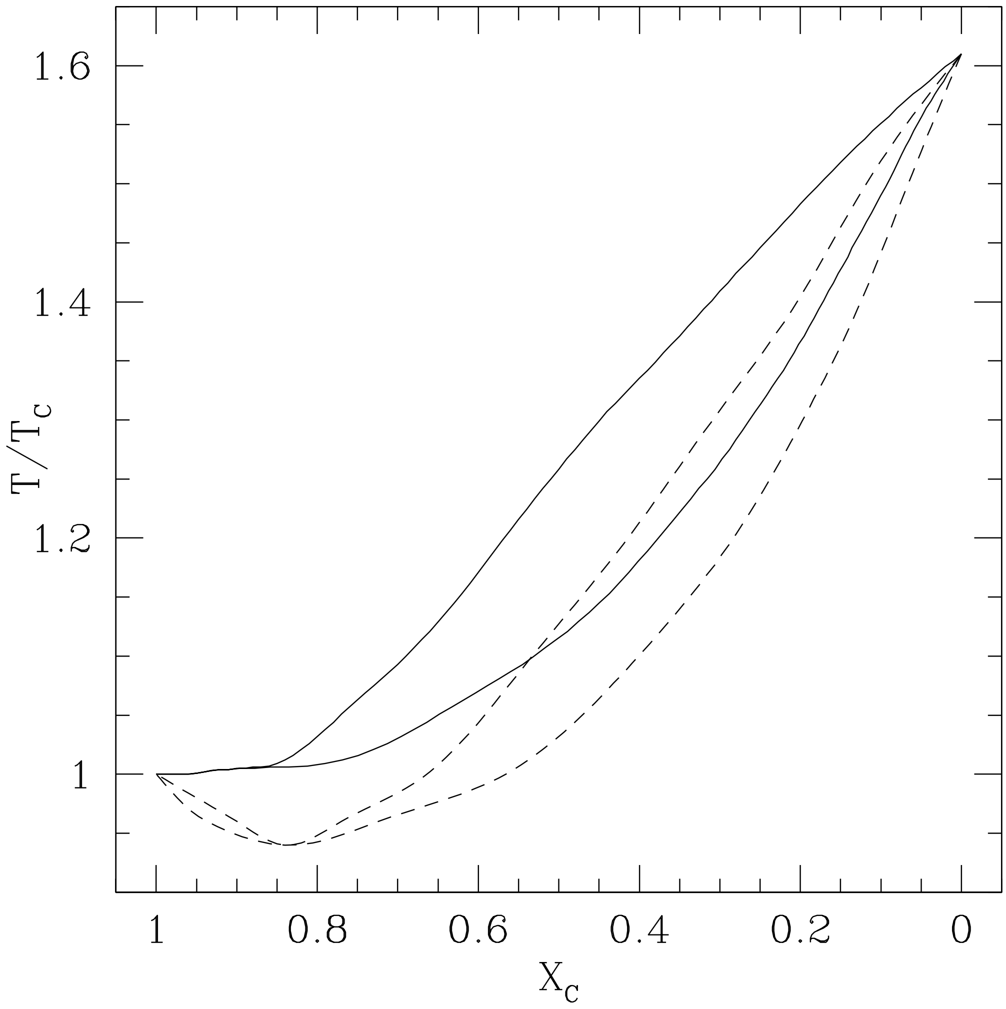

Fig. 2.1.— Phase diagrams for a C/O mixture as computed by Ichimaru et al. (1988, dashed line) and Segretain & Chabrier (1993, solid line), where the vertical axis is in units of the crystallization temperature of C, and the horizontal axis is the C mass-fraction. The solid line is of "spindle" type, while the dashed line is that of an "azeotrope". The principal feature of the azeotrope is that there is a range of compositions for which the crystallization temperature of the mixture is less than that of either of the two constituents in the pure state.

3.2. Energy Release

Because the distribution of C and O within a model changes during phase separation, the density profile changes as well. At a given pressure, O is slightly denser than C. A model which has undergone phase separation has more oxygen in its core, and thus a slightly larger concentration of mass in its central regions. As a result, the phase-separated model is more tightly bound gravitationally.

While it may be convenient to think of the energy which is released as being due solely to the change in the gravitational potential energy of the star, this is only part of the story. The relevant quantity is actually the total binding energy of the star, $E_{\rm bind}$, which is the sum of all the nonthermal (structural) sources of energy. As such, it acts as a potential energy for the configuration. $E_{\rm bind}$ can be written as

$$E_{\rm bind} = E_{\rm grav} + E_{\rm deg} + E_{\rm coul} \tag{2.1}$$

where $E_{\rm grav}$, $E_{\rm deg}$, and $E_{\rm coul}$ are the respective energy contributions from gravitational interactions, kinetic energies of the degenerate electrons, and Coulomb interactions among the different charged particles (ions and electrons).

As phase separation occurs and the central regions become oxygen enriched, the central density of the model increases. Thus, $E_{\rm grav}$ becomes more negative, as does $E_{\rm coul}$. $E_{\rm deg}$, however, becomes more positive, since the Fermi energy of the electrons increases with increasing density. Summing these contributions, we find that there is a net decrease in $E_{\rm bind}$ for the models considered here. Due to conservation of energy, this energy must be used to increase the thermal energy of the ions, which are the only significant repository of thermal energy in the cores of our white dwarf models. This energy, then, is available to be radiated away and acts as an additional luminosity source.

In order to make this process clearer, we give the following example which might be appropriate for a simplified model of planetary interiors. Imagine we have a self-gravitating object made of two different materials which are uniformly mixed, each of which is incompressible. If the materials are fluid (e.g., molten), then the heavier of the two will sink to the center forming a core comprised purely of the heavy material, surrounded by a mantle of the lighter material. The internal energies of the fluid elements do not change as they are transported up and down since the surrounding fluid medium is unable to do any work on these elements by compressing them. This situation is analogous to setting $E_{\rm coul}$ and $E_{\rm deg}$ to zero in the white dwarf case. Thus, the only change in energy is the change in gravitational energy, which is clearly negative. This gravitational energy change is what drove the fluid motions even in the presence of viscous and other dissipative processes, and it is these processes which transform the mechanical motion of "phase separation" into thermal energy, thus allowing the object to remain warm longer.

The various contributions to the photon luminosity L and the neutrino luminosity L_ν of the white dwarf may be formally written as (e.g., Isern et al. 1997; Chabrier 1998)

$$L + L_\nu = -\int_0^{M_{\rm WD}} dm \left(C_v \frac{dT}{dt} + T \left(\frac{\partial P}{\partial T}\right)_{V,X_O} \frac{dV}{dt} + \left(\frac{\partial u}{\partial X_O}\right)_{T,V} \frac{dX_O}{dt} \right) \quad (2.2)$$

where $V = 1/\rho$ is the specific volume, X_O is the mass-fraction of the heavier of the two chemical species (in this case, oxygen), and u is the internal energy per unit mass, which contains thermal, electron degeneracy, and Coulomb contributions. The first term in the integrand on the righthand side of equation 2.2 is due to the heat capacity of the core, which includes the release of latent heat of crystallization, while the second term gives the contribution to the luminosity due to volume changes, and is usually small in white dwarfs since the pressure P is only a weak function of the temperature. The final term gives the luminosity due to the changing chemical profiles within the white dwarf. This is the term we will study in our numerical calculations.

As a check on the direct evolutionary calculations, we can estimate the age delay produced by a given energy release. If we denote by dE a small amount of energy which is released during the process of phase separation, and if we assume that this energy is quickly radiated, then we can calculate an estimated age delay t_d:

$$t_d = \int \frac{dE}{L}. \tag{2.3}$$

In the context of a sequence of evolutionary models, this integral is operationally a sum, since a given model is computed at discrete points in time, luminosity, etc. Furthermore, since the energy ΔE_i is released *between* luminosities L_{i-1} and L_i, say, the average luminosity at which the energy is released is approximately $(L_{i-1} + L_i)/2$, so the discrete version of equation 2.3 becomes

$$t_d = \sum_i \frac{\Delta E_i}{\frac{1}{2}(L_{i-1} + L_i)}. \tag{2.4}$$

We have used equation 2.4 as an alternate prescription to calculate age delays. For the larger energy releases, t_d computed in this way agrees with the delay calculated from the self-consistent evolutionary calculations, and for small energy releases it provides a better estimate since the small energies can become masked in the numerical noise of the evolutionary calculations.

4. Numerics

The basis for these calculations is WDEC, the White Dwarf Evolutionary Code, as described in Lamb & Van Horn (1975), and in Wood (1990). Our current version uses the updated OPAL opacity tables (Iglesias & Rogers 1993; Wood 1993). We use the additive volume technique to treat the equation of state of the C/O mixture in the cores of our models.

4.1. The Melting Curve

Our criterion for crystallization is given by the phase diagram which we adopt, with the following caveat. Our equation of state (EOS) is based on the Lamb EOS code (Lamb & Van Horn 1975), which has $\Gamma \simeq 160$ at crystallization. Here, $\Gamma \equiv Z^2e^2/\langle r\rangle k_BT$ is the ratio of Coulomb energy between neighboring ions to each ion's kinetic energy. More recent calculations indicate that $\Gamma \simeq 180$ (Ogata & Ichimaru 1987). As a result, our values for the crystallization temperature of C, $T_{\rm C,xtal}$, are too high by a factor of $\sim 180/160 = 1.125$.

To remedy this situation, we could simply adjust $T_{\rm C,xtal}$ downward accordingly, and we have done this for a few runs. This is inconvenient, however, because it places us at the edge of our EOS tables which were calculated with $\Gamma \simeq 160$. Instead, we apply a correction factor to our calculated age delays which takes into account the fact that crystallization/phase separation occurs at lower central temperatures, and therefore lower luminosities, than is calculated directly in our models. This correction to the calculated age delays is typically of order 25%. We find that this procedure for calculating the age delay is accurate to within 1–2% when compared to sequences which we calculate self-consistently with $\Gamma \simeq 180$.

4.2. Implementation in WDEC

The calculation of the evolutionary sequences is "quasi-static" in the sense that we compute a sequence of static models separated by finite steps in time. Each static model represents the cooling white dwarf at a different age and luminosity. We include the physics of phase separation using the same approximation: we assume that the timescale for any mixing which occurs is short compared to the individual evolutionary timesteps (see section 4.3. of this chapter; Mochkovitch 1983; Isern et al. 1997), and we assume that the binding energy which is released by this process can be modeled by some suitably chosen local energy generation rate, $\epsilon_{\rm ps}$ (e.g., Isern et al. 1997). The phase separation calculation may therefore be broken into three sections. The first part involves obtaining the changing composition profile as a function of the crystallized mass-fraction, while the second part is the calculation of the cumulative energy released, also as a function of the crystallized mass-fraction. The final part is the calculation of the value of $\epsilon_{\rm ps}$, which is the energy locally deposited per unit mass per unit time. Our implementation of the complete problem is self-consistent in that we let $\epsilon_{\rm ps}$ vary as the compositional profile changes due to crystallization, as WDEC iterates to a converged model.

The first part of the overall problem relates to the composition of the crystallizing layers. Using the phase diagram of Segretain & Chabrier (1993) or Ichimaru et al. (1988), we compute the final composition profile of the model given the initial profile, before doing a full evolutionary calculation. This is possible because the composition of the crystals which are forming is determined solely by the mass fractions of C and O which are present in the fluid phase, and not by the temperature and density of the medium (the temperature and density of course determine *when* the fluid crystallizes, but given that it is crystallizing, the chemical composition of the solid is determined *solely* by the composition of the fluid). We are therefore required to compute only once, at the onset of crystallization, the composition profile as a function of the crystallized mass fraction. At subsequent evolutionary times, we use this relation and the current crystallized mass-fraction to interpolate onto the composition grid, which is a computationally convenient procedure.

We take this same approach for the calculation of the energy released. At the onset of crystallization, we calculate the total amount of energy released as a function of $M_{\rm xtal}/M_{\star}$, using the relation

$$\delta E = \int_0^{M_{\rm WD}} \left(\frac{\partial u}{\partial X_O}\right)_{\rm T,V} \delta X_O dm, \tag{2.5}$$

where δE is the binding energy released by the composition change δX_O. Since these changes in composition are with respect to the pre-crystallization state, we are in effect holding both the temperature and density profiles constant for all subsequent phases of crystallization. Holding the temperature profile constant is a quite reasonable approximation, since the vast majority of the mass in the the white dwarf model is strongly degenerate for the temperature range of interest. Similarly, we expect the changes in the density profile to be small ($\frac{\delta\rho}{\rho} \lesssim 1\%$) even in the presence of composition changes. This is a consequence of the fact that the equations of state for carbon and oxygen are very similar in the strongly degenerate regime, i.e., $\mu_{\rm e} = 2.0$ for both elements. This suggests that this approach would not necessarily be as accurate for carbon and iron, for instance, since $\mu_{\rm e} = 2.15$ for iron.

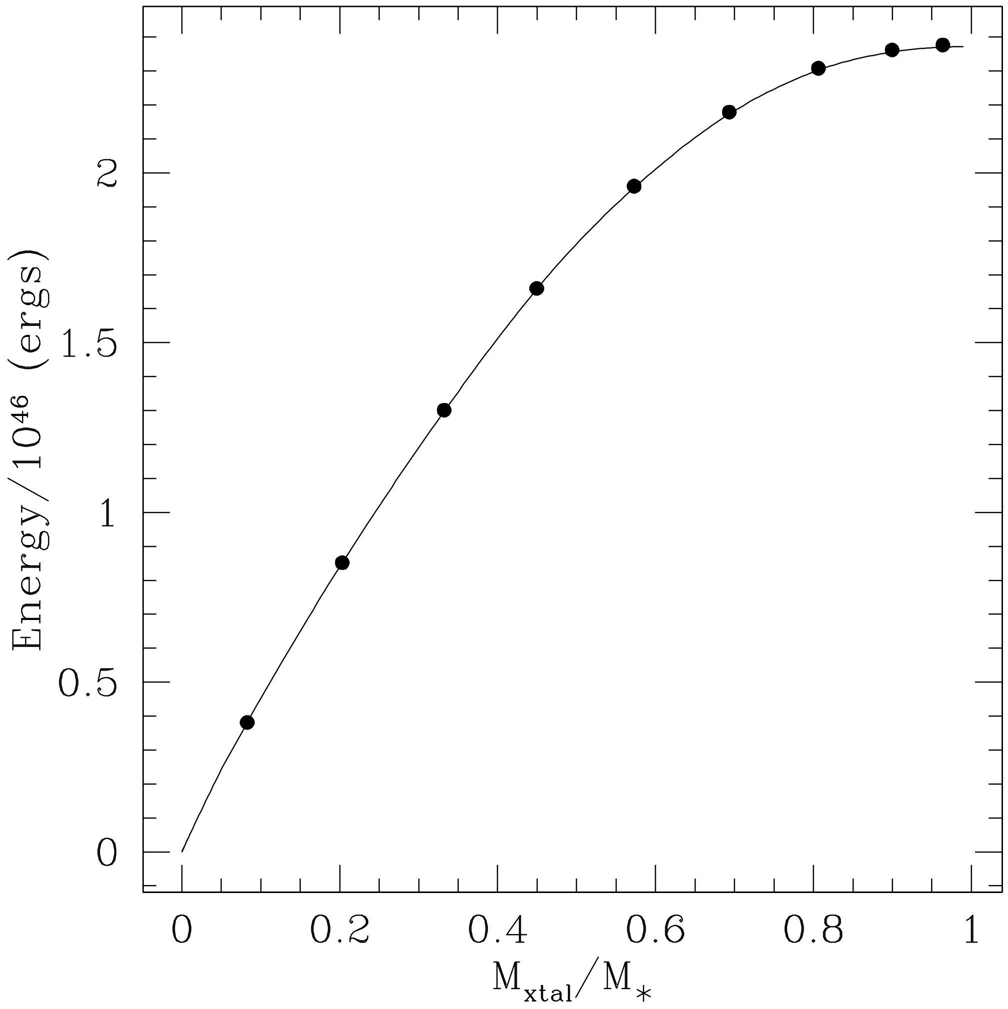

Fig. 2.2.— A comparison of the energy released during crystallization from a static calculation (line) with that from a self-consistent evolutionary calculation (filled dots). The error for the total energy released at complete crystallization is less than 0.5%.

Figure 2.2 provides the final justification for our assumptions. The filled dots represent the energy released as computed self-consistently at each evolutionary time step, and the solid line is the calculated energy released assuming a static density and temperature profile as described in the above paragraph. The best agreement is for smaller amounts of crystallization, since these models differ the least from the initial static model. Even near complete crystallization, however, the difference between the two values is less than 0.5%, justifying our assumptions. Computationally, it is very convenient to compute the energy release just once at the outset and then interpolate using the present value of the crystallized mass fraction. This allows WDEC to avoid doing a calculation of the energy release for each iteration of each model, which would significantly affect the speed of the calculations.

Because all our calculations are done on evolutionary timescales, we do not have any information about the actual dissipative processes which are responsible for depositing the energy of phase separation locally. Indeed, without an accurate hydrodynamic model of the mixing process, this is not possible. Fortunately, it is more important to know the total energy released rather than exactly how this energy is deposited within the white dwarf model. This is because the core has a very high thermal conductivity, which tends to smooth out the temperature distribution. Thus, wherever the energy is initially deposited, it will soon be shared throughout the core; indeed, an isothermal core was an assumption of the original Mestel theory (1952), and it is still a very accurate description of the physics in the interiors of white dwarfs (e.g., García-Berro et al. 1996; Segretain et al. 1994). We therefore choose $\epsilon_{\rm ps}$ such that the local temperature is increased by the same fractional amount throughout the core, i.e., $\frac{\delta T}{T}$ = const., while we simultaneously require that the total energy deposited in this way is equal to the energy released due to phase separation in a given timestep. This is somewhat analogous to the analytical approach outlined by Isern et al. (1997), although we developed our approach for ease of numerical implementation.

There is one final adjustment which we make to the value of $\epsilon_{\rm ps}$ as calculated above. It is due to the fact that WDEC calculates models quasi-statically, so that $\epsilon_{\rm ps}$ is assumed to have been constant during the last time step taken, when in fact it may have changed by a substantial amount. Put another way, the value of $\epsilon_{\rm ps}$ which WDEC calculates should be associated with the average luminosity of the present and previous timesteps, not just the current luminosity. Thus, WDEC is implicitly calculating a delay based upon

$$t_d = \sum_i \frac{\Delta E_i}{L_i} \tag{2.6}$$

instead of the expression in equation 2.4. We can remedy this situation by an appropriate rescaling of $\epsilon_{\rm ps}$. If we rescale ΔE_i, and hence $\epsilon_{\rm ps}$, by $\frac{L_i}{\frac{1}{2}(L_i+L_{i-1})}$, then equation 2.6 is transformed into equation 2.4, and we recover the correct age delay due to crystallization when implemented in the evolution code. In the limit that our timesteps are very small, the above prescription is not necessary, but such small timesteps would be computationally inconvenient, both from a cpu-time standpoint and from a numerical convergence standpoint.

4.3. Consistency Checks

We use three different initial C/O profiles in our analysis. In Figure 2.3 we show the oxygen composition in the core both before (dotted line) and after (solid line) crystallization has taken place. We have taken a homogeneous 50:50 C/O initial distribution and assumed complete mixing of the overlying fluid layers as crystallization takes place. This should place an upper limit on the effect which phase separation can have on any particular model. We note that the composition profile after crystallization assuming the Segretain & Chabrier (1993) phase diagram agrees well with that given in Chabrier et al. (1993).

Figure 2.4 shows a different initial oxygen profile which is computed in Salaris et al. (1997) for a 0.61 $M_{\odot}$ white dwarf model. This profile was obtained by considering nuclear reaction processes in the white dwarf progenitor. Here we use a modified algorithm for mixing which reduces to the "complete mixing" algorithm when applied to an initially flat distribution. When a shell crystallizes, we check to see if the enhanced carbon content of the innermost fluid shell now has more carbon than the shell overlying it. If it does, then we mix the two shells and perform the same comparison with the next shell farther out, mixing all three shells if necessary. In this way, we move outward through the fluid until further mixing no longer decreases the carbon content of the fluid between this point and the crystallization boundary. This is physically reasonable, since carbon is, in a sense, "lighter" than oxygen, so these layers should be mixed by a convective instability.

For completeness, we use a third profile taken from Wood (1990) and Wood (1995). It is designed to be representative of C/O profiles calculated in Mazzitelli & D'Antona (1986) and D'Antona & Mazzitelli (1989), who also

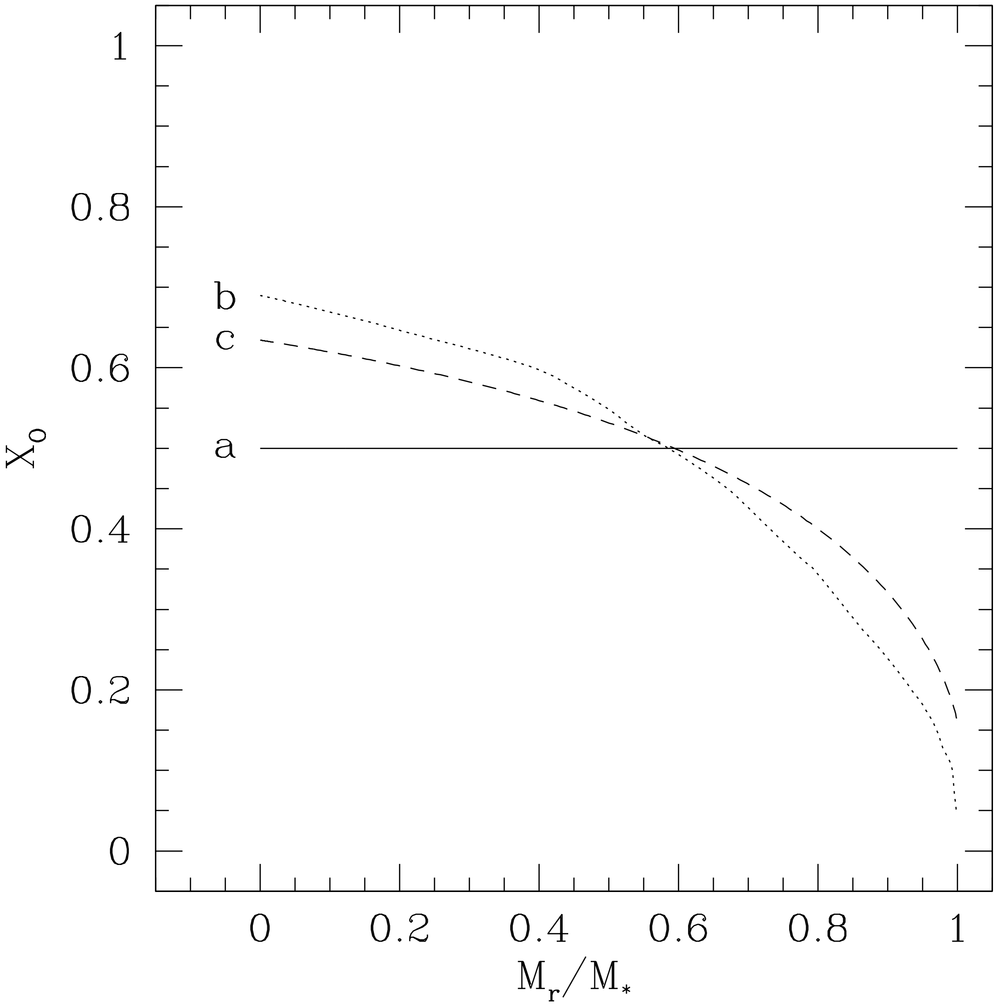

Fig. 2.3.— Before crystallization has occurred, we have assumed a 50:50 C/O mixture, as shown by the solid line (a). After crystallization is complete, the oxygen profile is given by the dotted line (b) if the phase diagram of Segretain & Chabrier (1993) is used, and by the dashed line (c) if the phase diagram of Ichimaru et al. (1988) is used. We have assumed complete mixing of the remaining fluid layers at each stage of crystallization. It is the redistribution of matter from the initial to the final profile which results in a net decrease in the overall binding energy of the configuration. This model is for a 0.6 $M_{\odot}$ white dwarf.

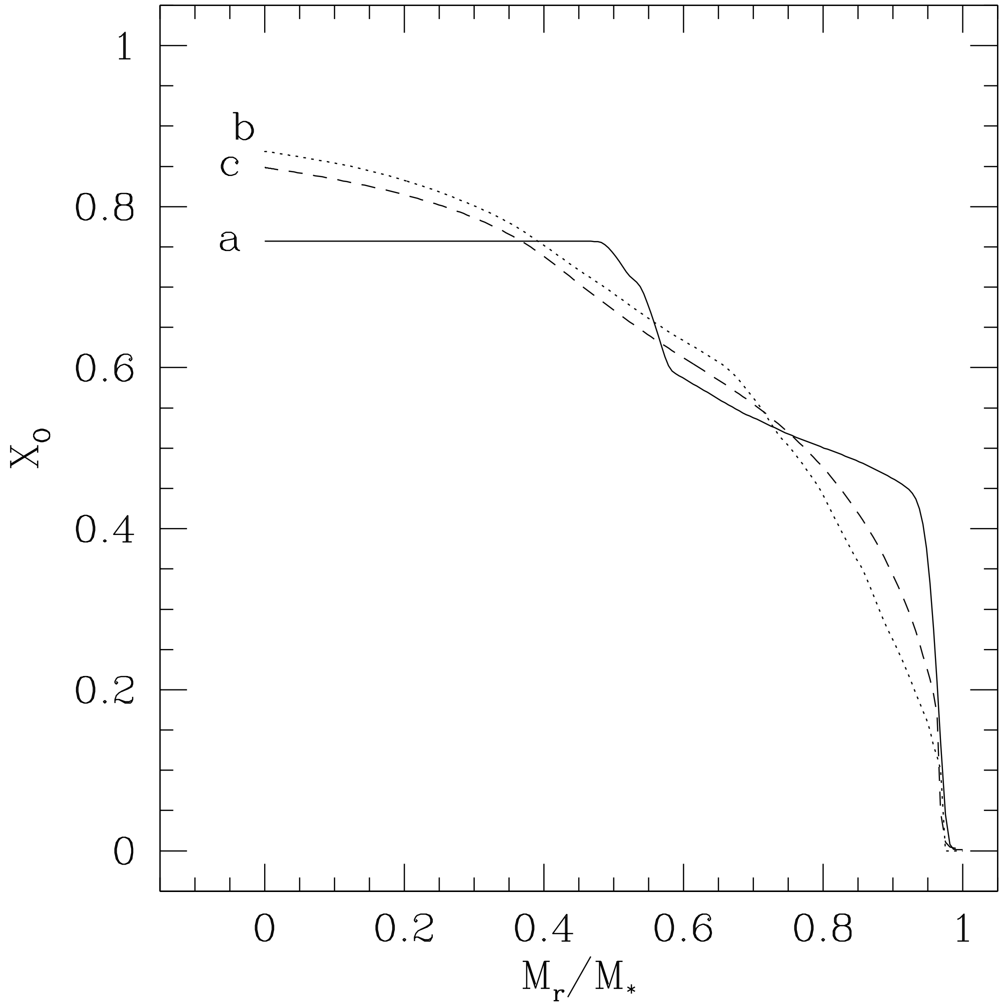

Fig. 2.4.— The same as Figure 2.3, except that the initial C/O profile (a) is that computed by Salaris et al. (1997) for a 0.61 $M_{\odot}$ white dwarf model. Curves (b) and (c) are the final profiles assuming the Segretain & Chabrier (1993) and Ichimaru et al. (1988) phase diagrams, respectively. Note that the oxygen mass-fraction at the very center increases by only about 15% during crystallization in this case, as compared with a 40% increase for the central value in Figure 2.3. Thus, less energy is liberated.

consider nuclear reaction rates. Algebraically, it is given by

$$X_{\rm ox} = \begin{cases} 0.75 & 0.0 \le q \le 0.5 \\ 0.75 - 1.875(q - 0.5) & 0.5 < q \le 0.9 \\ 0.0 & 0.9 < q \le 1.0 \end{cases} \tag{2.7}$$

where $q = M_{\rm r}/M_\star$ and $X_{\rm c} = 1 - X_{\rm ox}$.

Our treatment of mixing provides an upper bound for the efficiency of this process. If we were to perform a more self-consistent calculation, we would compute the Brunt-Väisälä frequency for a given chemical profile in the model and mix those layers which were convectively unstable *and* whose computed timescales for mixing were shorter than the individual timesteps in our evolutionary calculations. An analytical approach to this more detailed problem is given in Isern et al. (1997) and Mochkovitch (1983). Here we merely note that a typical value of $|N^2|$ for a Rayleigh-Taylor unstable region in the cores of our models is $\sim 10^{-4}$, yielding a timescale for the mixing instability of $\frac{1}{|N|} \sim 10^2$ s, which is clearly shorter than the relevant timescales for evolution.

5. A Simple Test Problem

As a check of the standard approach to treating phase separation, we performed a simplified treatment of that given in Xu & Van Horn (1992), in which they calculate the change in binding energy of a zero-temperature C/Fe white dwarf which undergoes phase separation. In order to do this, we have written a separate code which implements the equations for a zero-temperature degenerate electron gas. Our approach is simpler in that we do not include Coulomb effects in our EOS calculations, so our approach is essentially pure Chandrasekhar theory (Chandrasekhar 1939). We do include, however, relativistic effects, which

Xu & Van Horn are unable to treat. In testing this approach to phase separation, we compute the energy released due to phase separation in two different ways. First, we directly compute the global change in the binding energy. Second, we use the expression for the local energy release and integrate this over the mass of the model, as given in equation 2.5. To further simplify things, we have taken the initial state to be one in which the distribution of Fe and C is uniform throughout the model, and we have taken the final state to be a pure Fe core surrounded by a pure C mantle.

Figure 2.5 shows the results for differing initial fractions of C and Fe. For instance, for an initial 50:50 C/Fe distribution we calculate an energy release of about $1.9 \cdot 10^{48}$ ergs, with less than a 5% relative error between the two methods. Even this small amount of error decreases as we approach a pure Fe or C initial state. This is because the density and composition changes before and after phase separation are now smaller. For instance, if the model is 99% C uniformly distributed initially, then after phase separation most of it (99% in fact) is pure C. The contrast between 99% and 100% is small enough that the local density and composition changes are also small ($\delta X_{\rm C} \lesssim$ 1%, $\frac{\delta\rho}{\rho} \lesssim 0.1\%$), which means that the approximation involved in making the infinitesimal variations in equation 2.5 finite is more accurate. We note that it is possible to perform such a simplified treatment for a C/Fe white dwarf model and still obtain meaningful results, while for a C/O model it would not be possible. This is because $\mu_{\rm e} = 2.0$ for both C and O, while $\mu_{\rm e} = 2.15$ for Fe. Thus, ignoring Coulomb effects, C and O have identical equations of state, while C and Fe are still nontrivially different in this approximation.

The results of this test problem (Figure 2.5) convince us that by applying equation 2.5, we are correctly calculating the change in the binding energy of the configuration, and thus the amount of thermal energy which has been liberated from structural sources. This shows us that the overall approach to this problem which we use here, and which has been used in the past, is sound and accurately describes the physics of phase separation.

6. Results

6.1. 0.6 $M_\odot$ White Dwarf Models

In Table 2.1 we give an evolutionary listing of our fiducial sequence (other sequences are available from the author upon request). This sequence is more than just a convenient reference model for the rest of our calculations. Given the observed peak of the masses of isolated white dwarfs in the vicinity of 0.6 $M_\odot$ (Weidemann & Koester 1983; Weidemann & Yuan 1989; Bergeron et al. 1995; Lamontagne et al. 1997), this model will be the most useful in our comparisons with the white dwarf population as a whole. For the surface layer masses, we have taken $M_{\rm He}/M_\star = 10^{-2}$ and $M_{\rm H}/M_\star = 10^{-4}$ as in Wood (1995). We explore the effect of different surface layer masses later in this section.

We now wish to consider the effect of phase separation on actual evolutionary sequences. We compute this effect in two different ways. Using the first method, we compare sequences in which the physics of phase separation is included with those in which it is not. Taking two such sequences, we first perform a spline fit for each sequence's age over a fixed luminosity grid, and then we calculate the difference in ages at each luminosity. The results are given by the solid line in Figure 2.6, and indicate an age delay of about 1.5

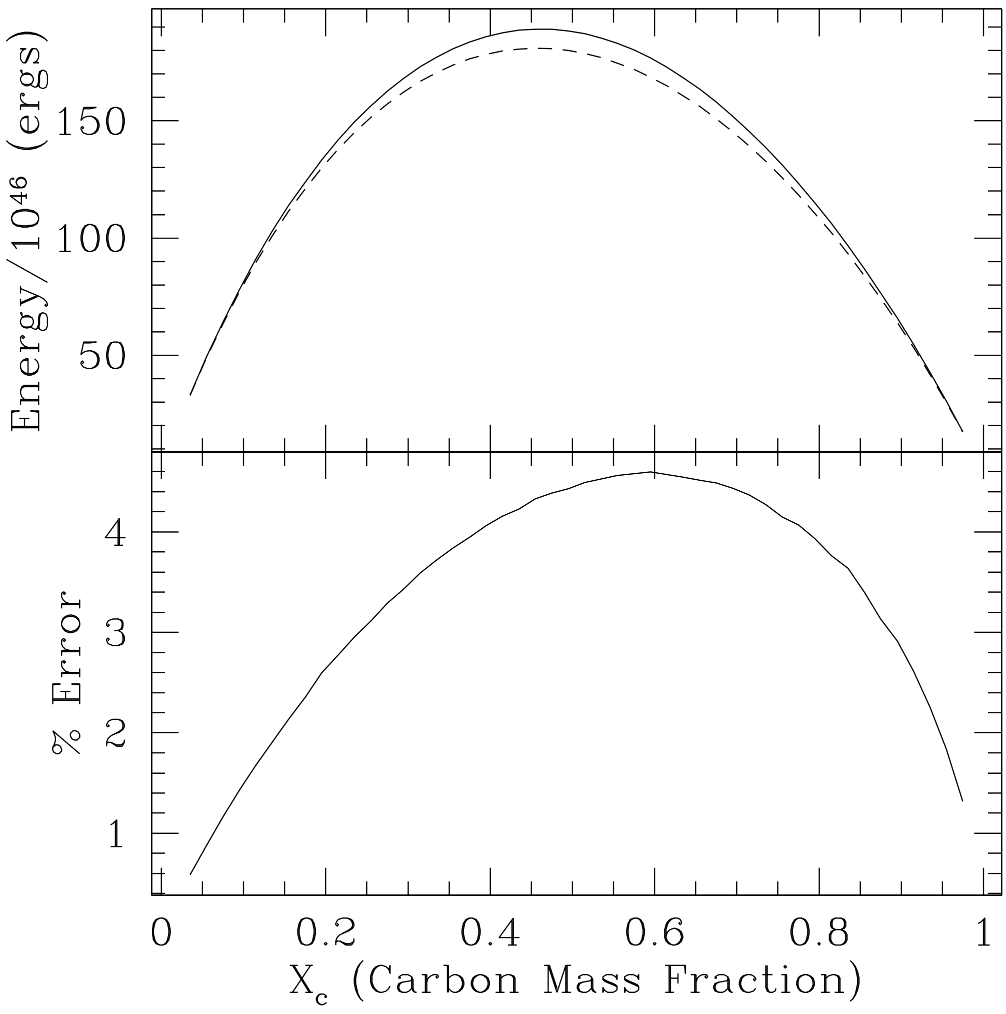

Fig. 2.5.— The upper panel shows the energy released due to phase separation as a function of X_c, the carbon mass-fraction. The model is a C/Fe mixture computed assuming pure Chandrasekhar theory. The solid line comes from a direct calculation of the change in binding energy, and the dotted line is obtained from the application of equation 2.5. The lower panel shows the percent error between these two methods. The total mass of the model is set to 0.66546 $M_{\odot}$, as in Xu & Van Horn (1992).

Table 2.1. Fiducial White Dwarf Cooling Sequence without Phase Separation

$\log L/L_\odot$	log Age (yr)	$\log T_c$	$T_{\rm eff}$	$\log R_\star$	$\log L_\nu/L_\odot$	$M_{\rm xtal}/M_\star$
1.0000	5.917	7.950	4.869	9.131	1.298	0.000
0.6000	6.158	7.891	4.793	9.084	0.946	0.000
0.2000	6.376	7.843	4.710	9.049	0.581	0.000
-0.2000	6.592	7.798	4.623	9.024	0.193	0.000
-0.6000	6.855	7.737	4.533	9.004	-0.230	0.000
-1.0000	7.204	7.660	4.440	8.989	-0.886	0.000
-1.2000	7.429	7.604	4.394	8.982	-1.356	0.000
-1.4000	7.674	7.531	4.346	8.976	-1.956	0.000
-1.6000	7.903	7.448	4.299	8.971	-2.670	0.000
-1.8000	8.097	7.360	4.251	8.967	-3.449	0.000
-2.0000	8.264	7.273	4.203	8.963	-4.248	0.000
-2.2000	8.413	7.187	4.155	8.959	-5.042	0.000
-2.4000	8.550	7.103	4.106	8.956	-5.804	0.000
-2.6000	8.679	7.021	4.058	8.953	-7.279	0.000
-2.8000	8.805	6.940	4.009	8.951	-10.000	0.000
-3.0000	8.930	6.860	3.961	8.948	-10.000	0.000
-3.2000	9.055	6.778	3.912	8.946	-10.000	0.000
-3.4000	9.182	6.694	3.863	8.944	-10.000	0.000
-3.6000	9.317	6.613	3.814	8.942	-10.000	0.059
-3.8000	9.497	6.518	3.765	8.939	-10.000	0.379
-4.0000	9.704	6.350	3.717	8.935	-10.000	0.804
-4.2000	9.825	6.176	3.668	8.933	-10.000	0.961
-4.4000	9.900	6.022	3.618	8.933	-10.000	0.989
-4.6000	9.953	5.891	3.569	8.932	-10.000	0.990
-4.8000	9.996	5.777	3.519	8.932	-10.000	0.990

Gyr; this is for an initially homogeneous 50:50 C/O profile with an assumed metallicity of $Z = 0.000$ in the opacities.

The other method involves applying equation 2.4 to a sequence undergoing phase separation, which is shown by the dotted line Figure 2.6. This yields an asymptotic value for the age delay of 1.38 Gyr, which is within 5% of the age difference computed with the first method. This result indicates that the basic physics which is operating is well-described by equation 2.4, i.e., the energy being released by phase separation is mostly being radiated in a given timestep. For the remainder of the results quoted here, the age delays have been calculated using the second method (equation 2.4), since this proves to be more accurate for the cases involving smaller energy releases and age delays.

We now study the effect of the initial composition profile on the age delays. We use three different profiles: one which is a homogeneous 50:50 mix (Figure 2.3), one calculated by Salaris et al. (1997) (Figure 2.4), and one given by equation 2.7. Our results are summarized in Table 2.2, where the columns labeled SC and IIO indicate that we have used the phase diagrams of Segretain & Chabrier (1993) and Ichimaru et al. (1988), respectively. Near the centers of these models, we found that the initial/final oxygen mass-fraction changed by only about 15% in the initially stratified case in Figure 2.4, as compared to 40% in the homogeneous case in Figure 2.3. Because less matter is being redistributed in the initially stratified case, we would expect less energy to be released as a result. Using the phase diagram of Segretain & Chabrier (1993) applied to a 0.6 $M_{\odot}$ white dwarf model, we find that in the homogeneous case $2.38 \cdot 10^{46}$ ergs are released whereas in the initially stratified case in Figure 2.4 only $1.03 \cdot 10^{46}$ ergs are released. These energies result in age delays of

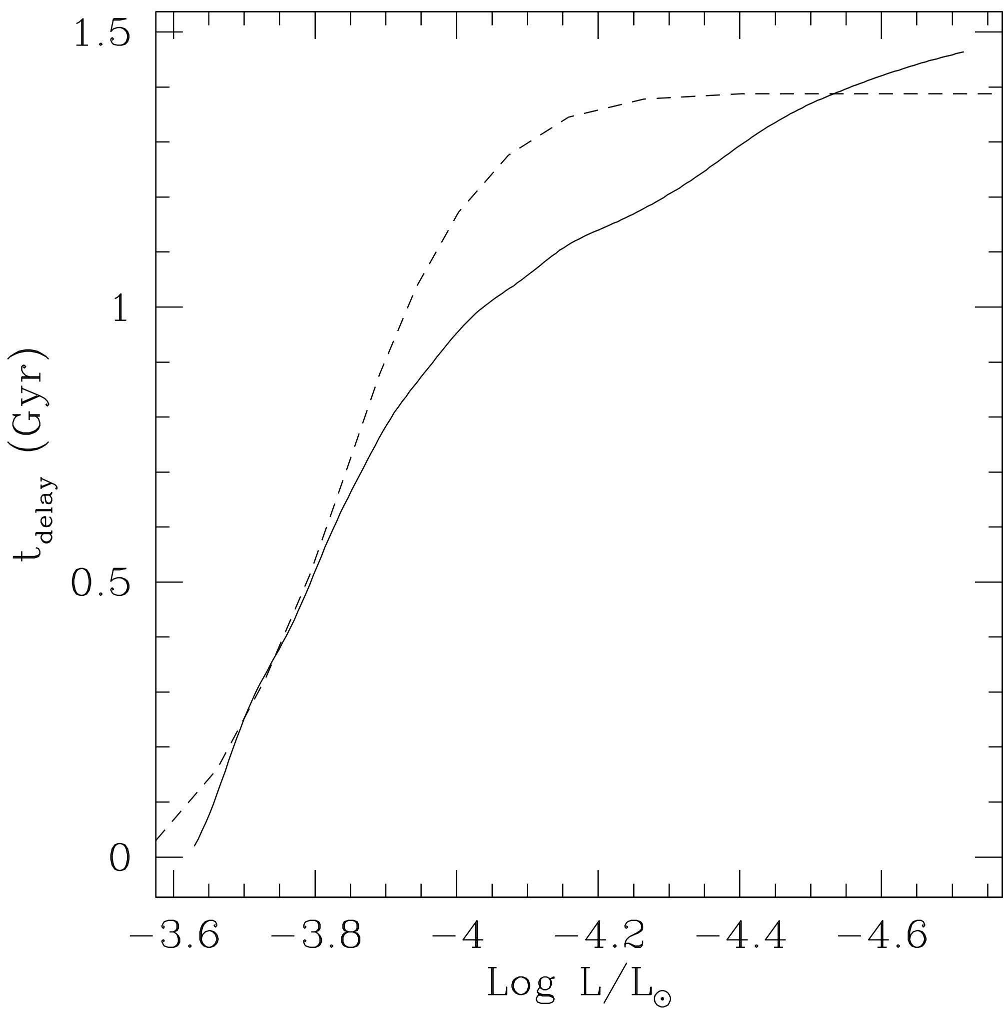

Fig. 2.6.— The solid line is the age difference between two 0.6 $M_\odot$ white dwarf evolutionary sequences with $Z = 0.0$, one of which is undergoing phase separation. The dotted line is the result of applying equation 2.4 to the evolutionary sequence undergoing phase separation, which yields an asymptotic value for the age delay of ~ 1.4 Gyr. At complete crystallization ($\log L/L_\odot \sim -4.6$), the value given by the direct evolutionary calculation is within 5% of this, indicating that the basic physics which is operating is well-described by equation 2.3.

1.38 Gyr and 0.62 Gyr, respectively. Thus, the initial composition profile has a large effect on the calculated age delays. In addition, the Ichimaru et al. (1988) phase diagram produces smaller composition changes and hence smaller values, reducing the Segretain & Chabrier age delays by approximately one-third.

We now consider the effect of a nonzero metallicity in the opacity tables. The effect of varying the metallicity from $Z = 0.000$ to $Z = 0.001$ results in a change of less than 0.016% in the energies released, and is barely detectable numerically. The main effect of changing the metallicity is to affect the luminosity range at which the phase separation energy is released, which in turn affects the age delay, $t_{\rm delay}$. For both the homogeneous and stratified case, the average luminosity during crystallization changes by less than 3% as Z is varied from 0.000 to 0.001, and hence $t_{\rm delay}$ also changes by less than 3%. Thus, the age delay is essentially insensitive to the metallicity assumed for the opacities.

Finally, we summarize the effect of different surface layer masses in Table 2.3. For $M_{\rm He}/M_\star = 10^{-3}$ and $M_{\rm H}/M_\star = 10^{-5}$ (comp1), we find maximum age delays of 1.45 Gyr, and for $M_{\rm He}/M_\star = 10^{-4}$ and $M_{\rm H}/M_\star = 10^{-6}$ (comp2), our maximum calculated age delay is 1.56 Gyr. These values represent increases of 5% and 13%, respectively, over the age delays calculated in our fiducial

Table 2.2. Age Delays for $0.6M_\odot$ Models

Initial Profile	Delay (Gyr) SC	IIO
50:50 homogeneous	1.38	0.99
stratified (Salaris et al. 1997)	0.62	0.39
stratified (Wood 1995)	0.30	0.20

model. For clarity, we note that these calculations are for the age differences introduced by phase separation alone at these new surface layer masses; the white dwarf ages themselves change significantly with He layer mass, which produces a decrease in the calculated ages (without including phase separation) of ~ 0.75 Gyr for each order of magnitude increase in M_{He}. Again, we find that varying the metallicity in the opacities has a small effect on these numbers, at only the 1% level.

6.2. The Mass Dependence

The mass of the white dwarf model affects the process of phase separation in two main ways, as is illustrated in Figure 2.7. First, a more massive white dwarf has a higher gravity so that more energy is released by the subsequent rearrangement of matter. Second, the luminosity at which crystallization occurs is higher for a more massive white dwarf, which tends to lessen the age-delay for a given energy release. For example, even though the total energy released in a 1.2 $M_\odot$ model increases by a factor of ~ 10, the average luminosity increases by a factor of ~ 30, and hence there is a net decrease in the time delay relative to the 0.6 $M_\odot$ sequence.

Table 2.3. Age Delays for $0.6 M_\odot$ Models with Different Surface Layer Masses

Initial Profile	Delay (Gyr)			
	comp1		comp2	
	SC	IIO	SC	IIO
50:50 homogeneous	1.45	1.04	1.56	1.12
stratified (Salaris et al. 1997)	0.66	0.42	0.71	0.44
stratified (Wood 1995)	0.32	0.21	0.34	0.23

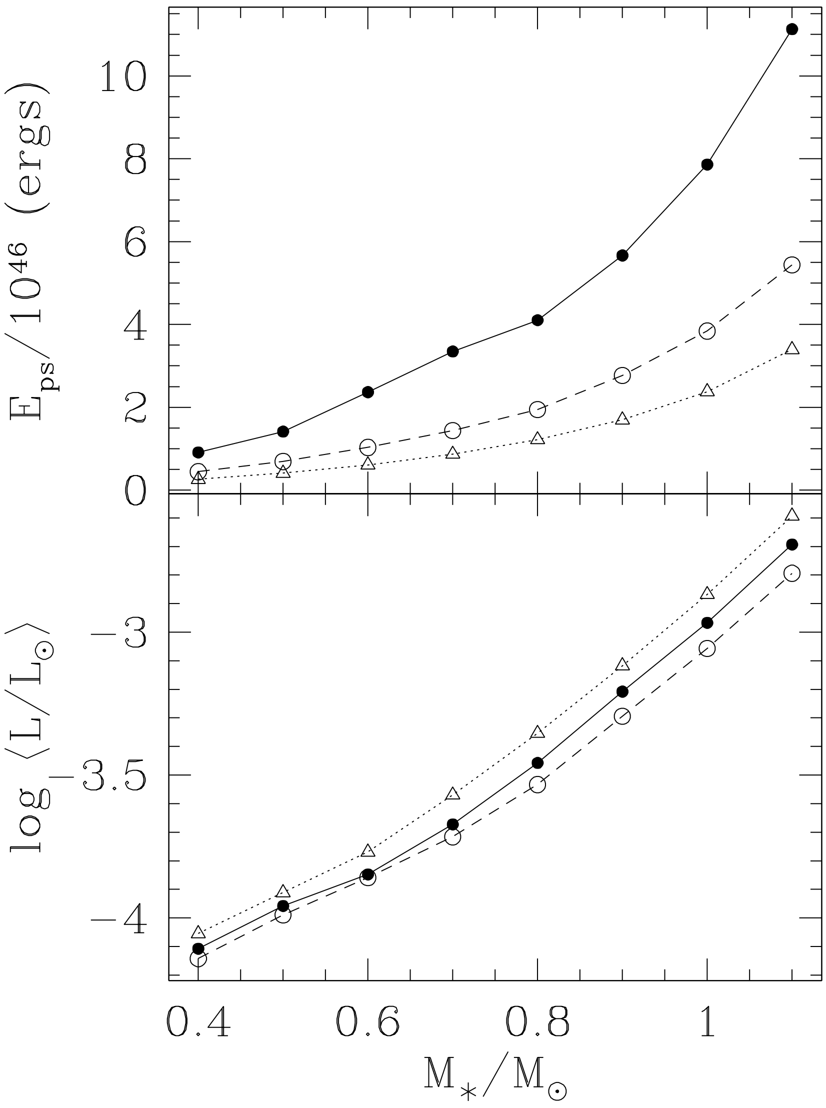

Fig. 2.7.— Phase separation energy and average luminosity as a function of mass. The solid curves are for initially homogeneous 50:50 C/O mixtures, the dashed curves are for the stratified C/O profile of Figure 2.4 (Salaris et al. 1997), and the dotted curves are for the stratified C/O profile of equation 2.7 (Wood 1995). The upper panel shows the phase separation energy released as a function of total stellar mass, and the lower panel shows the average luminosity during the crystallization process, also as a function of total stellar mass.

The competition of these two effects suggests that there may be a mass for which there is a maximum age-delay, for a fixed composition profile. This is indeed the case, as is demonstrated in Figure 2.8. We find that the 0.6 $M_\odot$ white dwarf models have the maximum age-delays for a given composition profile (this was also found by Segretain et al. 1994). The calculated age delay is only weakly dependent upon the metallicity, as can be seen from the small difference between the solid and dashed curves. It is strongly dependent upon the initial profile, however, which can decrease the energy release, and hence the age-delays, by a factor of three or more, as is shown in Figure 2.8.

From the preceding calculations we find that the two most important factors influencing the magnitude of the age delays introduced by the physics of phase separation are the *mass* of the white dwarf model and its *initial* C/O profile. Because the mass range of observed white dwarfs is strongly peaked around $0.6 M_\odot$ (e.g., Lamontagne et al. 1997), we find that the age delay we calculate is near the maximum possible with respect to this parameter. In terms of the initial C/O profile, however, the situation is reversed. For a $0.61 M_\odot$ white dwarf model, the profile calculated by Salaris et al. (1997) reduces the age delay by a factor of ~ 2 from the 50:50 homogeneous case. Using the profile of Wood (1995), which is based on results from Mazzitelli & D'Antona (1986) and D'Antona & Mazzitelli (1989), the reduction factor is ~ 5.

If we take as our best guess the initial profile of Salaris et al. (1997), assume a $0.6 M_\odot$ white dwarf model with $M_{\rm He}/M_\star = 10^{-2}$ and $M_{\rm H}/M_\star = 10^{-4}$, and use both the Segretain & Chabrier (1993) and Ichimaru, Iyetomi, & Ogata (1987) phase diagrams, then we obtain age delays in the range of 0.4–0.6 Gyr.

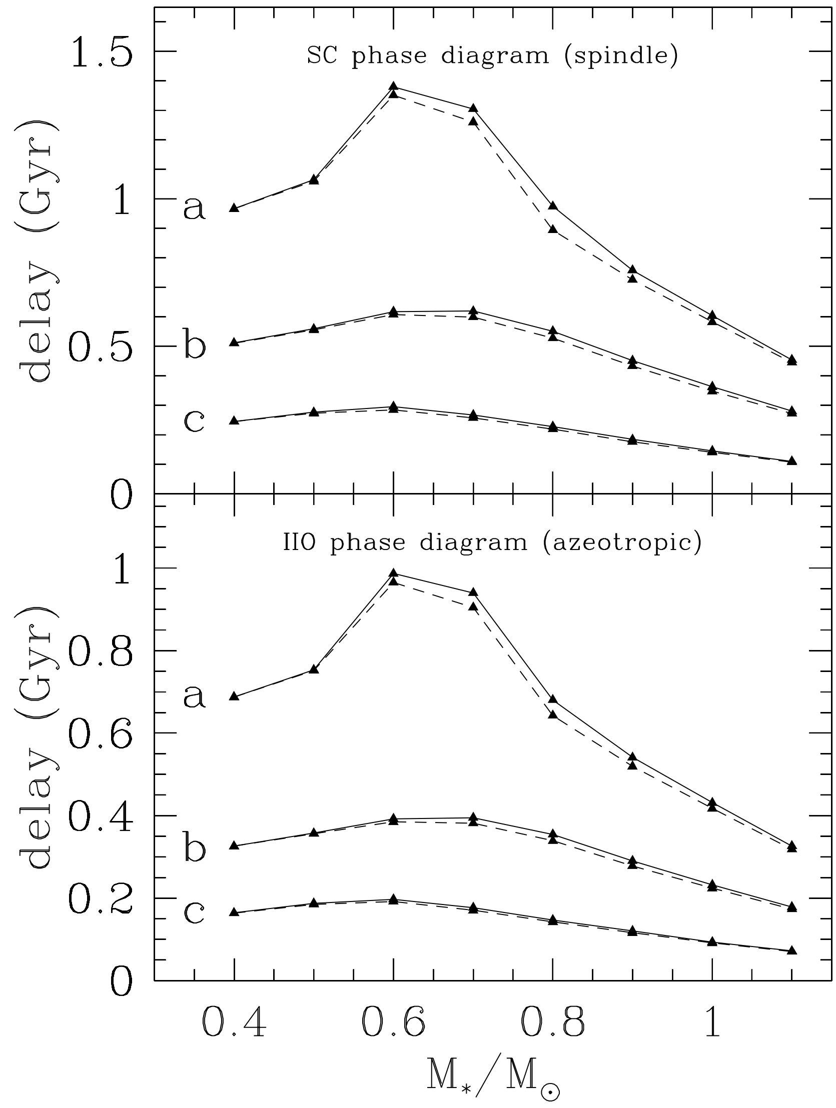

Fig. 2.8.— Age delay due to phase separation during crystallization as a function of total mass of the white dwarf model. Curve (a) corresponds to a 50:50 homogeneous initial C/O profile, while curves (b) and (c) are the initial profiles shown by the solid lines in Figures 2.4 and 2.3, respectively. The solid lines are for zero metallicity opacities and the dashed lines are for $Z = 0.001$, which shows that our result has little metallicity dependence. All models have $M_{\rm He}/M_\star = 10^{-2}$ and $M_{\rm H}/M_\star = 10^{-4}$.

7. Conclusions

We find a maximum age delay of ~ 1.5 Gyr due to phase separation for our fiducial white dwarf model ($M_\star = 0.6M_\odot$) and a best guess age delay of 0.4–0.6 Gyr. Salaris et al. (1997) have recently calculated a value of ~ 1 Gyr, using the evolutionary models of Wood & Winget (1989). If we scale their value to our present models (assuming an average luminosity during crystallization for their models of $\log L/L_\odot \simeq -4.1$), then we obtain 0.75 Gyr, which is in basic agreement with our estimate of 0.62 Gyr. The differences in these models are mainly due to the different surface layer masses adopted; more recent asteroseismological analyses of the class of DA's suggests that the appropriate surface layer masses are $M_{\rm He}/M_\star \sim 10^{-2}$ and $M_{\rm H}/M_\star \sim 10^{-4}$ (Clemens 1993, 1995), and these are the values which we have assumed.

The most important factors influencing the size of the calculated age delay are the total stellar mass and the initial composition profile. We find the largest age delays occur in models with masses of $\sim 0.6M_\odot$, near the peak in the observed white dwarf mass distribution. The best current theoretical initial C/O profile produces models with smaller age delays, of ~ 0.6 Gyr. In addition, if we use the phase diagram of Ichimaru et al. (1988) instead of the Segretain & Chabrier (1993) phase diagram, then our age delays are reduced by about one-third. We note that the prescription which we have adopted for the mixing during crystallization provides an upper bound for the efficiency of this process, and hence a maximum for the age delay. More realistic treatments of the mixing process may reduce the age delay. We find that varying the opacities (via the metallicity) and the surface layer masses has only a small effect ($\lesssim$ 10%) on the calculated age delays.

Our calculations do not take into account the possible age delays introduced by the phase separation of heavier trace-element species such as ^{22}Ne, which may produce significant age delays of 2–3 Gyr (Segretain et al. 1994; Hernanz et al. 1994). These species would arise from the initial abundance of metals in the main-sequence stars which later evolved into white dwarfs. This effect may only be important for Population I stars, however, and would not therefore affect the calculated ages of the cool white dwarfs which populate the turndown in the WDLF, since these white dwarfs were formed very early in the history of the Galaxy (Hernanz et al. 1994). We are currently investigating the possibility that the magnitude of the theoretical spike in the WDLF produced by ^{22}Ne deposition, if real, can be used as a diagnostic of the initial metallicity of Galactic clusters and possibly some globular clusters, once sufficiently complete observations can be made for a given cluster.

In the context of Galactic evolution, mean age estimates for the oldest Galactic globular clusters (GCs) have recently decreased. For example, Chaboyer et al. (1998) derive a value of 11.5 ± 1.3 Gyr for these GC's. Given the best fit age of $9.5^{+1.1}_{-0.8}$ Gyr which Oswalt et al. (1996) derive from their observed WDLF, there may only be a difference of ~ 2 Gyr between GC ages and WDLF ages. In fact, we would expect a delay of at least 1–2 Gyr from the onset of GC formation to the formation of the Galactic disk, and possibly a much larger delay, depending on the Galactic formation model used (Burkert, Truran, & Hensler 1992; Chiappini, Matteucci, & Gratton 1997). Our results are consistent with this state of affairs since we conclude that the maximum effect which the phenomenon of phase separation can have on the modeled ages of the coolest white dwarfs is of order 1.5 Gyr, and is most likely in the 0.6

Gyr range.

Chapter 3

Pulsations and Crystallization

1. Astrophysical Context

The theoretical study of pulsating crystalline objects extends many years into the past. One of the first numerical studies was by Alterman, Jarosch, & Pekeris (1959), who modeled global oscillations of the Earth. Their main interest was in fitting the oscillation period of 57 minutes which was excited by the Kamchatka earthquake of 1952. In the process, they examined how the central density in their models allowed them to match the periods of other oscillation modes which were also observed to be excited by the earthquake.

In an astrophysical context, Hansen & Van Horn (1979) treated oscillations in white dwarf models with a crystalline inner core. Since it was known that 1 $M_\odot$ models with $T_{\rm eff} \sim 10{,}000$ K were in the process of crystallizing (Lamb & Van Horn 1975; Van Horn & Savedoff 1976), Hansen & Van Horn self-consistently treated the response of the crystalline core to the pulsations. Their main interest was in explaining the observed period ranges of the ZZ Ceti's in terms of low radial order oscillations. They found that the g-mode periods were decreased by the presence of crystallization, which is contrary to our present findings.

McDermott, Van Horn, & Hansen (1988) treated oscillations in neutron star models with a fluid core, a solid crust, and a thin surface fluid "ocean." They considered neutron star oscillations as a possible explanation for the observed irregularities in the timing of subpulses from radio pulsars, and as a source of the observed periodicities in many X-ray burst sources. Theoretically, they found g-modes which were trapped in the cores of their models, as well as those which were trapped in the surface oceans.

Finally, Bildsten & Cutler (1995) considered g-mode oscillations in the thin surface oceans of accreting neutron star models. Their aim was to explain the observed 5–7 Hz quasi-periodic oscillations in the brightest accreting neutron star systems. They found a good match to these frequencies for low order, $\ell = 1$ g-modes.

Why, then, does this problem need to be re-examined in the context of white dwarf stars? As is usually the case in science, new observations and new circumstances have again made this problem one worth considering, but in more detail than the general analyses of the past. For example, Hansen & Van Horn (1979) were concerned primarily with the range of normal mode periods which are possible given a crystallized core, not with any of the details of how the periods of high overtone g-modes are affected at the level of 5–10%. At the time, there were no known high-mass white dwarf pulsators, and precise mode identifications for *any* pulsating white dwarf had yet to be done.

That situation has changed with the discovery of pulsations in BPM 37093 (Kanaan et al. 1992), a high-mass ZZ Ceti (see Figure 3.1) which should be substantially crystallized (Winget et al. 1997); depending on the C/O ratio in its core, it should be between 50% and 90% crystallized by mass. The Whole

Earth Telescope (WET) examined this target in the Spring of 1998 and found at least 8 independent frequencies, three of which had been previously seen by Kanaan (1996). Thus, the potential to perform asteroseismology on this object requires us to make a more detailed theoretical investigation of this class of objects.

One hope is that we will be able to independently determine the crystallized mass fraction $M_{\mathrm{xtal}}/M_{\odot}$, and thereby provide a direct test of the theory of crystallization, now over three decades old (Abrikosov 1960; Kirzhnits 1960; Salpeter 1961). This subject is relevant to the astronomical community at large, since phase separation of C and O during crystallization, and, indeed, crystallization itself, represent the largest sources of systematic uncertainties in the age of the local Galactic disk as derived from the white dwarf luminosity function. In addition, understanding the internal structure of white dwarfs may prove vital in fitting cosmological models to Supernova Ia (SNIa) data (Garnavich et al. 1998), so that systematic differences in the absolute magnitudes of the SNIa may be corrected for the evolutionary differences in the SN progenitors (Höflich, Wheeler, & Thielemann 1998).

2. Review of Nonradial Oscillation Theory

2.1. The Fluid Equations

To a first approximation, most stars may be thought of as fluid spheres. Since we are interested only in an adiabatic analysis, we may write the fluid equations for conservation of mass and momentum, supplemented by the equation for the gravitational potential, which must be satisfied locally (see the discussion in

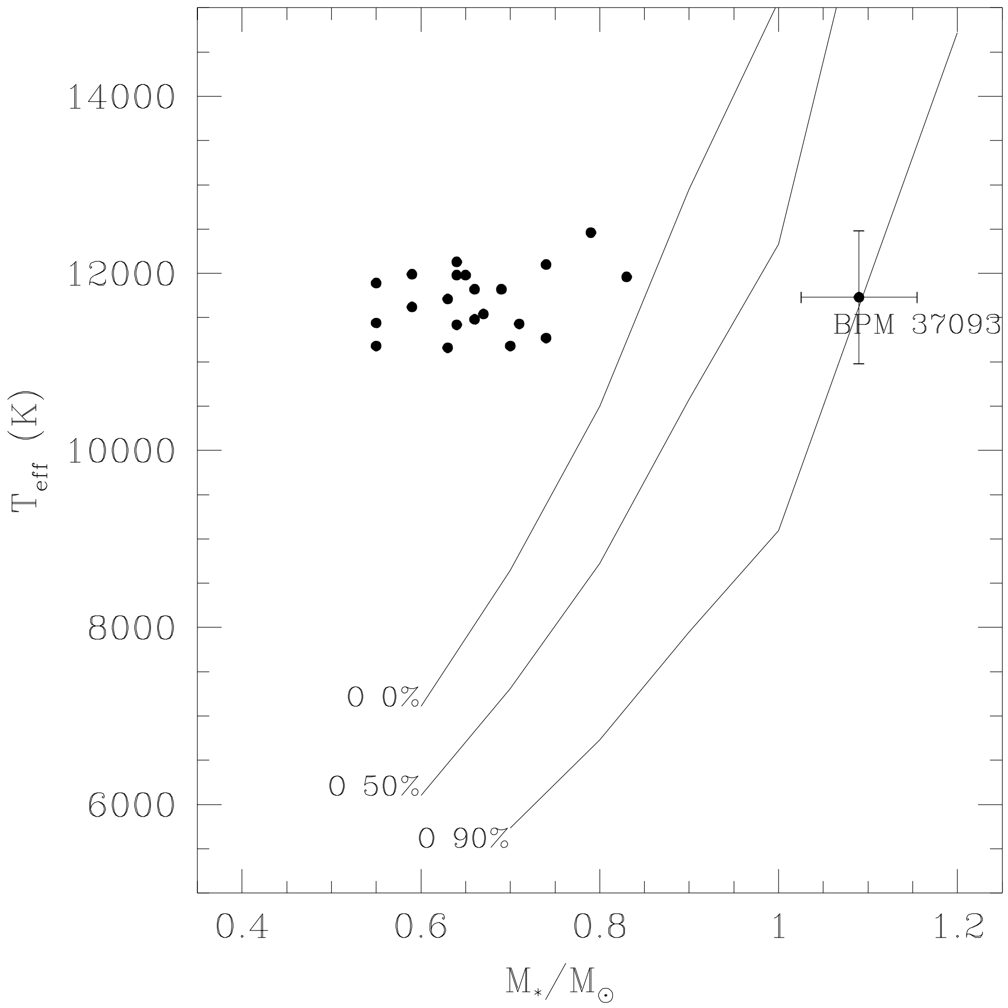

Fig. 3.1.— The position of BPM 37093 relative to the other ZZ Ceti's in Bergeron et al. 1995 as a function of $T_{\rm eff}$ and $M_\star/M_\odot$. The lines correspond to constant amounts of crystallized mass fraction assuming a pure oxygen core. If BPM 37093 has an oxygen core it should be $\sim$ 90% crystallized, and for a carbon core, $\sim$ 50% crystallized.

Unno et al. 1989 for the following derivation):

$$\frac{\partial \rho}{\partial t} + \vec{\nabla} \cdot (\rho \vec{u}) = 0 \tag{3.1}$$

$$\rho(\frac{\partial}{\partial t} + \vec{u} \cdot \vec{\nabla})\vec{u} = -\vec{\nabla} p - \rho \vec{\nabla} \Phi, \tag{3.2}$$

$$\nabla^2 \Phi = 4\pi G \rho \tag{3.3}$$

where ρ is the density, $\vec{u}$ is the velocity field, p is the pressure, Φ is the gravitational potential, and G is the universal constant of gravitation. Here we are explicitly ignoring viscous, electromagnetic, and external forces.

We now wish to perturb these equations to obtain the oscillation equations. If we make an Eulerian perturbation of these equations and then assume that the equilibrium configuration is a static one (i.e., $\vec{u} = 0$ and $d\rho/dt = 0$), then we obtain

$$\frac{\partial \rho'}{\partial t} + \vec{\nabla} \cdot (\rho \vec{v}) = 0 \tag{3.4}$$

$$\rho \frac{\partial \vec{v}}{\partial t} = -\vec{\nabla} p' - \rho' \vec{\nabla} \Phi - \rho \vec{\nabla} \Phi', \tag{3.5}$$

$$\nabla^2 \Phi' = 4\pi G \rho' \tag{3.6}$$

where we have written the perturbed velocity field $\vec{u'}$ as $\vec{v}$. Since we wish to search for modes of the system, we assume a time dependence for all perturbed quantities of $e^{i\sigma t}$, e.g., $\rho'(t, \vec{r}) \equiv \rho'(\vec{r}) e^{i\sigma t}$. Since the velocity is just the time derivative of the displacement $\vec{\xi}$, we now have

$$\rho' + \vec{\nabla} \cdot (\rho \vec{\xi}) = 0 \tag{3.7}$$

$$\rho \sigma^2 \vec{\xi} = \vec{\nabla} p' + \rho' \vec{\nabla} \Phi + \rho \vec{\nabla} \Phi' \tag{3.8}$$

for the fluid equations, while equation 3.6 for the gravitational potential is unchanged in form.

The final assumption which we will make is that the initial equilibrium model is spherical. This is a good approximation for stars with weak magnetic fields and which are slowly rotating, and it has been shown to hold observationally for individual white dwarfs and pre-white dwarf objects (Winget et al. 1991; Winget et al. 1994). This assumption means that $\rho(r)$ and $\Phi(r)$ are a function of the radial distance r only.

The assumption of spherical symmetry makes possible a particular separation of variables, in which $\rho'(\vec{r}) = \rho'(r)Y_\ell^m(\theta,\phi)$, and similarly for p' and Φ'. The displacement eigenfunction is given by

$$\vec{\xi} = \left[\xi_r(r), \xi_h(r)\frac{\partial}{\partial\theta}, \xi_h(r)\frac{1}{\sin\theta}\frac{\partial}{\partial\phi}\right] Y_\ell^m(\theta,\phi), \tag{3.9}$$

where

$$\xi_h(r) = \frac{1}{\sigma^2 r}\left(\frac{p'}{\rho} + \Phi'\right). \tag{3.10}$$

In the above formulae, ξ_r and ξ_h are the radial and horizontal displacements, respectively, associated with a given mode of frequency σ.

Substituting the above forms in equations 3.6–3.8 and skipping many steps, we arrive at the following three equations (Unno et al. 1989):

$$\frac{1}{r^2}\frac{d}{dr}(r^2\xi_r) - \frac{g}{c_s^2}\xi_r + \left(1 - \frac{L_\ell^2}{\sigma^2}\right)\frac{p'}{\rho c_s^2} = \frac{\ell(\ell+1)}{\sigma^2 r^2}\Phi' \tag{3.11}$$

$$\frac{1}{\rho}\frac{dp'}{dr} + \frac{g}{\rho c_s^2}p' + (N^2 - \sigma^2)\xi_r = -\frac{d\Phi'}{dr} \tag{3.12}$$

$$\frac{1}{r^2}\frac{d}{dr}\left(r^2\frac{d\Phi'}{dr}\right) - \frac{\ell(\ell+1)}{r^2}\Phi' = 4\pi G\rho\left(\frac{p'}{\rho c_s^2} + \frac{N^2}{g}\xi_r\right), \tag{3.13}$$

where g is the acceleration due to gravity, c_s is the sound speed,

$$L_\ell^2 \equiv \ell(\ell+1)c_s^2/r^2$$

is the Lamb acoustic frequency, and

$$N^2 \equiv g\left(\frac{1}{\Gamma}\frac{d\ln p}{dr} - \frac{d\ln\rho}{dr}\right) \tag{3.14}$$

is the famed Brunt-Väisälä frequency. Since equation 3.13 is a second-order equation for Φ', this equation is equivalent to two first-order equations. Thus, the three equations 3.11–3.13 represent a fourth-order problem for the solution of linear, adiabatic oscillations of a spherical model star.

2.2. Asymptotic Theory

In this section we perform a local analysis which forms the basis for our understanding of mode propagation in white dwarf stars. To begin, we make the Cowling approximation (Cowling 1941), which simply says that we will ignore perturbations to the gravitational potential Φ and its derivatives. This is a valid approximation in the high ℓ and high k limit, and is also a very good approximation for g-modes in white dwarf stars, which are primarily envelope modes; we have found numerically that the Cowling approximation affects the mode periods at less than a 0.2% level, even for $k = 1$, $\ell = 1$ modes. As a result of this approximation, we do not need to consider equation 3.13 any further.

For equations 3.11 and 3.12, we make the following change of variables (Unno et al. 1989):

$$\tilde{\xi} \equiv r^2\xi_r \exp\left(-\int_0^r \frac{g}{c_s^2}dr\right) \tag{3.15}$$

$$\tilde{\eta} \equiv \frac{p'}{\rho}\exp\left(-\int_0^r \frac{N^2}{g}dr\right) \tag{3.16}$$

This results in two coupled, first-order equations for $\tilde{\xi}$ and $\tilde{\eta}$:

$$\frac{d\tilde{\xi}}{dr} = h(r)\frac{r^2}{c_s^2}\left(\frac{L_\ell^2}{\sigma^2} - 1\right)\tilde{\eta} \tag{3.17}$$

$$\frac{d\tilde{\eta}}{dr} = \frac{1}{r^2 h(r)} \left(\sigma^2 - N^2\right) \tilde{\xi}, \tag{3.18}$$

where

$$h(r) \equiv \exp\left[\int_0^r \left(\frac{N^2}{g} - \frac{g}{c_s^2}\right) dr\right].$$

If we now search for solutions which are locally propagating in space, i.e.,

$$\tilde{\xi}, \tilde{\eta} \propto \exp(ik_r r),$$

then we find

$$k_r^2 = \frac{1}{\sigma^2 c_s^2}(\sigma^2 - L_\ell^2)(\sigma^2 - N^2), \tag{3.19}$$

which is a local dispersion relation relating the frequency of a mode σ to its spatial radial wavenumber, k_r.

In order for a mode to be propagating in a given region, we must have k_r real, i.e., $k_r^2 > 0$. If we consider the high-frequency limit of equation 3.19 for $\sigma^2 \gg L_\ell^2$, N^2, then we find that

$$k_r = \frac{\sigma}{c_s}.$$

From a complete asymptotic analysis, we find a condition analogous to the Bohr-Sommerfeld quantization condition, namely $\int k_r dr = k\pi$. Inserting this here, we find

$$\sigma_k = \frac{\pi k}{\int_{r1}^{r2} dr/c_s}, \tag{3.20}$$

where $r1$ and $r2$ are the inner and outer turning points where $k_r = 0$. We see that the frequency of these modes depends mainly on the sound speed, so the primary restoring force for these modes is pressure; these modes are therefore called p-modes. We note that the frequencies of these modes as a function of radial overtone number k are evenly spaced.

Taking the low-frequency limit of equation 3.19 ($\sigma^2 \ll L_\ell^2,\ N^2$), we obtain

$$k_r = \frac{L_\ell N}{\sigma c_s} = \frac{[\ell(\ell+1)]^{1/2} N}{r}\frac{1}{\sigma}.$$

Applying the same quantization condition, we find that the frequency relation is

$$\sigma_k = \frac{[\ell(\ell+1)]^{1/2}}{k\pi}\int_{r1}^{r2}\frac{N}{r}dr, \tag{3.21}$$

or in terms of period this reads

$$P_k = \frac{k\pi}{[\ell(\ell+1)]^{1/2}}\left[\int_{r1}^{r2}\frac{N}{r}dr\right]^{-1}. \tag{3.22}$$

This relation depends only on the Brunt-Väisälä frequency, which is the local oscillation frequency for fluid elements due to buoyant/gravitational return forces; these modes are therefore called g-modes. We see that the g-modes are evenly spaced in period as a function of k, in contrast to the p-modes.

We now wish to derive a relation between the horizontal and vertical displacements of a mode near the surface. If we take as an idealized outer boundary condition that the pressure and density vanish there, then the Lagrangian variation of the pressure should also be zero, i.e., $\delta P = 0$. Since the connection between Lagrangian and Eulerian variations of a function f is

$$\delta f = f' + \vec{\xi}\cdot\nabla f,$$

this condition translates into

$$\begin{aligned} 0 &= P' + \vec{\xi}\cdot\nabla P \\ &= P' + \xi_r\frac{dP}{dr} \\ &= P' - \rho g \xi_r, \end{aligned}$$

so

$$P' = \rho g \xi_r, \tag{3.23}$$

where we have used the condition of hydrostatic equilibrium. Since we are employing the Cowling approximation ($\Phi' = 0$), equation 3.10 gives P' as

$$P' = \rho\sigma^2 r\xi_h,$$

which combined equation 3.23 gives the following relation for the ratio of horizontal to vertical displacements at and near the surface:

$$\frac{\xi_h}{\xi_r} = \frac{GM}{R^3\sigma^2}. \tag{3.24}$$

Here, M and R are the total stellar mass and radius of the model, respectively.

We see from equation 3.24 that the low-frequency g-modes have $\xi_h \gg \xi_r$, which means that the displacements near the surface are mainly horizontal. For the high-frequency p-modes we have $\xi_r \gg \xi_h$, so these modes have predominantly vertical displacements near the surface. We summarize these results for the two different classes of spheroidal modes below:

p-modes

$\sigma^2 > L_\ell^2, N^2$, "high-frequency limit"

$\sigma_k \sim \frac{k\pi}{\int_{r1}^{r2} dr/c_s}$

displacements become vertical near the surface

frequencies of consecutive radial overtones are evenly spaced

g-modes

$\sigma^2 < L_\ell^2, N^2$, "low-frequency limit"

$P_k \sim \frac{2\pi^2 k}{\sqrt{\ell(\ell+1)}} \left[\int_{r1}^{r2} N dr/r\right]^{-1}$

displacements become horizontal near the surface

periods of consecutive radial overtones are evenly spaced

Based on these considerations, the pulsational properties of a model are locally determined by N^2 and L_ℓ^2. Thus, the radial dependence of these two functions is a useful diagnostic for the frequency spectrum of a given white dwarf model. We call such a plot a "propagation diagram," an example of which is shown in Figure 3.2, where we have labelled the high- and low-frequency domains of the p- and g-modes. We note that the bumps in N^2 and L_ℓ^2 correspond to C/O, He/C, and H/He transition zones. We use the modified Ledoux prescription as outlined in Brassard et al. (1991) to compute the Brunt-Väisälä frequency in a composition transition zone. In addition, we sometimes use the Schwarzschild criterion, which ignores the changing composition profiles and uses equation 3.14 directly. Although this is unphysical, it often has the useful side effect of minimizing the contribution of the transition zones, which is useful for comparison purposes.

Finally, to remind ourselves of the horizontal nature of g-mode pulsations implied by equation 3.24, as well as the angular structure contained in 3.9, we show a cross-sectional view of a particular g-mode in Figure 3.3, where the arrows indicate the direction of motion of a given fluid element. The mode pictured is a spheroidal mode with $\ell = 1$ and $m = 0$. The cross section which we have taken is a plane which intersects the polar axis of the model. The radial coordinate is again taken to be $x = \ln r/p$.

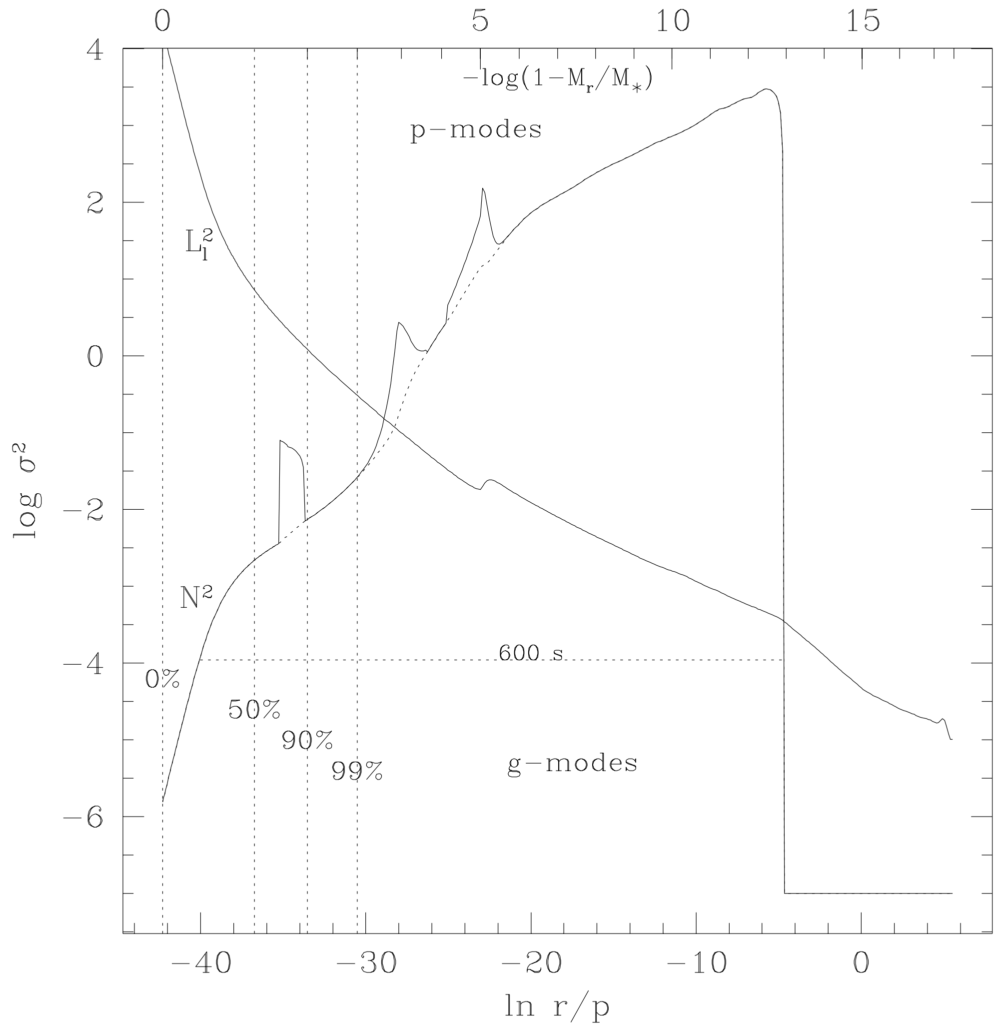

Fig. 3.2.— A propagation diagram showing N^2 and L_ℓ^2 as a function of $\ln r/p$ (lower axis) and $-\log(1-M_r/M_\star)$ (upper axis); the center is on the left and the surface is on the right. The region of propagation of a 600 second g-mode is shown. The vertical dashed lines are labelled by the percent mass which is interior to these regions, i.e., the 90% line indicates the boundary at which 90% of the mass of the model is inside this point. We see that a model which is this crystallized now has an inner turning point for g-mode propagation considerably farther out than in the uncrystallized case.

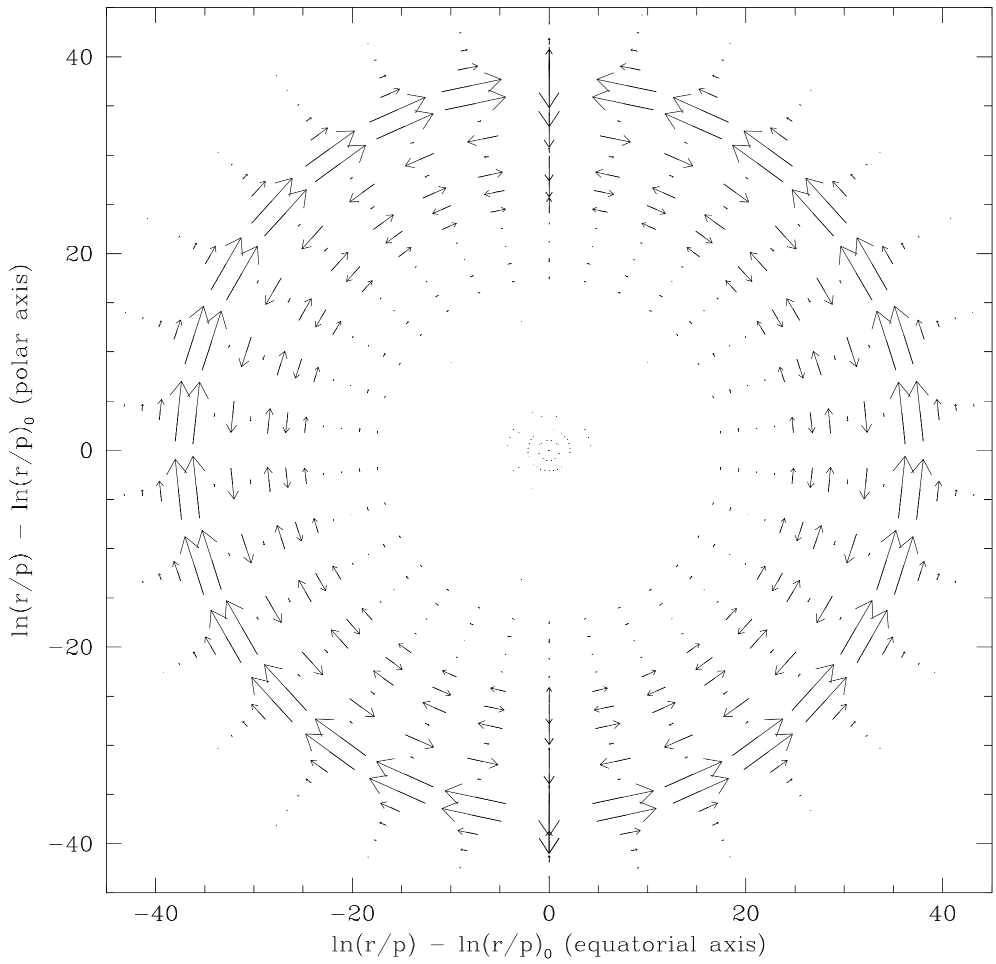

Fig. 3.3.— A cross-sectional view of an $\ell = 1, m = 0$ g-mode, where the arrows indicate the direction of motion of the fluid elements. The motions are mainly horizontal, with a considerable amount of shear between different radial layers.

3. The Effect of a Crystalline Core

How does a crystalline core affect the oscillations of a star? As we introduce a solid core into our models, two things occur: (1) A new class of modes appears (the torsional/toroidal modes, in this case), and (2) the pre-existing p- and g-modes are modified. We now treat these cases separately.

3.1. The Torsional Modes

The torsional modes, or t-modes, are very special nonradial modes characterized by zero radial displacement and zero compression, i.e., ξ_r and $\vec{\nabla} \cdot \vec{\xi}$ both vanish, where $\vec{\xi}$ is the displacement vector. In the context of general stellar pulsation models, these modes are called toroidal modes. In models which are non-magnetic and non-rotating and are fluid throughout, these modes have zero frequency and therefore correspond to steady-state fluid motions. In the case of nonzero rotation, these modes can have nonzero frequencies and are called Rossby or r-modes. The presence of solid regions in a model with finite shear also allows the toroidal modes to have a nonzero frequency. In this case, we call the modes torsional or t-modes.

Waves may propagate such that either the displacement of the material medium is parallel to the direction of propagation of the wave, or is perpendicular to it. Landau & Lifshitz (1975) use the nomenclature longitudinal and transverse, respectively, for such waves propagating in a solid. In the geophysical literature, these waves are also commonly referred to as pressure (P) and shear (S) waves, respectively. The square of the velocity of propagation for each is

$$v_p^2 = \frac{\lambda + 2\mu}{\rho} \tag{3.25}$$

$$v_s^2 = \frac{\mu}{\rho}, \tag{3.26}$$

where λ and μ are the Lamé elastic coefficients, with λ defined by

$$\begin{aligned} \lambda &\equiv K - \frac{2}{3}\mu \\ &= \Gamma_1 P - \frac{2}{3}\mu, \end{aligned}$$

where $K = \Gamma_1 P$ is the bulk modulus. The quantity μ is also known as the shear modulus. We use the expression for it given in Hansen & Van Horn (1979),

$$\mu \sim 0.37n\frac{(Ze)^2}{a},$$

where a is the radius of a sphere containing one ion of charge Ze, and $1/n = (4/3)\pi a^3$. As we will show, none of our results depend sensitively on the precise value of the shear modulus.

In the following, we use the equations derived by Hansen & Van Horn (1979) for t-mode oscillations in order to obtain a local dispersion relation for these modes. The displacement eigenfunction for the t-modes has the following separation:

$$\vec{\xi} = \left[0\,, \xi_h(r)\frac{1}{\sin\theta}\frac{\partial}{\partial\phi}, -\xi_h(r)\frac{\partial}{\partial\theta}\right] Y_\ell^m(\theta,\phi). \tag{3.27}$$

If we now define

$$z_1 = \frac{\xi_h(r)}{r^2},$$

$$z_2 = \frac{\mu}{r}\left(\frac{d\xi_h(r)}{dr} - \frac{\xi_h(r)}{r}\right),$$

the equations of oscillation become

$$\begin{aligned} r z_1' &= -z_1 + \frac{1}{\mu} z_2 \\ r z_2' &= [\mu(\hat{\ell}-2) - \sigma^2 \rho r^2] z_1 + 4 z_2, \end{aligned} \tag{3.28}$$

where $\hat{\ell} \equiv \ell(\ell+1)$ (Hansen & Van Horn 1979). If we rewrite these equations in terms of $\tilde{z}_1 = r z_1$ and $\tilde{z}_2 = z_2/r^4$, we have

$$\begin{aligned} r \tilde{z}_1' &= \frac{r^4}{\mu} \tilde{z}_2 \\ r \tilde{z}_2' &= \frac{1}{r^6} [\mu(\hat{\ell}-2) - \sigma^2 \rho r^2] \tilde{z}_1. \end{aligned} \tag{3.29}$$

If we assume that $\tilde{z}_1, \tilde{z}_2 \propto e^{i k_r r}$, then we find the local dispersion relation:

$$k_r^2 = \frac{1}{v_s^2} (\sigma^2 - T_\ell^2). \tag{3.30}$$

Here, $T_l^2 \equiv (\hat{\ell} - 2) v_s^2 / r^2$ is the "torsional frequency".

These modes propagate in regions which have nonzero shear (the crystallized regions) and which have $\sigma^2 > T_\ell^2$. Their frequency spectrum is equally spaced, as is the case with p-modes, with

$$\sigma_k \sim \frac{k\pi}{\int dr/v_s}.$$

As we might expect, the $k = 1$ period for these modes goes like $R_\star / v_s$, the crossing time for a shear wave; this period is typically of order 10–20 sec.

In Figure 3.4, we show a propagation diagram for t-modes with $\ell = 2$. If we imagine a model which is 90% crystallized, then the t-mode can potentially propagate anywhere inside the 90% mass point in the model. If the mode is an $\ell = 2$ mode, then its region of propagation is restricted further to the region for which its frequency is greater than the torsional frequency, i.e., $\sigma^2 > T_\ell^2$. For a 1 sec mode, this corresponds to the part of the horizontal dotted line which lies to the left of the 90% point. We note that for all the $\ell = 1$ modes, we have $T_\ell^2 = 0$, so these modes propagate through the entire crystallized region.

From an observational standpoint, the longest period t-modes should have periods $\sim$ 20 sec, which is too short to explain the oscillations observed in the ZZ Ceti's, which have periods in the 100's of seconds. In addition, these modes cannot couple (in the linear limit) to the fluid at the solid/fluid interface, so these oscillations cannot propagate from the crystalline core through the fluid to the surface. Also, the different angular structure of the t-modes (equation 3.27) should make any nonlinear coupling between these modes and the ordinary p- and g-modes very weak. To the first nonlinear order this coupling will be zero. We therefore expect these modes to be unobservable unless crystallization has proceeded out into the photosphere; the oldest white dwarfs in the Galaxy should still be far too hot for this to have occurred. We therefore turn our attention to the p- and g-modes.

3.2. The Spheroidal Modes

p-modes

For pressure waves in a solid medium, the velocity v_p is given by equation 3.25. If we treat the non-zero μ as a perturbation, we then find that

$$\frac{\delta v_p}{v_p} \sim \frac{2\mu}{3\Gamma_1 P},$$

where δv_p is the change in v_p due to the finite shear modulus. In the cores of our 1.1 $M_\odot$ models, we typically find $\mu/p \sim 0.01$. Thus, p-mode periods are affected at the level of only a few percent by the presence of a crystalline

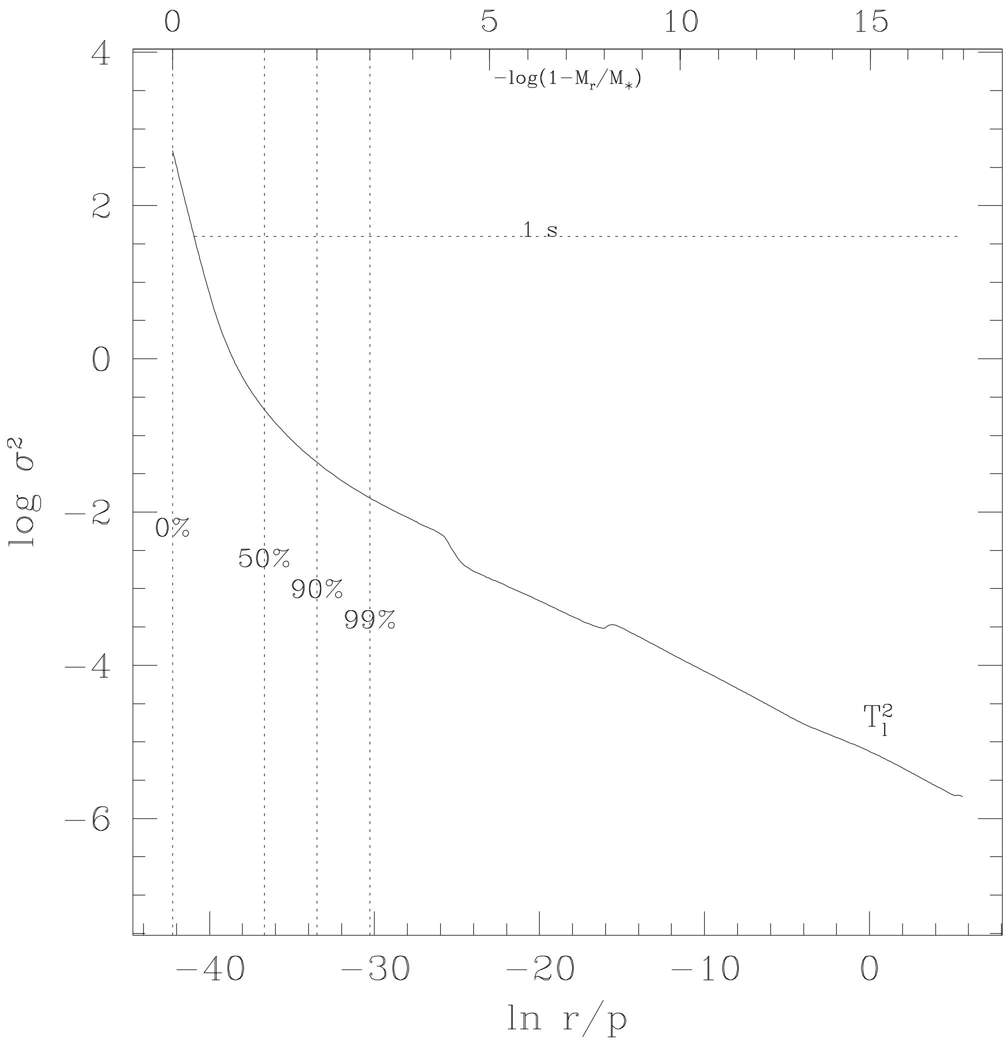

Fig. 3.4.— A propagation diagram for t-modes for $\ell = 2$. The t-modes propagate only in the crystallized region, e.g., only to the left of the 90% crystallized line for a 90% crystallized model. We note that for $\ell = 1$ we have $T_\ell^2 = 0$, so the modes propagate throughout the entire crystallized region in this case.

lattice. They are therefore of no more interest than are ordinary p-modes in the context of the observed pulsations of the DAV and DBV white dwarfs.

g-modes

We concentrate the remainder of our analysis on the g-modes, since these are the modes which are believed to be responsible for the pulsations observed in the white dwarf variables. Because g-modes have large shears associated with their fluid motions, we expect the nonzero shear modulus μ of the solid to have a significant effect on them. Qualitatively, we may ask when the return force due to a finite shear modulus is approximately equal to the return force normally experienced by fluid elements in the absence of such shear (e.g., Bildsten & Cutler 1995). Algebraically, the shear return force is equal to or exceeds the ordinary return force of the fluid when

$$\frac{\mu}{\rho\sigma^2 h^2} \geq 1,$$

where $h \equiv P/|dP/dr|$ is a pressure scale height.

In our models, we find that $\frac{\mu}{\rho\sigma^2 h^2} > 10^{10}$, which indicates that the g-modes are completely altered in the crystallized region. Thus, a g-mode which is propagating in the fluid region will find a complete mismatch as it attempts to propagate into the crystallized region. We therefore expect nearly complete reflection of the g-mode at such a boundary, with the result that the g-modes are essentially confined to the fluid regions of our models.

4. Numerical Analysis

4.1. The Global Solution

We now examine the above assertion and offer a numerical justification for it. Our approach is based on the work of Hansen & Van Horn (1979); we treat the "global" problem in that we allow the solid cores of our models to respond to the oscillations. We have used the Cowling approximation to simplify the pulsation equations, as was also done in Hansen & Van Horn (1979). Since g-modes in white dwarfs are primarily envelope modes, this is an excellent approximation and hardly affects the accuracy of our calculated periods, as was discussed at the beginning of section 2.2. The details of the rest of our treatment are summarized in Appendix A, where we describe the oscillation variables, the equations which they obey, the central boundary conditions, and the connecting conditions at the solid/fluid interface.

In Figure 3.5, we plot the radial and horizontal displacements of a particular mode. As is true of all the g-modes we have examined, the amplitude of the fluid motions is decreased by ~ 3 orders of magnitude in the solid as compared to the fluid. One other feature of the oscillations is that the horizontal displacement is discontinuous at the solid/liquid interface. In the approximation of zero viscosity and laminar flow, the fluid is free to slide over the solid surface. In reality, a turbulent boundary layer would probably form in this region, which would tend to dissipate the pulsation energy.

Since the kinetic energy density depends on the square of the displacement of a mode, we would expect it to be similarly attenuated in the solid core. This is indeed the case and is illustrated in Figure 3.6. Here we see that the

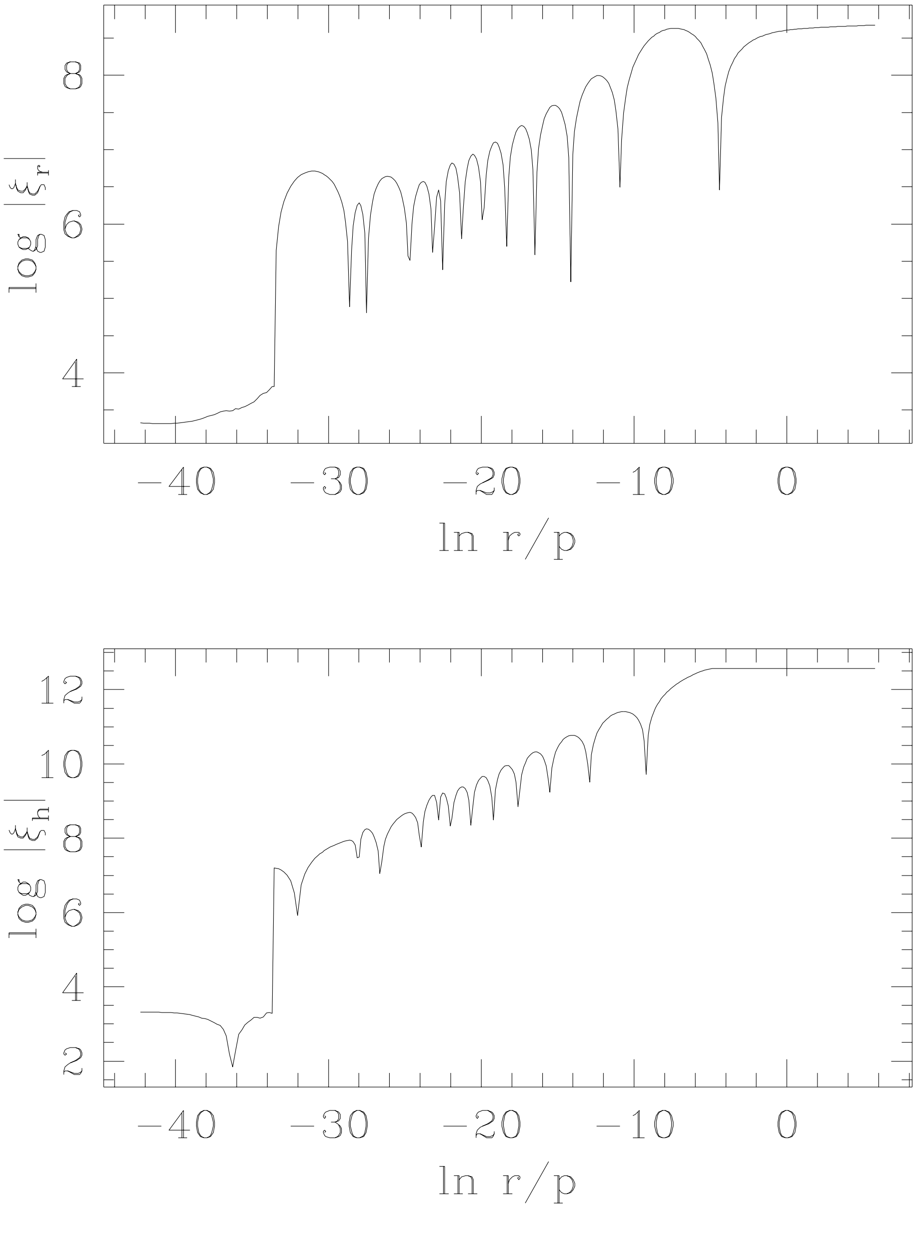

Fig. 3.5.— The log of the absolute values of the radial (upper panel) and horizontal (lower panel) displacements as a function of $\ln r/p$. Note that ξ_r is continuous at the solid/crystal interface at $\ln r/p \sim -34$, but that ξ_h is not. The magnitudes of both ξ_r and ξ_h are reduced by ~ 3 orders of magnitude as they penetrate the solid region.

kinetic energy is reduced by more than 6 orders of magnitude in the solid as compared to the liquid. Since the kinetic energy is an indicator of how a given mode samples the different regions of a model, we conclude that it is a very good approximation to treat the g-modes as excluded from the solid cores of our models. We will demonstrate the validity and the self-consistency of this approach in the following section.

4.2. The "Hard-Sphere" Boundary Condition

As suggested in the previous section, we may be able to reproduce the effects of crystallization on g-mode pulsations merely by applying a hard sphere boundary condition at the solid/liquid interface. By this we mean that the radial displacement is set to zero ($\xi_r = 0$) and the horizontal displacement is left to be arbitrary.

We have calculated the fractional difference between periods calculated with the "hard-sphere" approximation and those calculated with the "global" treatment. In Figure 3.7 we plot this difference for periods between 50 and 1000 sec with $\ell = 1$. The crystallized mass fraction is taken to be 0.9, and the mass of the model is 1.1 $M_{\odot}$. We find that the fractional difference in periods is less than 1 part in 10^4 for both $\ell = 1$ and 2 modes, and that the absolute error in the calculated periods over this range never exceeds 0.05 sec. We therefore conclude that the "hard sphere" boundary condition at the solid/fluid interface accurately represents the physics of g-mode oscillations in models with crystalline cores. Bildsten & Cutler (1995) found exactly the same approximation to be valid in their treatment of g-modes in the surface oceans of accreting neutron star models.

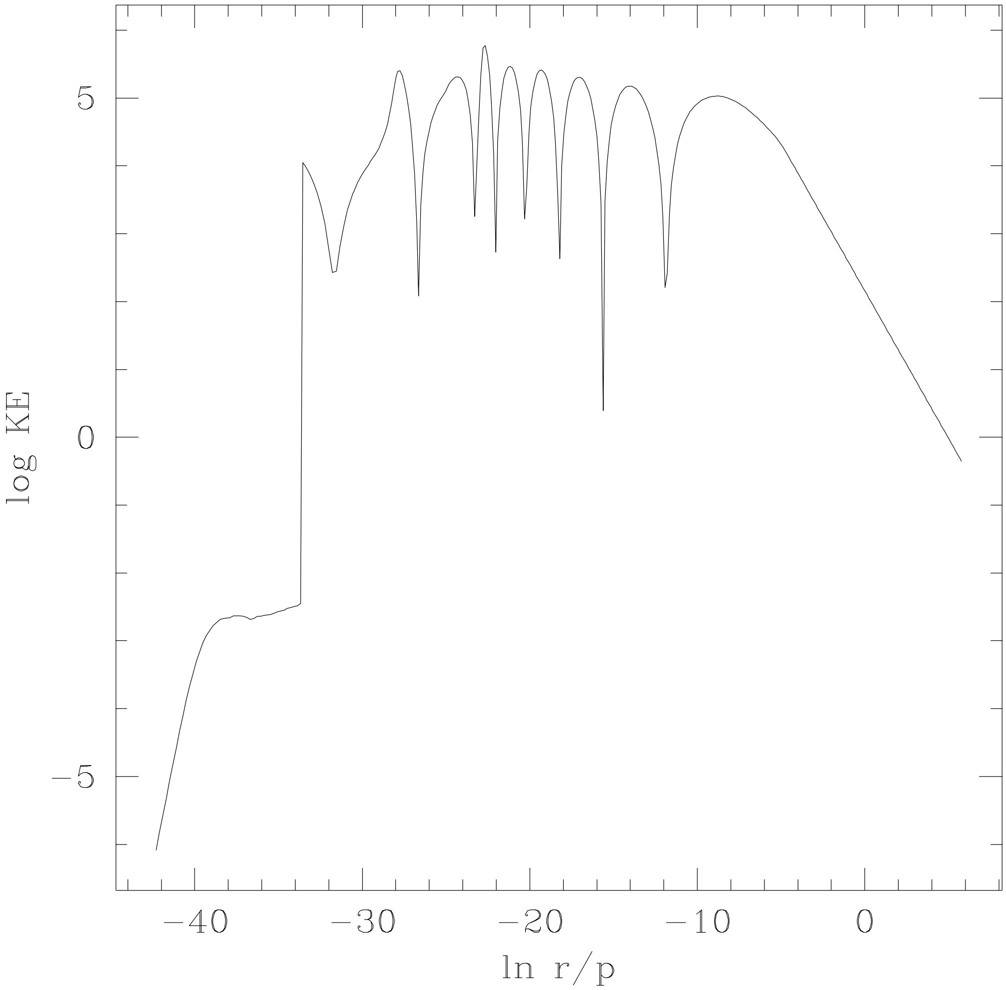

Fig. 3.6.— The log of the kinetic energy as a function of $\ln r/p$. The sharp drop of over 6 orders of magnitude in the kinetic energy at $\ln r/p \sim -34$ is due to the solid/crystal interface. The g-mode essentially does not penetrate into the crystallized region.

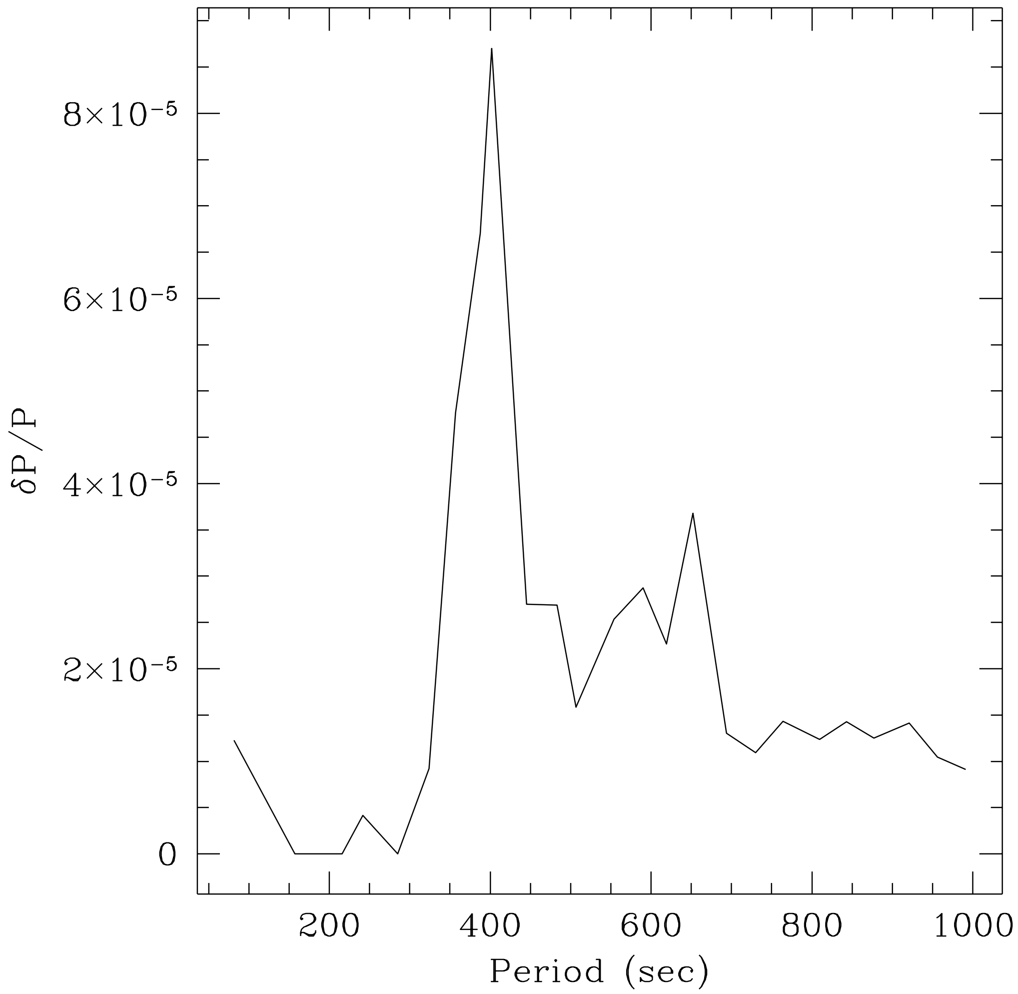

Fig. 3.7.— The fractional period difference $\delta P/P$ as a function of period. This difference is always less than one part in 10^4, which means that by using the "hard sphere" approximation, our errors in period are less than 0.1 sec for this range of periods, and in fact, are less than half of this. The same is true for the $\ell = 2$ modes.

Before proceeding to the detailed numerical calculations, we wish to convince the reader that crystallization will have a measurable effect on the periods. In Figure 3.8 we have plotted the kinetic energy per unit $x = \ln r/p$, so that the area underneath the curve represents the weight of each region's contribution to the total kinetic energy, as a function of x. The vertical dashed lines indicate different mass points in this model. For instance, if the model is 90% crystallized, then the kinetic energy to the left of the 90% line is eliminated from the mode. By visual inspection, this is of order 10% of the kinetic energy in the mode, so we might well expect that the period of this mode is affected at the 10% level. In fact, we will see in the next section that the periods can be shifted by even larger amounts.

Merely for purposes of contrast, we have included a plot similar to that in Figure 3.8, but *for a p-mode*; the mode displayed is an $\ell = 1$ mode. This shows that the kinetic energy is distributed differently in a p-mode, much deeper in the model. As we will see in the next section, this is a consequence of the "region of period formation" being deeper for p-modes than g-modes in white dwarf models.

5. The g-mode Periods as a Function of $M_{\rm xtal}/{\rm M}_\star$

5.1. Asymptotic Relations

The kinetic energy argument in section 4.2. tells us that we can expect the g-mode periods to change measurably as the crystallized mass-fraction increases from 0 to 90%. With this in mind, we re-examine the asymptotic formulae for

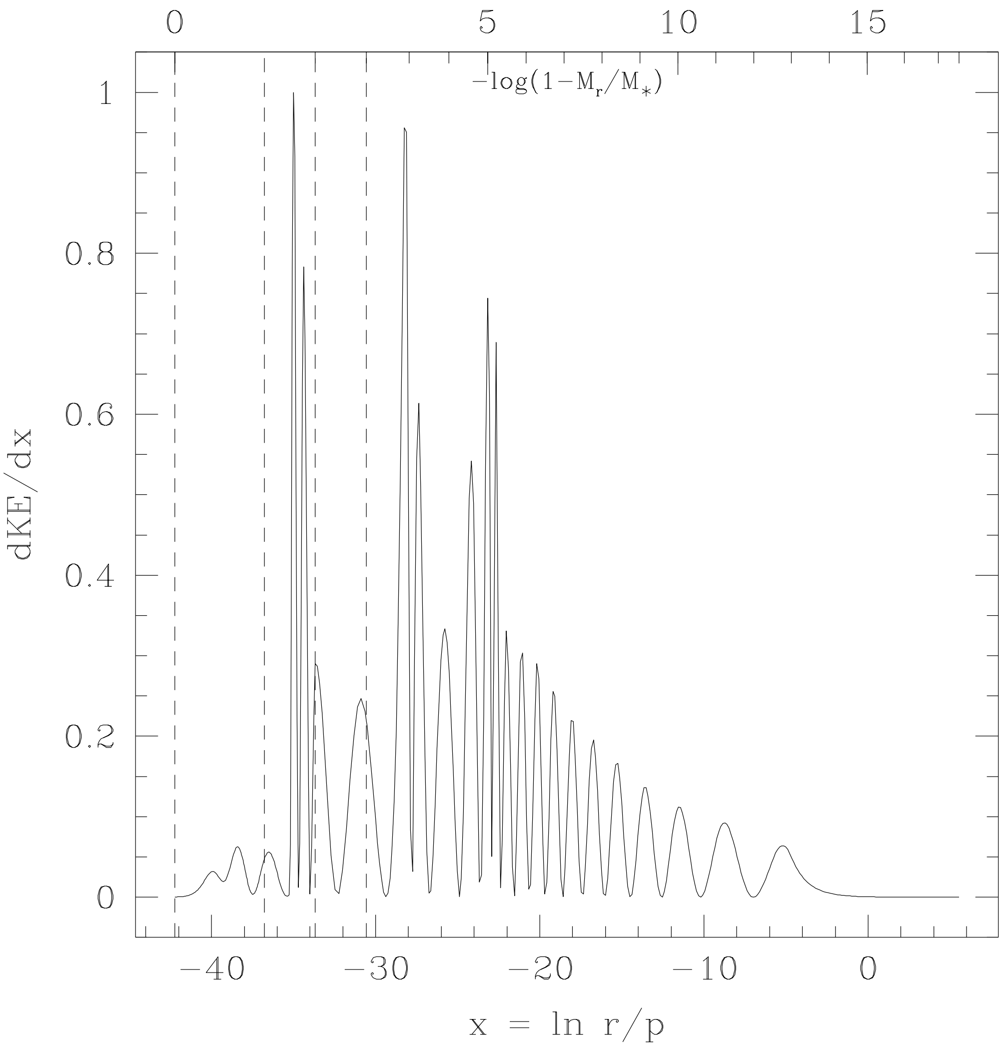

Fig. 3.8.— The kinetic energy per unit $x = \ln r/p$. The vertical dashed lines indicate the mass-fraction of the model interior to a given point. For instance, the dashed line at $x \sim -34$ defines the point in the model at which $M_{\rm r}/{\rm M}_\star = 0.90$.

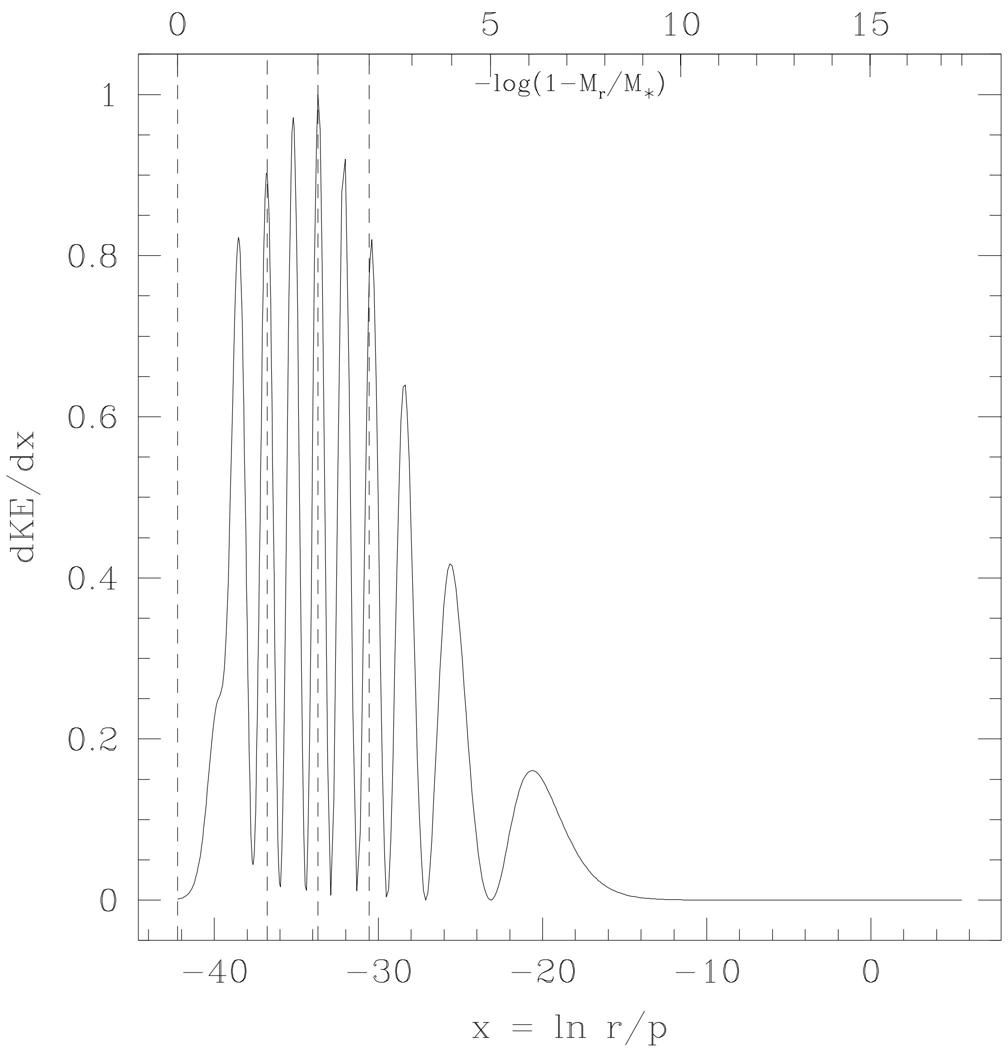

Fig. 3.9.— The kinetic energy per unit $x = \ln r/p$ of an $\ell = 1$ *p-mode*. The vertical dashed lines are present for easy reference to Figure 3.8, but we point out that the p-mode is able to propagate essentially unchanged into the crystallized regions of the model.

g-mode periods (e.g., Unno et al. 1989):

$$P_k \sim k\langle \Delta P \rangle,$$

$$\langle \Delta P \rangle = \frac{2\pi^2}{\sqrt{\ell(\ell+1)}} \left[\int_{r1}^{r2} N dr/r\right]^{-1}, \tag{3.31}$$

where we have written $\langle \Delta P \rangle$ for the mean period spacing between consecutive radial orders. Since the g-modes are excluded from the crystallized region, the inner turning point $r1$ is now a function of $M_{\rm xtal}/M_\star$. As we allow the model to crystallize while holding all other structural parameters constant, $r1$ moves outward, so the integral in equation 3.31 decreases, with the result that $\langle \Delta P \rangle$ and P_k both increase.

As a heuristic tool, we would like to plot the elusive "region of period formation," which would tell us visually the weight which the different regions of the star have in determining the period of a mode. This problem has been examined several times in the past, for example by Kawaler, Winget, & Hansen (1985), Schwank (1976), Goosens & Smeyers (1974), and originally by Epstein (1950). The aim in such analyses was not only to determine the broad regions of a given model which the modes sample, but also to note the *differences* in the way distinct modes sample a model.

To simplify matters, we examine this weight function in the asymptotic limit of high k and ℓ. For g-modes, we have to be content to determine a "region of frequency formation." We find from equation 3.21 that the relative contribution to the total frequency per unit radius is

$$\frac{d\sigma}{dr} \approx \frac{N}{r},$$

which depends only on N and r. In order to expand the radial axis and make the resulting functions easier to examine, we choose $x = \ln r/p$ as our radial coordinate. Then this becomes

$$\frac{d\sigma}{dx} \approx \frac{N}{1+V}, \tag{3.32}$$

where $V \equiv \Gamma_1 gr/c_s^2$. We emphasize that the appearance of the sound speed c_s^2 in the variable V is purely a result of the above radial coordinate change, and does not reflect a dependence of g-mode frequencies on c_s.

In Figure 3.10, we plot $d\sigma/dx$ versus x for a 1.1 $\mathrm{M}_\odot$ model with $\log M_{\mathrm{He}}/\mathrm{M}_\star = -3$ and $\log M_{\mathrm{H}}/\mathrm{M}_\star = -5$. The three spikes in $d\sigma/dx$ correspond to the composition transition zones O/C, C/He, and He/H. From inspection of this figure, we would expect the C/He transition zone to have the least effect on the g-mode periods, whereas the O/C transition zone in the core and the He/H transition zone in the envelope should both have a large effect. Numerically, Bradley (1993b) has found that the average period spacing and mode trapping effects to be most sensitive to the hydrogen layer mass, and least sensitive to the thickness of the helium layer.

The above discussion suggests that one way to idealize the composition transition zones while still retaining their mode trapping properties is to treat the corresponding bumps in the Brunt-Väisälä frequency as delta functions, i.e., something which is infinitesimally thin yet still has a finite area underneath it. In this limit, the Brunt-Väisälä frequency itself would be discontinuous across the transition zone, having different values on each side. This was treated numerically by Winget, Van Horn, & Hansen (1981) through the use of "jump conditions" (Gabriel & Scuflaire 1979).

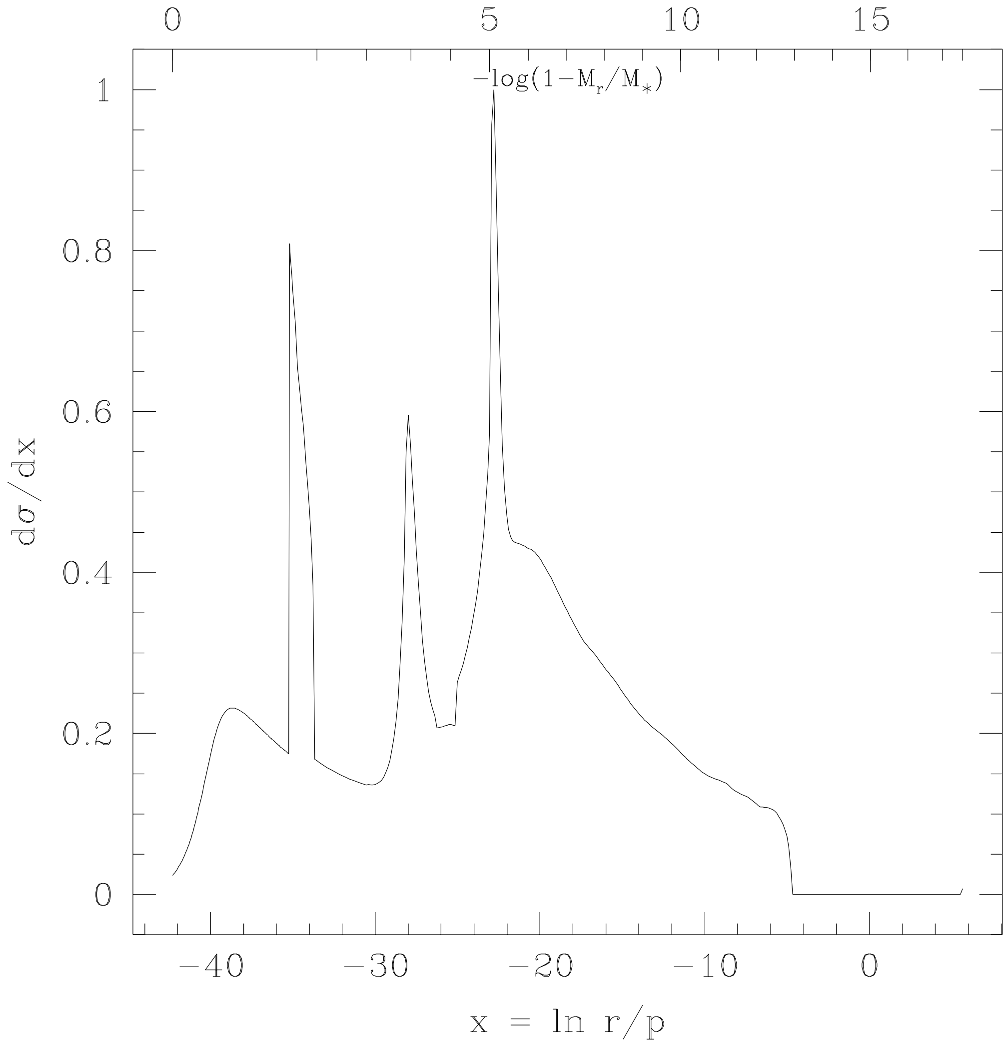

Fig. 3.10.— The frequency (period) formation region for g-modes in a 1.1 $M_\odot$ model. The three spikes are all composition transition zone features, which from left to right are due to the O/C, C/He, and He/H transition zones.

It is worth commenting on the similarities between the distribution of kinetic energy in Figure 3.8 and the shape of the g-mode period formation region in Figure 3.10. The kinetic energy plot is for a numerically determined mode, whereas the period formation region is in the high k limit. The value of $N/(1+V)$ in Figure 3.10 should correspond to to the wavelength of oscillations as a function of x in Figure 3.8. This is in fact the case, since we see that peaks in Figure 3.10 correspond to rapid spatial oscillations in the kinetic energy density. Similarly, the small value of $N/(1+V)$ at $x \sim 5$–10 results in a longer spatial wavelength in the oscillations of the kinetic energy density at this value of x.

We also note that the overall envelope of the kinetic energy is similar in shape to Figure 3.10. The kinetic energy dE in a shell dr is given by

$$\begin{aligned} dE &\approx \rho r^2 dr \left(\xi_r^2 + \ell(\ell+1)\xi_h^2\right) \\ &\approx \rho r^2 dr \xi_h^2, \end{aligned}$$

where we have used the fact that $\xi_h \gg \xi_r$ for g-modes. If we now substitute for ξ_h the asymptotic value for it taken from Unno et al. (1989), then we find

$$\begin{aligned} \frac{dE}{dr} &\approx \rho r^2 \xi_h^2 \\ &\approx \rho r^2 \left[\frac{N}{\rho^{1/2} r^2} w(r)\right]^2 \\ &\approx \rho r^2 \left[\frac{N}{\rho^{1/2} r^2} \frac{1}{\sqrt{k_r}} \cos\left(\int_r^{r2} k_r dr'\right)\right]^2 \\ &\approx \frac{N^2}{r^2 k_r} \cdot \frac{1}{2} \\ &\approx \frac{N^2}{r^2 N/r} \\ &\approx \frac{N}{r}, \end{aligned} \tag{3.33}$$

where $w(r)$ is an intermediate function defined in the asymptotic solution, we have replaced the rapidly oscillating $\cos^2$ by its average value of 1/2, and we have discarded all factors which do not have a radial dependence. Thus, we see that in the asymptotic limit the kinetic energy samples the model in the same way as does the period for g-modes.

We feel compelled to include a similar figure for a 0.6 $M_\odot$ model, since the peak in the observed white dwarf mass function is in the neighborhood of 0.6 $M_\odot$ (Weidemann & Koester 1983; Weidemann & Yuan 1989; Bergeron et al. 1995; Lamontagne et al. 1997). In Figure 3.11, we show the region of period (frequency) formation for a 0.6 $M_\odot$ model which otherwise has the same set of parameters as the more massive model. Here we see that the C/He transition zone should have a less dramatic effect on the average period spacing. In addition, the g-modes sample the core less in the more massive model. This makes sense since the higher mass model is denser in its core, so the Fermi energy of its electrons is higher. At the same temperature, this makes the pressure/density relationship closer to adiabatic. Since the Brunt-Väisälä frequency is the difference between the actual density gradient in the model and the adiabatic density gradient, the Brunt-Väisälä frequency is smaller in the core of the higher mass model, which results in the g-modes being forced farther out into the envelope.

For completeness, we wish to consider the period formation region for p-modes. From equation 3.20, we have

$$\frac{dP}{dr} \approx \frac{1}{c_s},$$

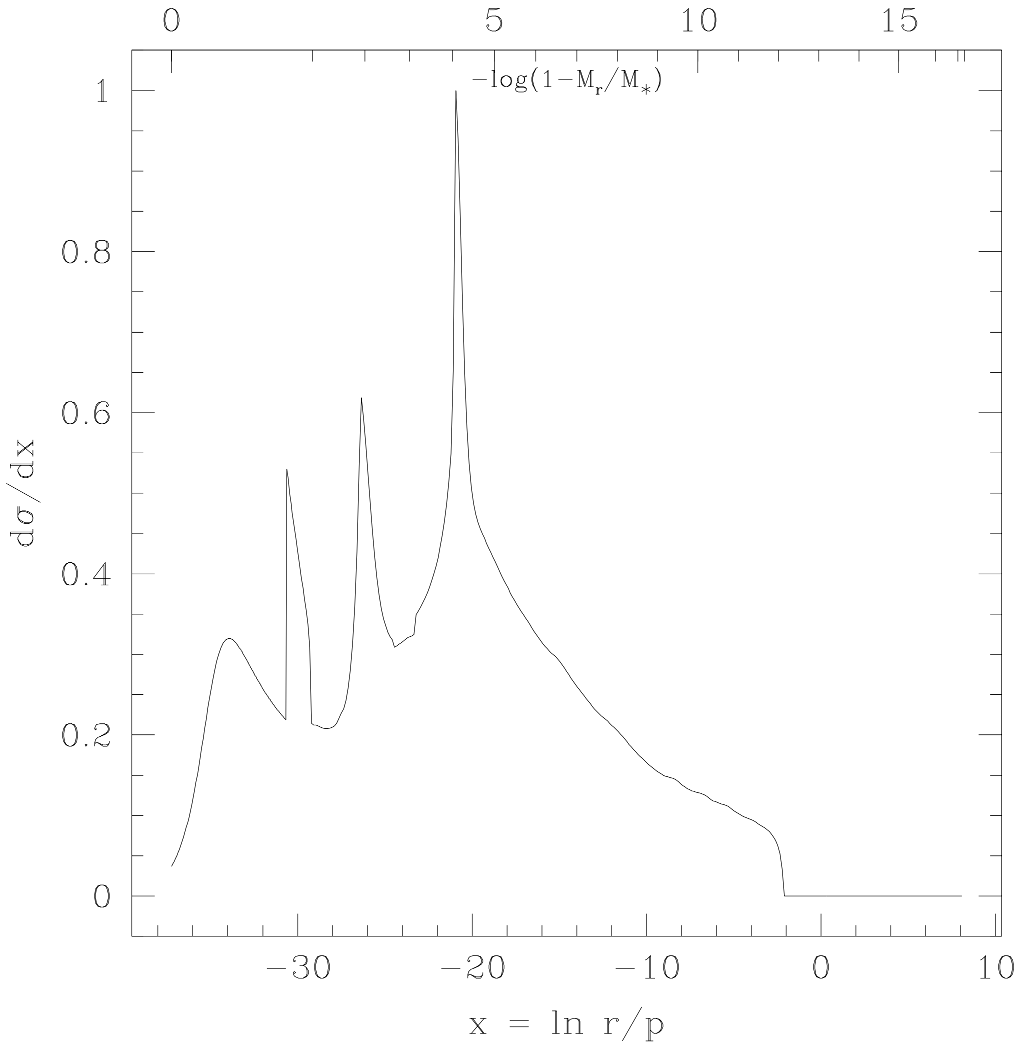

Fig. 3.11.— The period (frequency) formation region for g-modes in a 0.6 $M_\odot$ model.

so again using $x = \ln r/p$ as the radial variable, we have

$$\frac{dP}{dx} \approx \frac{r}{c_s(1+V)}, \tag{3.34}$$

where P is the mode period, c_s is the sound speed, and the other variables have the same meaning as in equation 3.32. In Figure 3.12 we plot dP/dx for p-modes, where the model used is identical to the 1.1 $M_\odot$ model used in Figure 3.10. The period formation region for p-modes in this model is weighted more toward the core than it is for the g-modes. This confirms our picture of g-modes in white dwarfs as "envelope" modes and p-modes as "core" modes. In addition, the energy density in the asymptotic limit has exactly the same weighting as does the period formation region, i.e., after an asymptotic analysis similar to the g-mode case, we find

$$\frac{dE}{dr} \approx \frac{1}{c_s}. \tag{3.35}$$

We see that the envelope of the kinetic energy in Figure 3.9 is quite similar in shape to Figure 3.12, reinforcing our conclusion.

5.2. Numerical Results

We now wish to make a comparison between the functional form of the period spacing implied by equation 3.31 and that derived from direct numerical calculations. To do this, we normalize $\langle \Delta P \rangle$ to the average period spacing in the uncrystallized case, denoted by $\langle \Delta P \rangle_0$. Such a comparison is shown in Figure 3.13, where the solid line gives the analytic relation and the filled circles are the result of a numerical pulsational analysis of $\ell = 2$ periods between 500 and 1000 sec. We have made the model, a 1.1 $M_\odot$ C/O core model, artificially

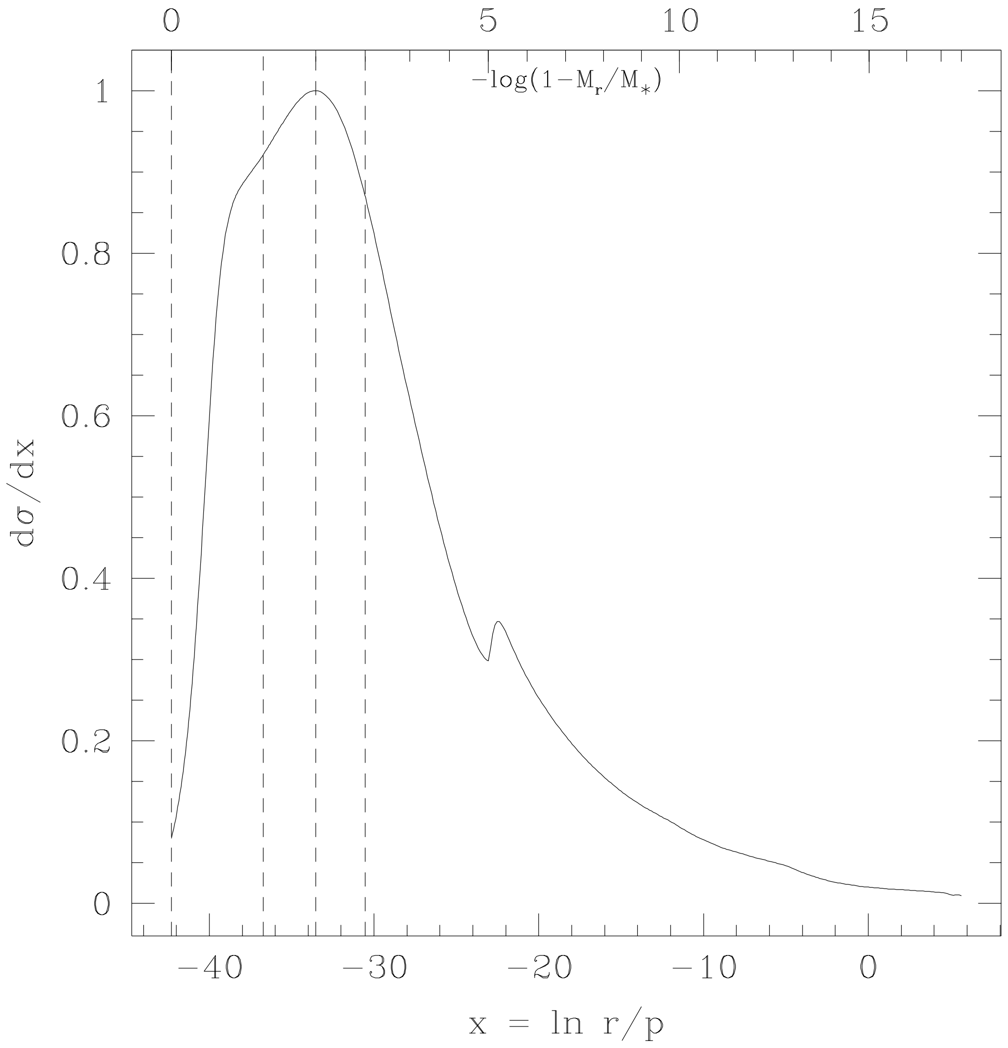

Fig. 3.12.— The period formation region for p-modes in a 1.1 $M_\odot$ model identical to that used in Figure 3.10. Note that the period formation region for p-modes is much deeper than the region for g-modes shown in Figure 3.10.

smooth by using the Schwarzschild criterion for the Brunt-Väisälä frequency, which essentially removes the bumps from the Brunt-Väisälä frequency and therefore minimizes mode trapping. The agreement between the two methods is extremely good.

We now examine the more realistic case, where we use the modified Ledoux criterion for the Brunt-Väisälä frequency (bumps and all). This plot is shown in Figure 3.14. Although the overall shape of the plot has changed somewhat, the agreement between the asymptotic and numerical results is still quite good. The observed "kink" for $0.75 \leq M_{\rm xtal}/{\rm M}_{\star} \leq 0.90$ is caused by the oxygen mass-fraction decreasing from 0.80 to 0.00 in this range. If we examine Figure 3.10 for the period formation region and we imagine moving the crystallization region to the right, we see that as we encounter the O/C transition zone, the area under the curve doubles, so we would expect the slope of the curve in Figure 3.14 to double as well, which is what we find.

An equivalent statement to the period spacing increasing with $M_{\rm xtal}/{\rm M}_{\star}$ is that the modes themselves are getting farther apart in period, so their periods must also be increasing. To illustrate this, we show how a spectrum of mode periods evolves continuously with $M_{\rm xtal}/{\rm M}_{\star}$. Since mode identification between different models is not a simple matter, we have calculated the spectrum of modes on a fine enough mesh in $M_{\rm xtal}/{\rm M}_{\star}$ so that the period changes are small compared to the distances between the periods themselves. We then identify a given mode at one mesh point with the nearest mode in period of the neighboring mesh point.

The result of this calculation for $\ell = 2$ periods is shown in Figure 3.16, where the model considered is a 1.1 ${\rm M}_{\odot}$ with $T_{\rm eff} = 11,800$ K, $M_{\rm He}/{\rm M}_{\star} = -3$,

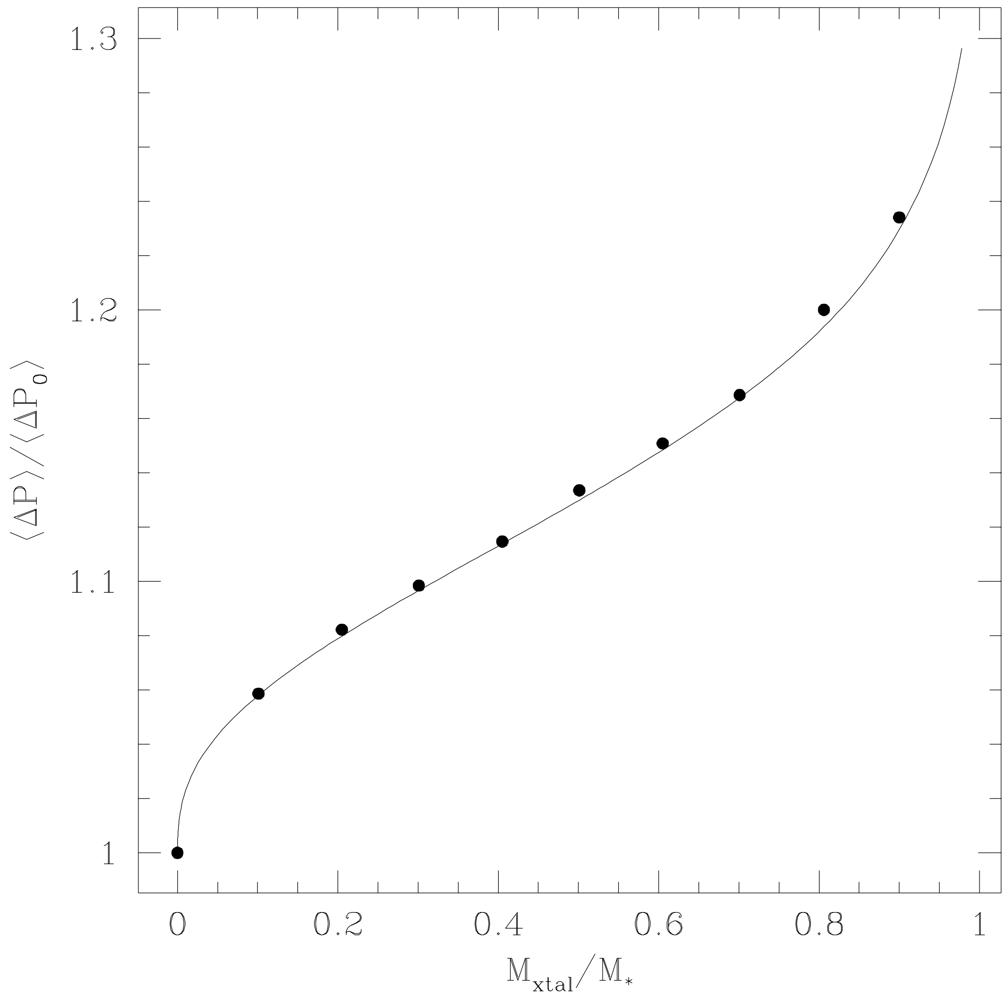

Fig. 3.13.— A comparison of analytical (solid line) and numerical (filled circles) period spacings, as a function of $M_{\rm xtal}/\mathrm{M}_\star$, where each has been normalized to the period spacing in the uncrystallized case. In order to minimize mode trapping effects, the Schwarzschild criterion has been used to compute the Brunt-Väisälä frequency.

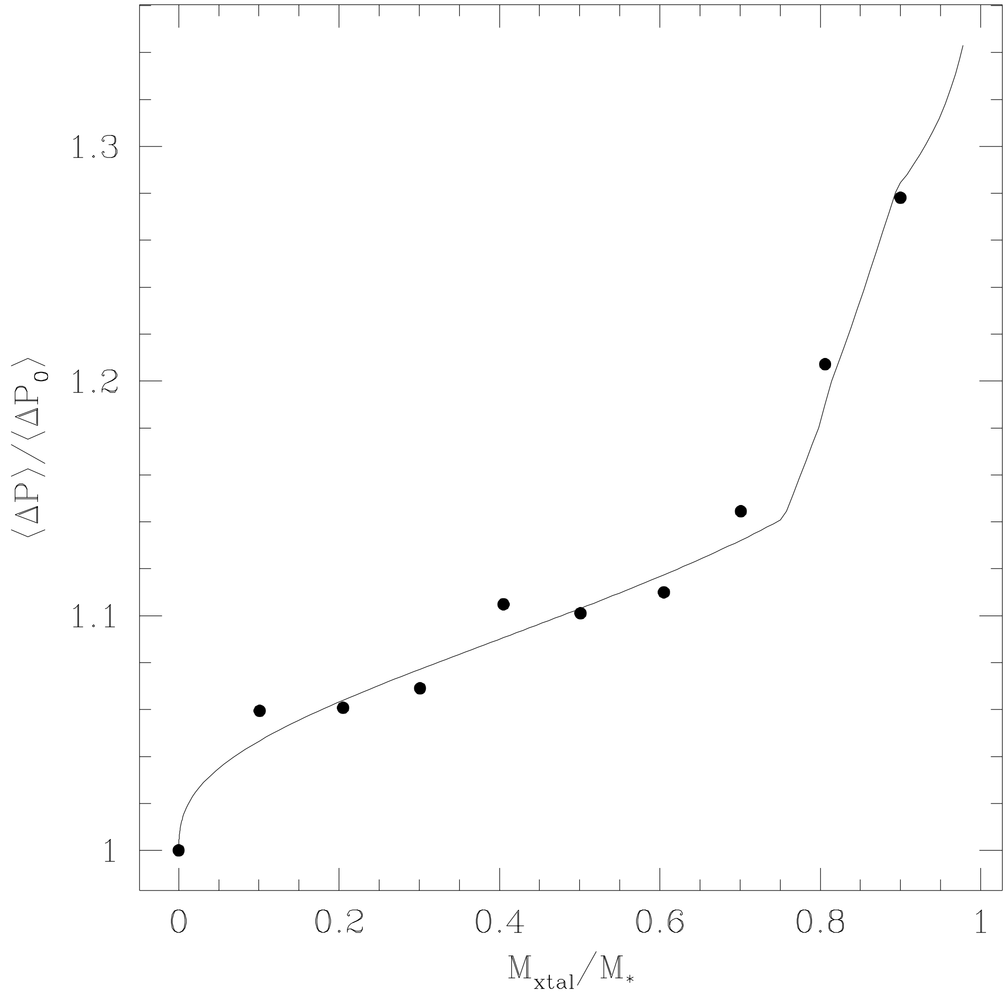

Fig. 3.14.— The same as Figure 3.13, except that the modified Ledoux prescription has been used to calculate the Brunt-Väisälä frequency. The "kink" for $0.75 \leq M_{\rm xtal}/{\rm M}_\star \leq 0.90$ is due to the changing C/O profile in the core.

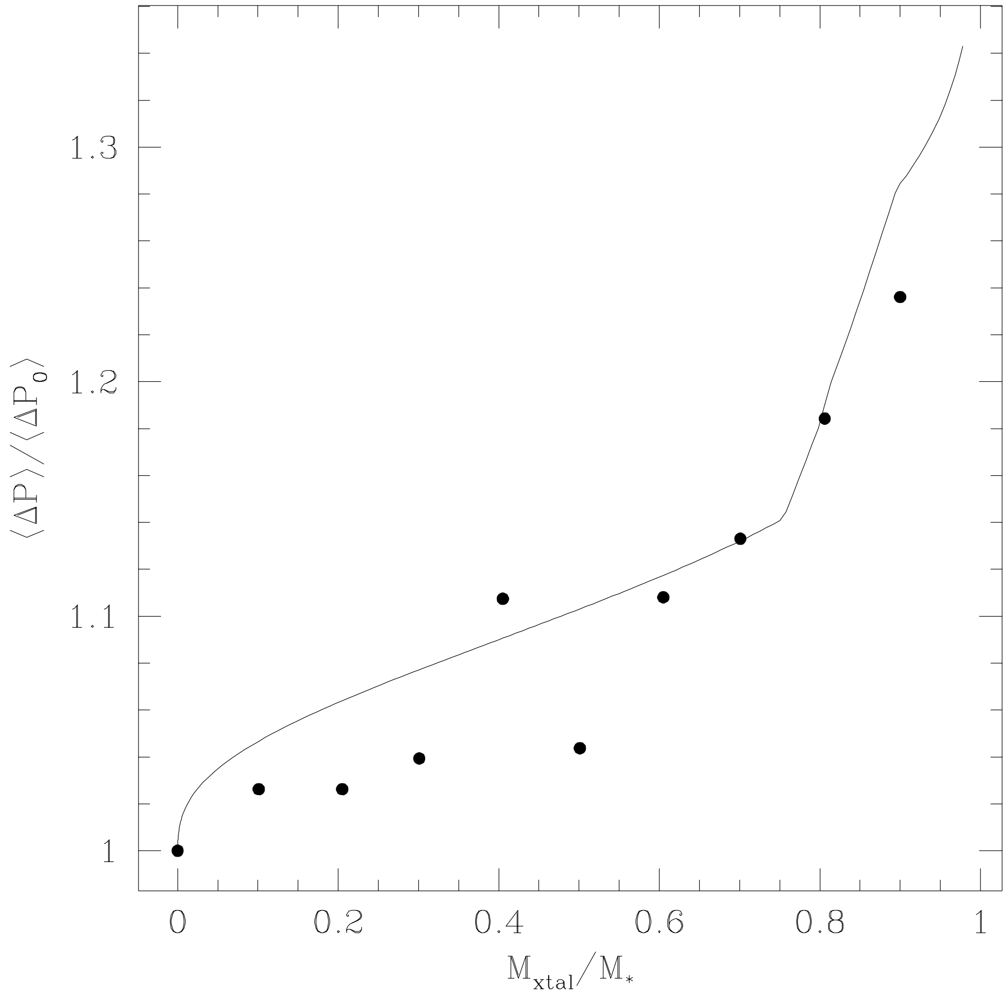

Fig. 3.15.— The same as Figure 3.14, except that periods between 500 and 700 sec have been used to define the average period spacing from the pulsation calculations; we have picked this range of periods to mimic that observed in BPM 37093. Here we see that mode trapping effects produce significant deviations from the asymptotic relation, and make it difficult to to determine the asymptotic value of $\langle \Delta P \rangle$.

and $M_{\rm H}/{\rm M}_\star = -5$. We have used the "hard-sphere" approximation for the solid/liquid boundary and the full Ledoux prescription for the Brunt-Väisälä frequency in calculating these periods; we have varied the parameter $M_{\rm xtal}/{\rm M}_\star$ from 0.00 to 0.99 in increments of 0.01. We note that the periods either appear to be increasing or are relatively constant. In fact, even in regions in which the period of a given mode is changing slowly, its period is still slightly increasing.

Figure 3.16 represents the most detailed calculation to date showing how g-mode periods in white dwarf models evolve as a single parameter is slowly varied. As such, it exhibits many interesting features. First, for a given degree of crystallization, some modes are much more sensitive to changes in $M_{\rm xtal}/{\rm M}_\star$ than are other modes. This is because none of these modes has a period large enough to be in the asymptotic limit, so they each sample the model differently. For instance, those modes which preferentially sample the deep interior of the model will be more strongly affected by a change in the amount of crystallization.

A second, related feature concerns how a pair of modes appears to approach and then move away from each other as the degree of crystallization is increased. This is reminiscent of the "avoided crossing" behavior found by Aizenman, Smeyers, & Weigert (1977). They found that two modes which approached each other in frequency were prevented from having the same frequency, and were forced to "veer away" from each other. In the process of this near miss, however, the modes exchanged their characteristic properties. The two lowest period modes pictured in Figure 3.16 have what appears to be an avoided crossing at $M_{\rm xtal}/{\rm M}_\star = 0.65$. To the left of this point, the lower period mode has more of its kinetic energy deep in the model near the

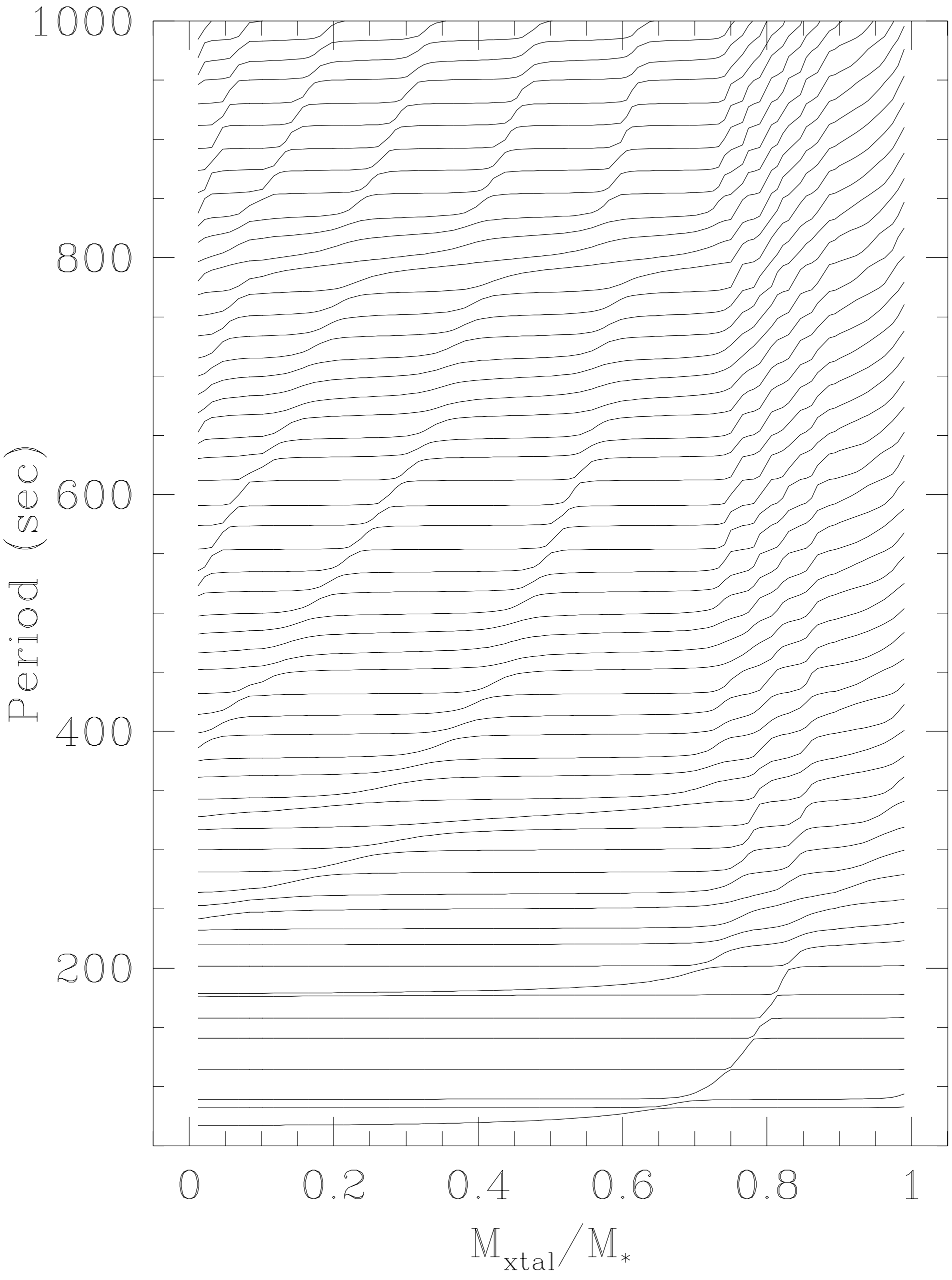

Fig. 3.16.— The evolution of $\ell = 2$ g-mode periods as a function of the crystallized mass-fraction. We see that in any region, the periods are either increasing or relatively constant.

solid/fluid interface, while to the right of this point it is the higher period mode which has its kinetic energy deeper. Thus, the modes *do* switch character at the "avoided crossing" point. This suggests that we may be seeing the same behavior described by Aizenman, Smeyers, & Weigert (1977), but in a different context.

Our general result that the g-mode periods increase due to the presence of crystallization is not what was found by Hansen & Van Horn (1979), who claimed that the g-mode periods became shorter when the finite shear of the solid core was included. We believe that the resolution of this disagreement lies in a re-interpretation of their calculated periods, not in the periods themselves. Hansen & Van Horn (1979) calculated the periods of $k = 1$ and 2 modes for $\ell = 1$, 2, and 3, in both the fluid case and in the case of a 99.9% crystallized core. They found that in the crystallized case, the $k = 1$ periods had decreased by approximately a factor of two compared to the fluid case; for example, the $\ell = 1$ period decreased from 193.8 sec to 99.8 sec. Our interpretation is that the 99.8 sec mode is actually a new mode, which would not exist if the core were not crystallized. Thus, the main effect of introducing a solid core is, in our view, to add an extra mode with a period below that of the previous $k = 1$ mode. To support this view we compare their $k = 1$ periods in the fluid case with their $k = 2$ periods in the solid case. For $\ell = 1$, 2, and 3, we find that their periods now *increase* from 193.8 to 193.9 sec, from 111.9 to 112.0 sec, and from 79.1 to 79.2 sec, respectively. While these increases are small, they are consistent with what one might expect from a $T_{\rm eff} \sim 10{,}000$ K Fe core white dwarf model which is strongly degenerate in its interior. In addition, the periods in the uncrystallized and the crystallized state are close enough to strengthen our conviction that this is actually the “correct” mode identification.

Using our “global” code, we are numerically unable to treat models which are more than 97% crystallized. For 97% crystallized models, we do find evidence for low-period “interfacial” modes which do not exist in the uncrystallized case; interfacial modes such as these were found in neutron star models by McDermott, Van Horn, & Hansen (1988). These modes could be the new modes found by Hansen & Van Horn (1979). We caution, however, that we do not understand the properties of these modes, i.e., how they change period as the degree of crystallization changes and whether or not the standard definition of radial overtone number is meaningful. We are therefore unable to extrapolate these results to the case of 99.9% crystallization which Hansen & Van Horn treated.

6. $\langle \Delta P \rangle$ as a Function of the Model Parameters

In uncrystallized models, the period spacing is a function of many things, including the total stellar mass, the effective temperature, and the hydrogen layer mass. This is still true in the crystallized case, and we examine the effects which each has on $\langle \Delta P \rangle$. The fiducial model against which we compare our calculations is a model with $\mathrm{M}_\star = 1.1\mathrm{M}_\odot$, $T_{\mathrm{eff}} = 11,800$, $M_{\mathrm{H}}/M_\star = 10^{-5}$, and $M_{\mathrm{He}}/M_\star = 10^{-3}$. Unless otherwise stated, all periods are calculated using the modified Ledoux prescription for the Brunt-Väisälä frequency.

6.1. The Hydrogen Layer Mass, M_{H}

For 0.6 $M_\odot$ models, nuclear burning considerations force $M_{\mathrm{H}}/M_\star$ to be smaller than a few times 10^{-4} (Iben & Tutukov 1984; Iben & Macdonald 1985). For models near 1.1 $M_\odot$, this translates into $M_{\rm H}/M_\star \leq 10^{-5}$ due to the higher gravities and pressures. We therefore examine models with $M_{\rm H}/M_\star$ between 10^{-10} and 10^{-5}.

In Figure 3.17, we plot $\langle \Delta P \rangle$ versus $\log M_{\rm H}/M_\star$ for different degrees of crystallization, as shown in the legend. For this model, we have used a C/O core and set $M_{\rm He}/M_\star = 10^{-3}$ and $T_{\rm eff} = 11,800$ K, and we have calculated the Brunt-Väisälä frequency using the Schwarzschild criterion, so that we may minimize mode trapping effects as much as possible. We see that the effect of increasing crystallization is to increase $\langle \Delta P \rangle$ at all compositions. Similarly, the effect of decreasing $\log M_{\rm H}/M_\star$ is also to increase $\langle \Delta P \rangle$, for all degrees of crystallization. Thus, a change in one can mimic a change in the other. Figure 3.18 shows the more physical case where we have used the Ledoux prescription for calculating the Brunt-Väisälä frequency in this model. The same trends are still evident, but the period spacing itself has decreased by 3–4 sec for all the models. This difference is due to the contribution of the composition transition zones.

The horizontal dashed lines in Figures 3.17 and 3.18 represent the possible range of the asymptotic period spacing for BPM 37093. This range is based on the observed value for $\langle \Delta P \rangle$ of ~ 17.3 sec from a preliminary analysis of the WET data, where we have assumed "errors" of $\pm 5\%$ in translating this to an asymptotic period spacing, as suggested by the deviations from the asymptotic line in Figure 3.15. For this analysis, we have assumed the observed modes are all $\ell = 2$ modes, since $\langle \Delta P \rangle \sim 17$ sec is too short to be produced by consecutive $\ell = 1$ modes in models with $\mathrm{M}_\star \sim 1.1\mathrm{M}_\odot$. In addition, we assumed the modes were all $m = 0$ since only in this way would we have enough information to

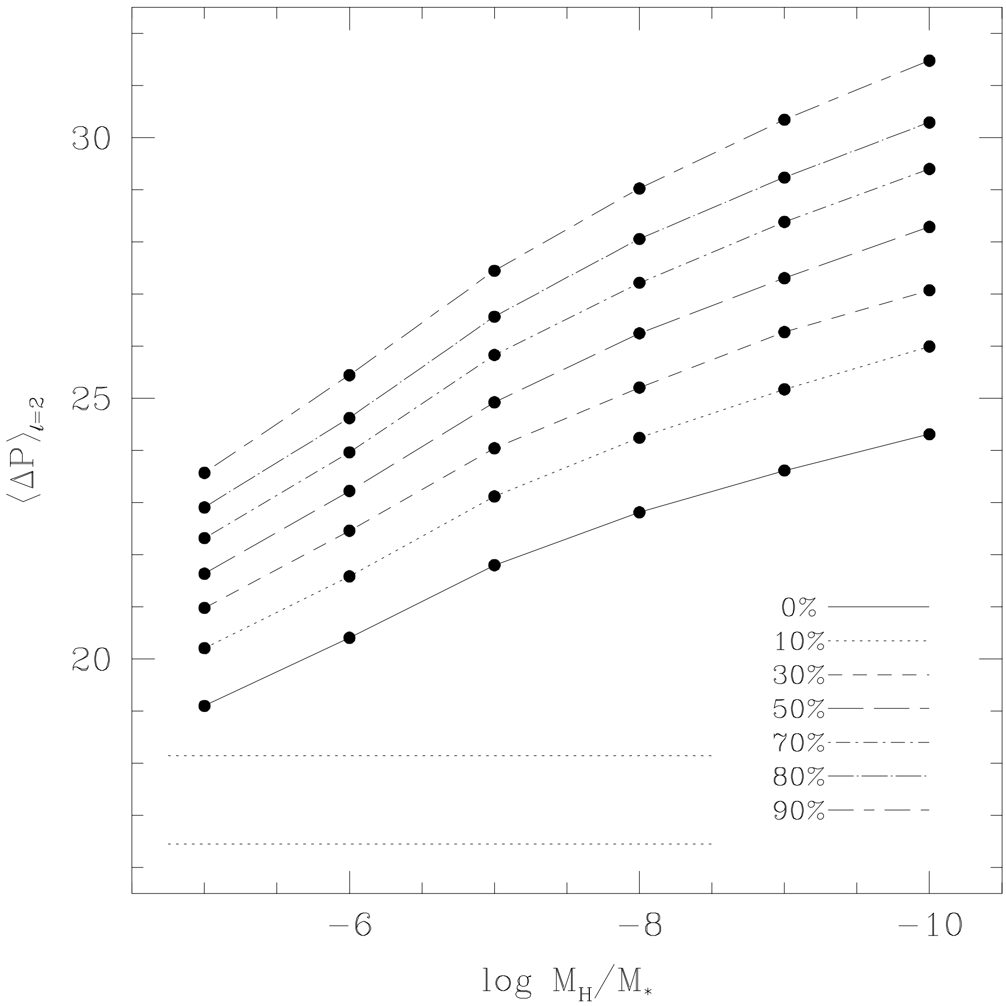

Fig. 3.17.— $\langle \Delta P \rangle$ as a function of $\log M_{\rm H}/M_\star$ for differing degrees of crystallization with N^2 calculated according to the Schwarzschild criterion.

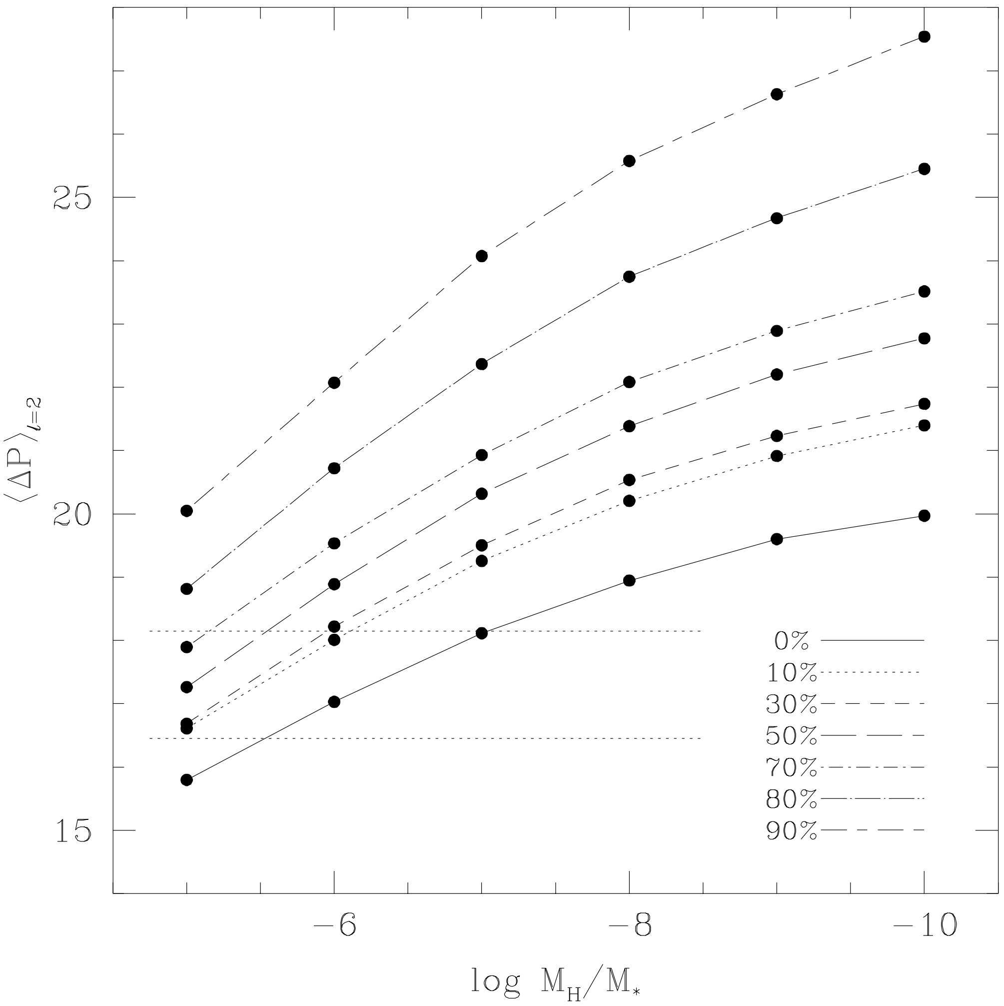

Fig. 3.18.— The same as Figure 3.17, except with N^2 calculated with the Ledoux prescription.

attempt a fit.

From Figure 3.18, we find the following constraints on our parameter space: $-7 \leq \log M_{\rm H}/M_\star \leq -5$ and $0.00 \leq M_{\rm xtal}/M_\star \leq 0.70$. This is a fairly large range for each parameter, but they are now no longer independent. If we know one of them, then that can reduce the allowed range for the other. For instance, if the model is 50% crystallized, then we must have $-6 < \log M_{\rm H}/M_\star < -5$. From Figure 3.17, we see that there is no choice of parameters for which the period spacing matches the data. This is not only evidence that the Schwarzschild criterion is not an appropriate description, but that the composition transition zones *do* have a significant effect on the average period spacing.

6.2. The Total Stellar Mass, $\mathrm{M}_\star$

We now consider models which differ only in mass from our fiducial model; all the other parameters are held fixed. In Figure 3.19 we plot the average period spacing for a set of $\mathrm{M}_\star = 1.15\ \mathrm{M}_\odot$ models as a function of $M_{\rm H}$, where we continue to use the more physical Ledoux prescription for the the Brunt-Väisälä frequency. Since the more massive models are smaller in radius, they have a higher average density, and therefore smaller periods and period spacings. For the less massive, $1.05\ \mathrm{M}_\odot$ models in Figure 3.20, we find the opposite is the case; these models are larger in radius and therefore have larger period spacings.

6.3. The Effective Temperature, $T_{\rm eff}$

In Figure 3.21 we show how the mean period spacing for $\ell = 2$ modes varies as a function of the effective temperature for our fiducial models. The horizontal

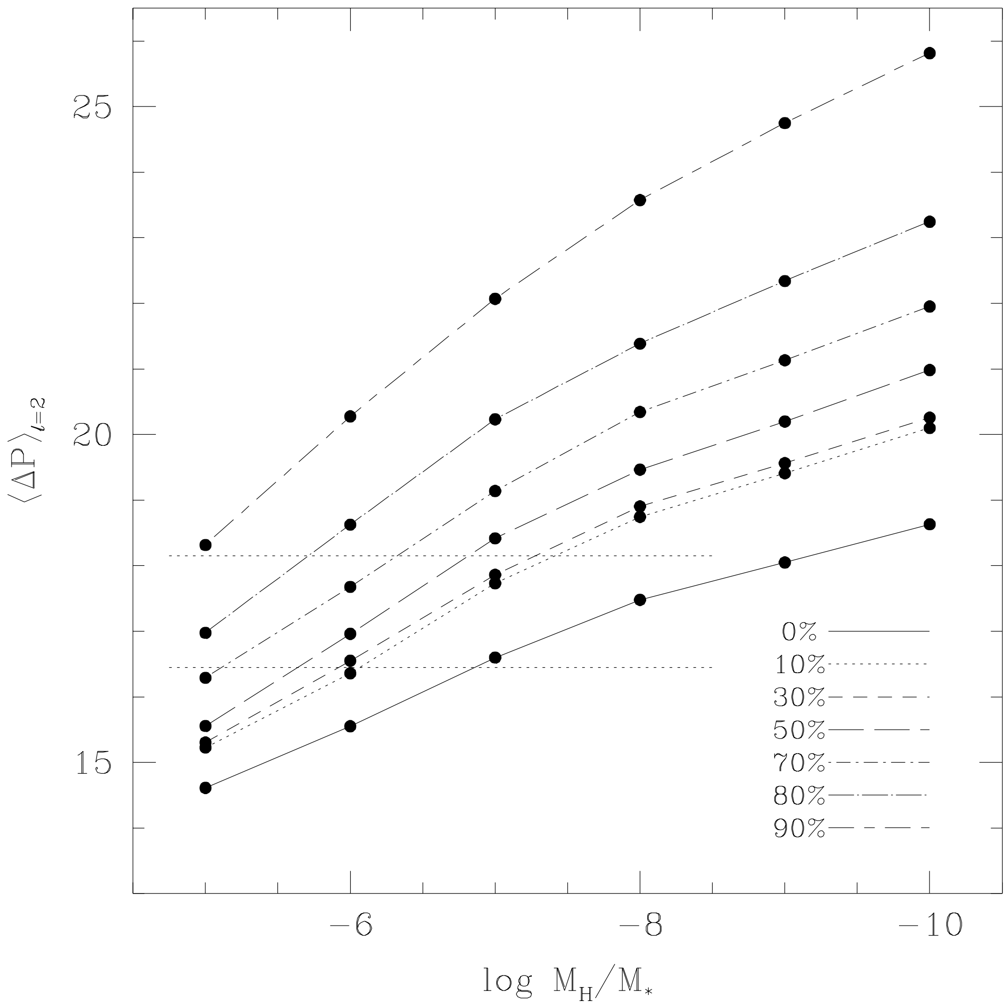

Fig. 3.19.— The same as Figure 3.18, except for 1.15 $M_\odot$ models.

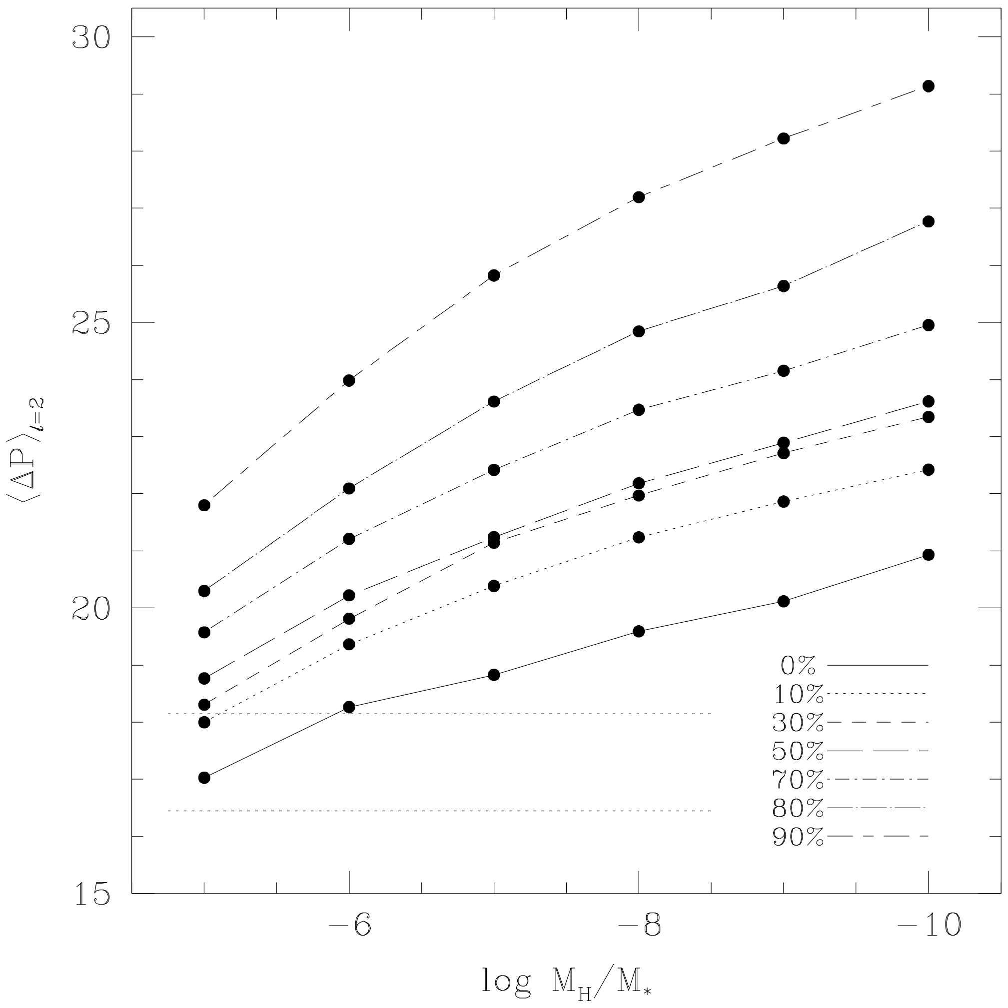

Fig. 3.20.— The same as Figure 3.18, except for 1.05 $M_\odot$ models.

dotted lines again span the range of the period spacing as determined from the data for BPM 37093. We see that as the models cool, the period spacing increases. This occurs because the models become more degenerate as they cool; in a completely degenerate configuration, the Brunt-Väisälä frequency is identically zero, except in a composition transition zone.

6.4. Scaling Relations

The results of the previous sections may be used to obtain simple (and simplistic) scaling relations for $\langle \Delta P \rangle$. If we look at small variations of these parameters about our fiducial model with 50% crystallization, then we find the following:

$$\langle \Delta P \rangle \propto X^{0.52} M_{\star}^{-2.1} T_{\rm eff}^{-0.69}, \tag{3.36}$$

where $X \equiv -\log M_{\rm H}/{\rm M}_{\star}$. In order to see the effect of observational uncertainties in these quantities, we recast equation 3.36 in differential form:

$$\frac{\delta \langle \Delta P \rangle}{\langle \Delta P \rangle} \propto 0.52 \frac{\delta X}{X} - 2.1 \frac{\delta {\rm M}_{\star}}{{\rm M}_{\star}} - 0.69 \frac{\delta T_{\rm eff}}{T_{\rm eff}}. \tag{3.37}$$

From fits of spectra of BPM 37093, Bergeron et al. (1995) find approximately $T_{\rm eff} = 11,740 \pm 200$ K, and ${\rm M}_{\star} = 1.09 \pm 0.05 {\rm M}_{\odot}$. From this we see that errors in the mass determination produce over 8 times the effect of errors in the temperature determination. Thus, ${\rm M}_{\star}$ is the most important input parameter which the observations can provide. The quantity X, the log of the hydrogen layer mass, is not an observable quantity in the standard sense. It can only be determined from an asterseismological analysis of a particular star, which leads us to the topic of the next section.

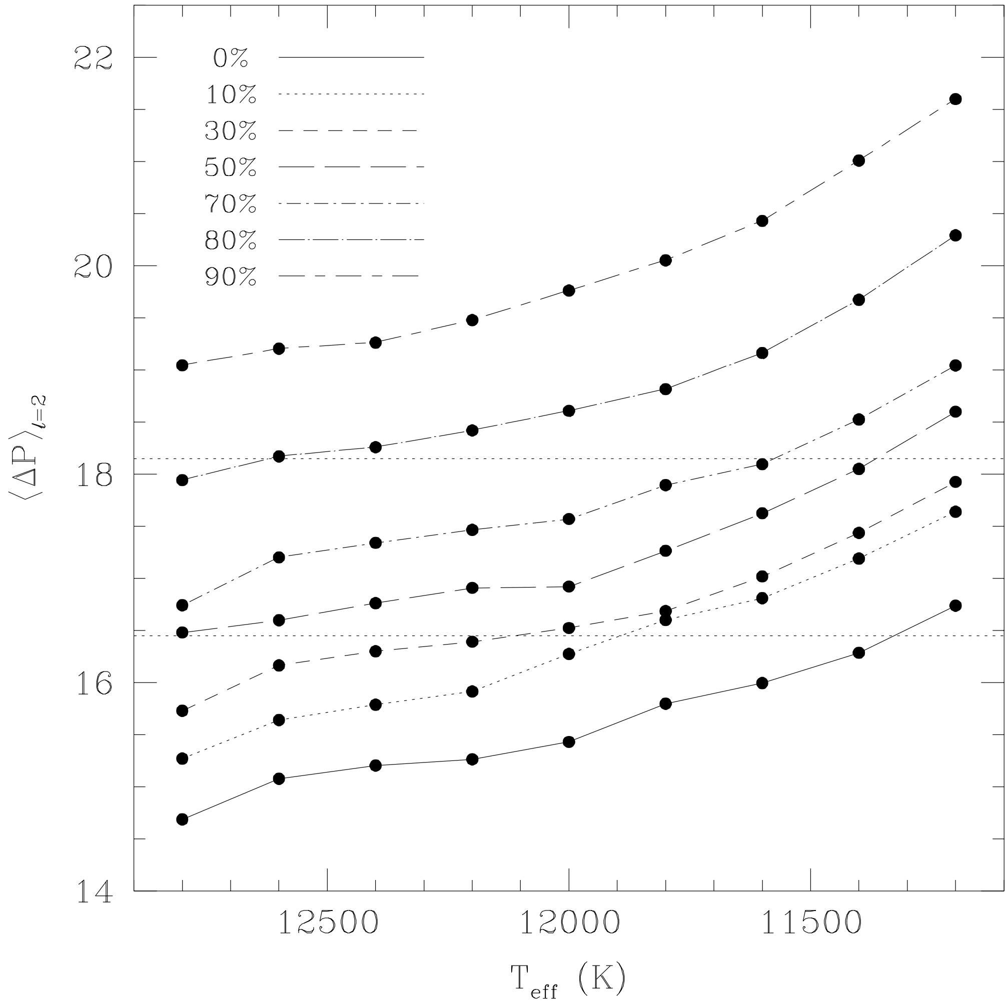

Fig. 3.21.— The average period spacing as a function of $T_{\rm eff}$ for different degrees of crystallization, as shown in the legend. The models all have $M_\star = 1.1 M_\odot$, $M_{\rm He}/M_\star = 10^{-3}$, and $M_{\rm H}/M_\star = 10^{-5}$.

7. Mode Trapping

7.1. Physical Description

If we examine Figure 3.10 or Figure 3.11, we see that the composition transition zones contribute a disproportionate weight to the frequency. In fact, eliminating the effect of these zones by using the Schwarzschild criterion for the Brunt-Väisälä frequency results in periods and period spacings which are larger by 14% and 23% for Figures 3.10 and 3.11, respectively. We saw that this had the effect of making the period spacings of the 1.1 $M_\odot$ model too large to agree with the preliminary value of $\langle \Delta P \rangle$ determined for BPM 37093. Apart from affecting just the mean period spacing, these transition zones introduce irregularities into individual period spacings, an effect which has come to be known as "mode trapping."

Figure 3.10 gives the weighted region of frequency formation in the asymptotic limit, i.e., short radial wavelength and large radial overtone k. This means essentially that the radial oscillations of the eigenfunction are rapid enough that a given mode samples all the "nooks and crannies" of $d\sigma/dx$. The modes of interest to us, however, are not yet in this high k limit, so they do not evenly sample $d\sigma/dx$. In general, a mode will have a non-negligible amplitude in these transition regions and will therefore sample these high weight regions. Some modes, however, will happen to have nodes in their eigenfunctions in the transition zones and will sample these regions much less. As a result, their integrated frequencies will be less than expected and their periods will be longer. This means that their periods will be closer to that of the next highest k, with the result that $\Delta P_k \equiv P_{k+1} - P_k$ will be decreased. In addition, as the modes move into the high k limit, they begin to sample the transition zone more equally, which will will minimize the effect of mode trapping from the above mechanism. These results agree with the previous investigation by Brassard et al. (1992).

The above description does not explicitly take into account the enhancement of a mode's eigenfunction in either the core or the envelop due to a composition transition zone, in other words, actual mode trapping. As such it should more properly be called something like "transition zone weighting." If we treat $d\sigma/dx$ as a potential, however, then a wave which tries to propagate through a transition zone sees the spike in $d\sigma/dx$ as a sudden change in the potential, and is partially reflected. Thus, modes can have an enhanced amplitude on one side of a transition zone relative to the other, depending on their degree of reflection from the interface.

Finally, we give a more physical argument for "transition zone weighting." In a transition zone, vertically displaced material feels a greater return force since it is intrinsically heavier than surrounding material if displaced upwards and lighter if displaced downwards. This is reflected in the enhanced Brunt-Väisälä frequency in a transition zone. Modes which sample this region will therefore tend to have higher frequencies (lower periods) than those which do not. Some modes will manage to avoid these transition zones by having periods which allow them to have nodes in or near these transition zones, so they will have lower frequencies and higher periods. These modes will be what we call trapped modes.

7.2. Phenomenology

The traditional way to obtain information about the surface layer thicknesses is to use mode trapping information for individual modes, i.e., calculate $\Delta P_k \equiv P_{k+1} - P_k$ directly from the data set and match this to numerical calculations. There is no reason why this will not work now, as long as we have enough well-identified consecutive overtones.

The physics of mode trapping should be unaffected by the presence of crystallization, with the exception that crystallization determines which periods can be normal modes. By this we mean that the set of periods which can be trapped in the outer envelope by a resonance with the hydrogen transition zone are determined by the structural parameters of the envelope, not the core. On the other hand, the degree of crystallization in the core determines the set of periods which are allowed to exist as normal modes. When periods in these two sets overlap, we find a trapped mode.

In general, a transition zone may trap a mode in the region above it *or* below it. For a mode to be trapped in the outer hydrogen layer, it needs to have a resonance with the He/H transition region such that its vertical and horizontal displacements both have a node near this interface (Brassard et al. 1992). If we imagine integrating this mode inward from the surface using the boundary conditions there, then we see that all this condition depends on is the mode frequency. Whether or not a frequency which would be trapped is indeed an allowable normal mode frequency *does* depend on the amount of crystallization in the core. From this, we see that it should be possible to disentangle the effects of crystallization and mode trapping.

More precisely, Brassard et al. (1992) find that the average period difference $\langle \Delta P \rangle_t$ between successively trapped modes is

$$\langle \Delta P \rangle_t = \frac{2\pi^2}{\sqrt{\ell(\ell+1)}} \left[\int_{rH}^{r2} N dr/r \right]^{-1}, \tag{3.38}$$

where rH is defined as the radius at the base of the hydrogen layer; the integral is therefore over the hydrogen surface layer only. We see that this does not depend on any of the properties of crystallized region, but only on those of the hydrogen envelope. They also find that the interval between successive overtones Δk is given by the ratio of this period to the average period spacing (equation 3.31):

$$\Delta k = \frac{\int_{r1}^{r2} N dr/r}{\int_{rH}^{r2} N dr/r}. \tag{3.39}$$

We find that Δk *is* a function of the crystallized mass fraction, since the inner turning point $r1$ moves outward as we crystallize our model.

In Figure 3.22, we show how mode trapping changes with different amounts of crystallization for a given model. Note that there is always a mode near 575 sec which is somewhat trapped. The mode near 630 sec also tends to be trapped. Essentially, the effect of crystallization is to shift the periods in a given model, and when some of these periods happen to "line up" with periods which can be trapped, we find a trapped mode. Thus, the set of periods which tend to be trapped are the same, regardless of the degree of crystallization. Unfortunately, the trapping due to different transition zones makes it difficult to define a trapping cycle. Furthermore, the structure of the mode trapping changes significantly as the degree of crystallization is changed by only 10%. This suggests that we will need to examine the degree of crystallization in smaller increments.

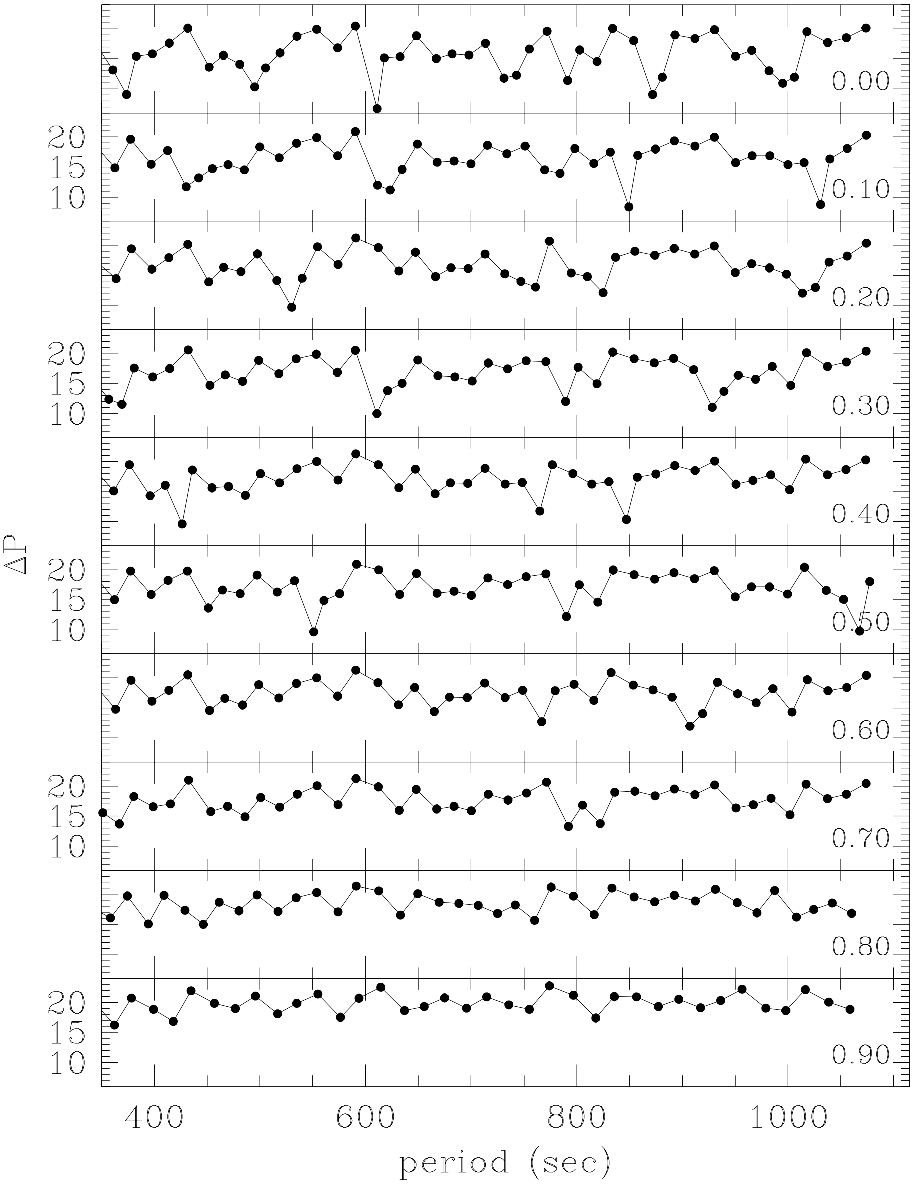

Fig. 3.22.— Forward period difference for $\ell = 2$ modes. Each panel is labelled by the degree of crystallization assumed for the model. All the other model parameters are held constant.

Figure 3.23 is a more detailed version of Figure 3.22 which shows how ΔP changes as the crystallized mass fraction is increased from 0.50 to 0.59 in increments of 0.01. First, we note that the mode trapping features for periods less than 520 sec remain unchanged as a function of crystallized mass fraction. The most significant feature, however, is a severe mode trapping feature which moves to higher periods as the degree of crystallization is increased; it is evident in the first four panels which have $M_{\rm xtal}/{\rm M}_\star$ in the range 0.50–0.54.

The open circles in Figure 3.23 represent the mode trapping inferred from data collected during the Spring 1998 WET run on BPM 37093. They show a strong trapping feature at 600 sec. If we imagine the different panels as an attempt at a fit to this data, then we see that this trapping feature will be best reproduced by models which are between 52% and 53% crystallized. At the present, we cannot examine the degree of crystallization in increments smaller than 0.01, although it is a straightforward modification to allow this; we will include this functionality in the near future. We note that this extreme sensitivity of some of the periods to the crystallized mass fraction may in principle allow us to derive very accurate values for the crystallized mass fraction, if we are able to zero in on a unique solution.

As we would imagine in a many-parameter problem such as this, there are many local minima which compete for the title of best solution. One such competitor is shown in Figure 3.24. The model is the same as that in Figure 3.23, except we have searched a different range of crystallization. Here, the observed trapping feature at 600 sec is best reproduced by a model which is between 82% and 83% crystallized. Again, we see that the trapping feature in the model is very sensitive to the crystallized mass fraction.

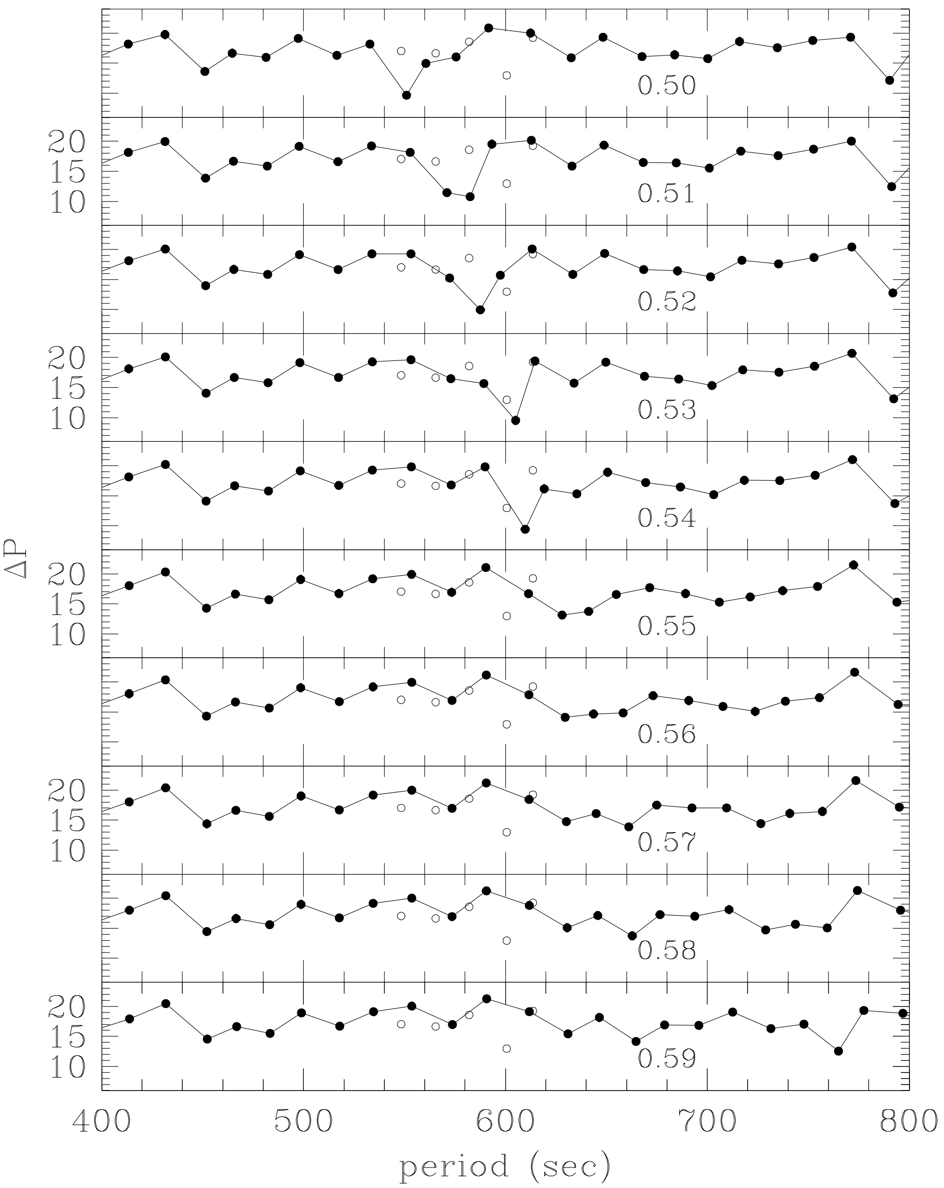

Fig. 3.23.— The filled circles connected by lines show the period spacing in the model versus the period, for degrees of crystallization varying between 50% and 59%. The open circles are from the observed period spacings in BPM 37093 from the WET run in Spring 1998, assuming that the observed modes can be identified as $\ell = 2, m = 0$ modes.

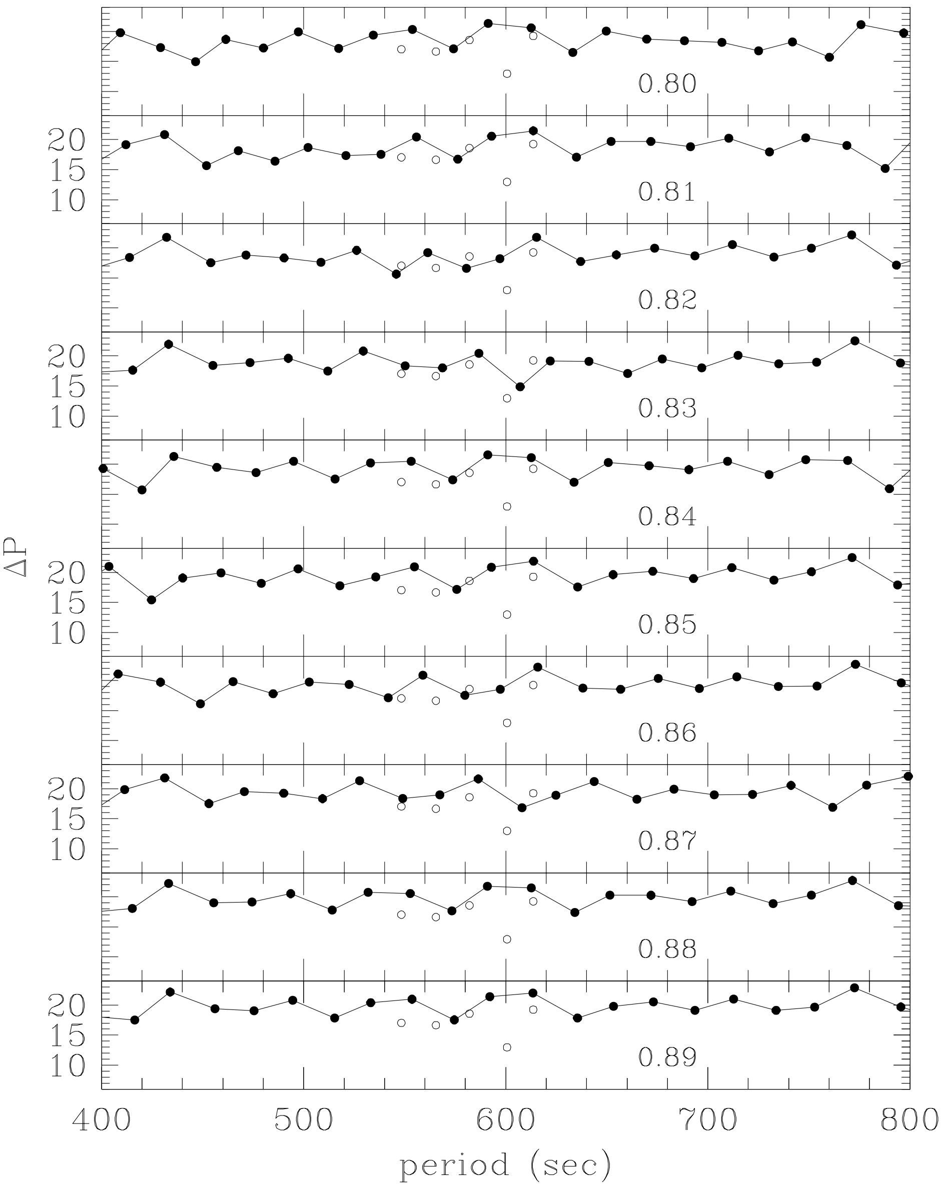

Fig. 3.24.— The same as Figure 3.23, except for values of the crystallized mass fraction between 80% and 89%.

8. Objective Fitting Procedures

We need an automated procedure for searching parameter space, both to obtain more precise fits and to address the issue of uniqueness of fit. The sensitivity of the trapping features to the crystallized mass fraction is both a blessing and a bane: It is a blessing because this should allow us in principle to determine precise values for $M_{\rm xtal}/{\rm M}_\star$, and it is a bane because in practice it requires the computation of an enormous number of models on a fine grid in order to sample the parameter space adequately.

We are currently exploring different methods which would address these issues. In one sense, the easy part of this problem is choosing a method such as "simulated annealing" or a "genetic algorithm" which can find global minima of multidimensional functions. The hard part is automatically generating the equilibrium models with a given set of fit parameters, so that these models can be examined pulsationally. Traditionally, the evolution of such models has been a "hands on" procedure, and this is true of our evolutionary models as well.

It may be possible to make use of these sophisticated fitting techniques by employing a hybrid approach. Instead of generating new evolutionary models for each new set of parameters, we can parameterize the Brunt-Väisälä frequency and vary it within a single evolutionary model. Although this is not a completely self-consistent approach, it is a very good approximation since the Brunt-Väisälä frequency depends sensitively on derivatives of the equilibrium model, and small differences in the density, temperature, and composition of the model can therefore produce large differences in the Brunt-Väisälä frequency.

The other structural parameters will be affected comparatively little by such changes, so they may be thought of as essentially constant. Since g-modes are mainly sensitive to the Brunt-Väisälä frequency (the asymptotic expression for g-mode periods involves *only* N^2 and r), we will be able to simulate changes in surface layer thickness (by moving the bumps in the Brunt-Väisälä frequency in and out) as well as in temperature (by increasing and decreasing the Brunt-Väisälä frequency locally). The only parameter not easily included in this scheme is the total stellar mass, $M_\star$, since as we change $M_\star$ we *would* expect changes in the pressure and density profiles. However, it should be possible to introduce scaling relations which would be accurate for $\sim 10\%$ changes in $M_\star$; this should be more than adequate since spectroscopic mass determinations typically result in errors which are smaller than this.

Unfortunately, this problem lies outside the scope of this thesis, although it may lie within the scope of future PhD theses at the University of Texas. The genetic algorithm in particular offers promise as a useful fitting technique (Metcalfe 1998), not only for its ability to converge to global minima, but because it can find a heterogenous "population" of solutions whose similarities tell us what we reliably know from the fit and whose differences tell us what we in principle cannot learn from a given data set. This will finally allow us to assess the uniqueness of our asteroseismological fits.

Chapter 4

Asteroseismological Signatures of Phase Separation

In this chapter we ask whether we can use asteroseismology to address the phenomenon of phase separation. There are two related ways phase separation should affect the pulsations. First, if we assume the theory of crystallization is correct and complete, then for a given initial C/O profile at a given temperature, a phase-separating model will have a different crystallized mass fraction than one in which no chemical rearrangement occurs; in the previous chapter we saw the consequences which this can have. Second, phase separation produces changes in the composition profile in the solid *and* fluid regions. Put another way, if we have two models started with the same initial C/O profile and which have crystallized to the same point, then the one which is undergoing phase separation will have a different C/O profile *in the fluid region*, and since the pulsations sample the fluid region, we could in principle tell the difference between these two cases.

We must first answer the fundamental question: Does the shape of the C/O profile significantly affect the pulsations of our white dwarf models, even in the fluid limit? If we are not sensitive to the C/O profiles in the cores of our models in the ordinary fluid cases, then we will almost certainly be unable to say anything about the profiles in our crystallizing, phase-separating models. Thus, we need to address the problem of arbitrary C/O profiles in the context of our "normal" 0.6 $M_\odot$, uncrystallized white dwarf models, as well as in the more massive 1.1 $M_\odot$ models.

First, however, we examine the effect which the process of crystallization has on the rates of period change in our models, in order to see what are the observable consequences.

1. The Question of $\dot{P}$

As a white dwarf evolves, the properties of the resonant cavity in which the g-modes propagate changes. The periods therefore should evolve with time. If we formally assume the period to be a function of the effective temperature $T_{\rm eff}$, the radius $R_\star$, and the crystallized mass fraction , $m_{\rm x} \equiv M_{\rm xtal}/{\rm M}_\star$, i.e.,

$$P \equiv P(T_{\rm eff}, R_\star, m_{\rm x}),$$

then we may write the time rate of change of the period $\dot{P} \equiv dP/dt$ as

$$\dot{P} = \frac{dT_{\rm eff}}{dt}\,\frac{dP}{dT_{\rm eff}}\bigg|_{R_\star, m_{\rm x}} + \frac{dR_\star}{dt}\,\frac{dP}{dR_\star}\bigg|_{T_{\rm eff}, m_{\rm x}} + \frac{dm_{\rm x}}{dt}\,\frac{dP}{dm_{\rm x}}\bigg|_{R_\star, T_{\rm eff}} \tag{4.1}$$

Since we are examining the role of crystallization in the pulsations, we are interested only in the third term on the RHS of equation 4.1.

The problem now consists of two parts. The first involves calculating the rate of period change as the crystallized mass fraction is varied, which we saw how to do in the previous chapter. The second involves calculating the time rate of change of the crystallized mass fraction, $dm_{\rm x}/dt$. Assuming that the standard treatments of crystallization accurately reflect the physics in white dwarf interiors, we can easily calculate $dm_{\rm x}/dt$ from our evolutionary models.

In Figure 3.16, we saw how an eigenspectrum of mode periods evolved as $m_{\rm x}$ was varied from 0.0 to ~ 1.0. Many of the periods appeared to change "rapidly" as the model crystallized. We might therefore expect that these periods would have a significantly enhanced $\dot{P}$. Computing $dP/dm_{\rm x}$ for the modes in this figure yields the somewhat chaotic looking Figure 4.1. Here, at each crystallized mass fraction, we have plotted $dP/dm_{\rm x}$ for all the $\ell = 2$ modes in the model with periods between 50 and 1000 sec. Since many of the modes have similar derivatives, the points corresponding to the different modes often lie nearly on top of each other. The utility of this plot is that it shows that the maximum values of $dP/dm_{\rm x}$ are in the range $\sim$ 1000–2000 sec. We note that the C/O profile assumed for this calculation is given by

$$X_{\rm ox} = \begin{cases} 0.80 & 0.00 \leq q \leq 0.75 \\ 0.80 - \frac{16}{3}(q - 0.75) & 0.75 < q \leq 0.90 \\ 0.0 & 0.90 < q \leq 1.00 \end{cases} \tag{4.2}$$

where $q = M_{\rm r}/M_\star$ and $X_{\rm ox}$ is the oxygen mass fraction.

If we restrict ourselves to periods between 500 and 700 sec, however, we find less scatter in the $dP/dm_{\rm x}$ relationship, and hence smaller maximum values. This is shown in Figure 4.2. We now see that the largest period changes are in the 500–1000 sec range, although when $m_{\rm x}$ is near 0.40 and 0.65, the value is less than 100 sec.

Clearly, the other half of this problem is calculating the magnitude of $\dot{m}_{\rm x} = \dot{M}_{\rm xtal}/{\rm M}_\star$. In Figure 4.3, we show how the magnitude of $\dot{m}_{\rm x}$ (in sec^{-1}) changes as a 1.1 M$_\odot$ model cools. In the vicinity of the ZZ Ceti instability strip

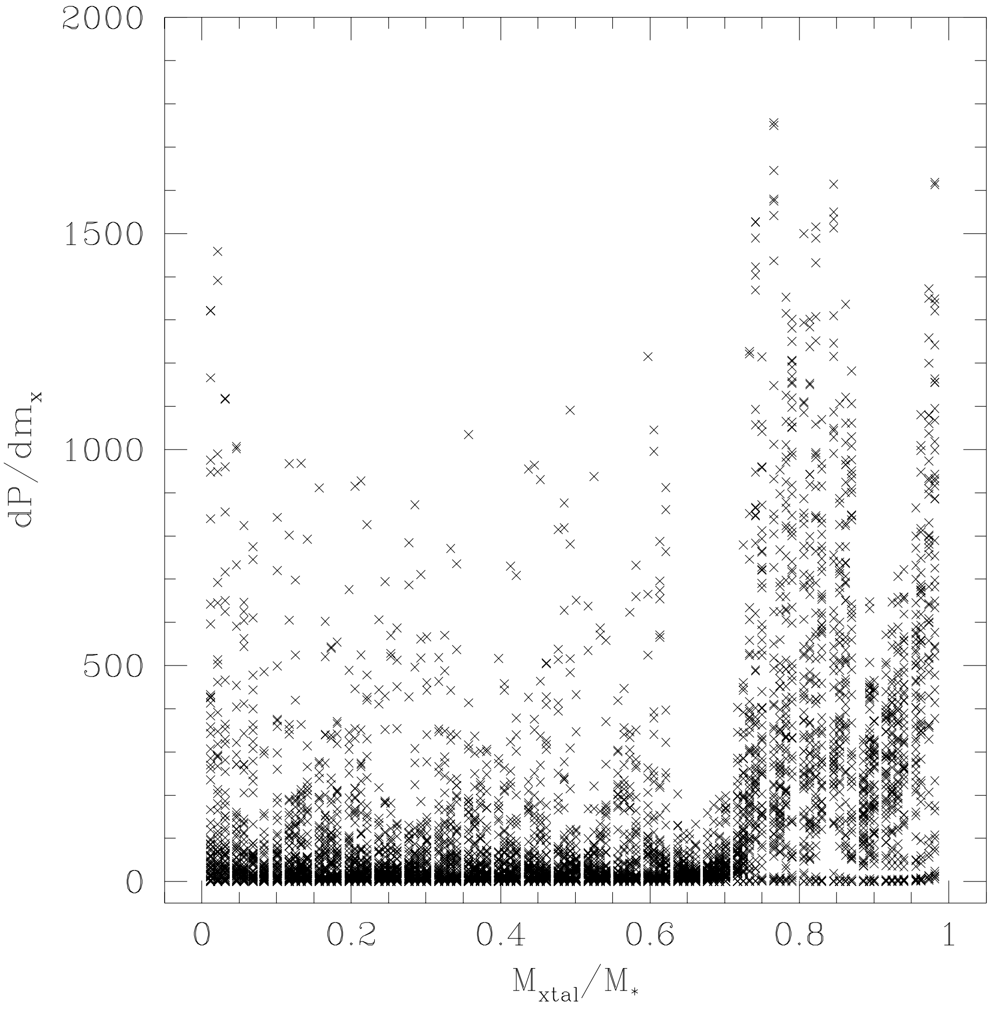

Fig. 4.1.— $dP/dm_{\rm x}$ as a function of $m_{\rm x} = M_{\rm xtal}/{\rm M}_\star$ for the periods shown in Figure 3.16.

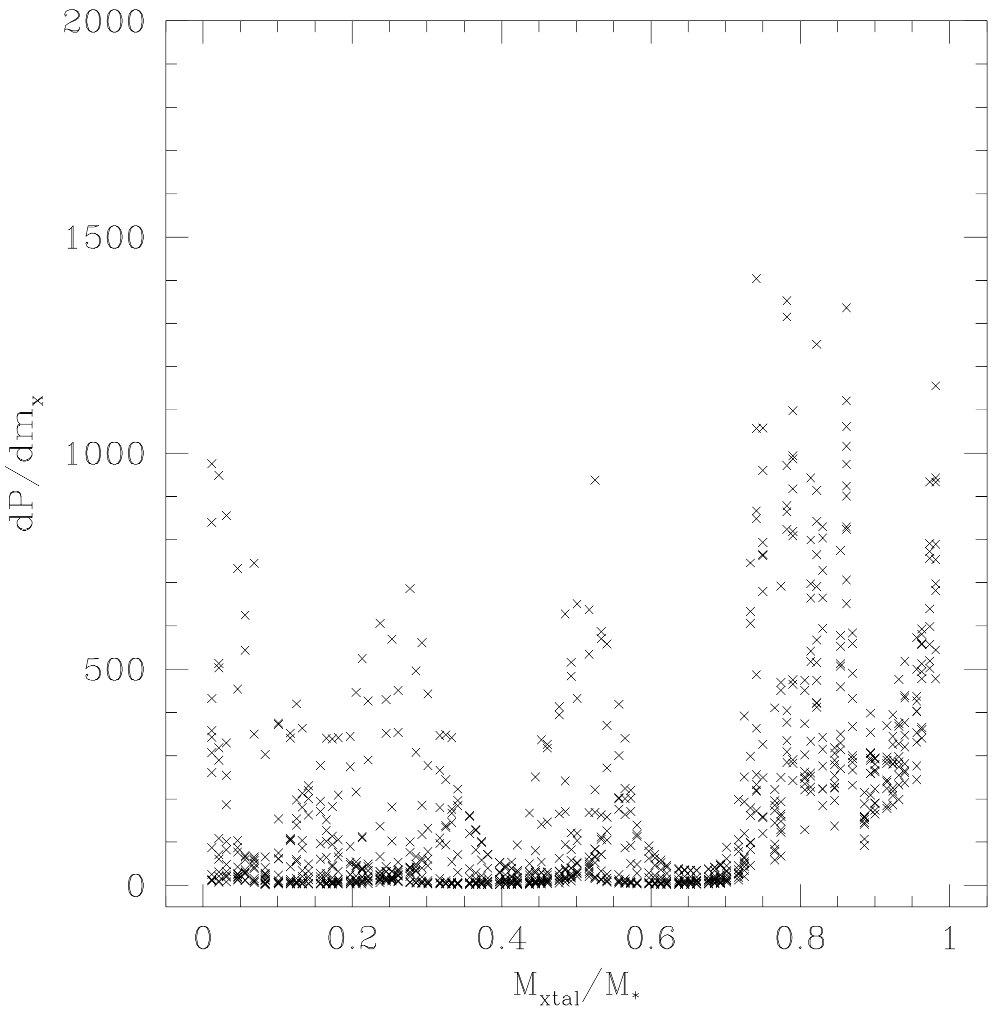

Fig. 4.2.— The same as Figure 4.1, except we have only plotted dP/dm_{x} for the periods between 500 and 700 sec. Note that near 0.40 and 0.65 the periods are quite insensitive to the crystallized mass fraction.

($T_{\rm eff} \sim 12,000$ K), we see that $\dot{m}_{\rm x} \sim 4.5 \cdot 10^{-18}$ sec^{-1}. For this temperature range and C/O profile, we have $m_{\rm x} \sim 0.8$, for which the larger derivatives in Figure 4.1 are ~ 1500 sec. Using these values, the third term in equation 4.1 gives a value of $\dot{P} \approx 7 \cdot 10^{-15}$ s/s. Thus, a few of the modes will have period changes this large. Modes between 500 and 700 sec will have somewhat smaller maximum values, with $\dot{P} \approx 5 \cdot 10^{-15}$ s/s.

The most sensitive measurements yet made for a $\dot{P}$ in a pulsating white dwarf are those for the star G117-B15A. Kepler, Nather, & Metcalfe (1998) find a value of

$$\dot{P} = (1.2 \pm 2.2) \cdot 10^{-15} \mathrm{s/s},$$

where they have used data from 1975 through 1997 to determine the stability of the mode. We estimate that a 10 year baseline of observations would be necessary to see the somewhat larger $\dot{P} \sim 6 \cdot 10^{-15}$ s/s which we would predict for the crystallizing pulsator BPM 37093. While this sounds like a very difficult task, 5 years of observational data already exist for this star.

2. The Effect of a Non-uniform C/O Profile

In this section we explore the effect which a non-uniform C/O profile has on the pulsations, both in the context of our "normal" 0.6 $M_\odot$ white dwarf models, as well as for the higher mass 1.1 $M_\odot$ models which are more appropriate for crystallizing ZZ Ceti's.

The profiles which we choose for this examination are extreme cases. The first profile is a "flat" or constant 50:50 C/O ratio throughout the cores of our white dwarf models. The other profile is taken to be pure O in the center,

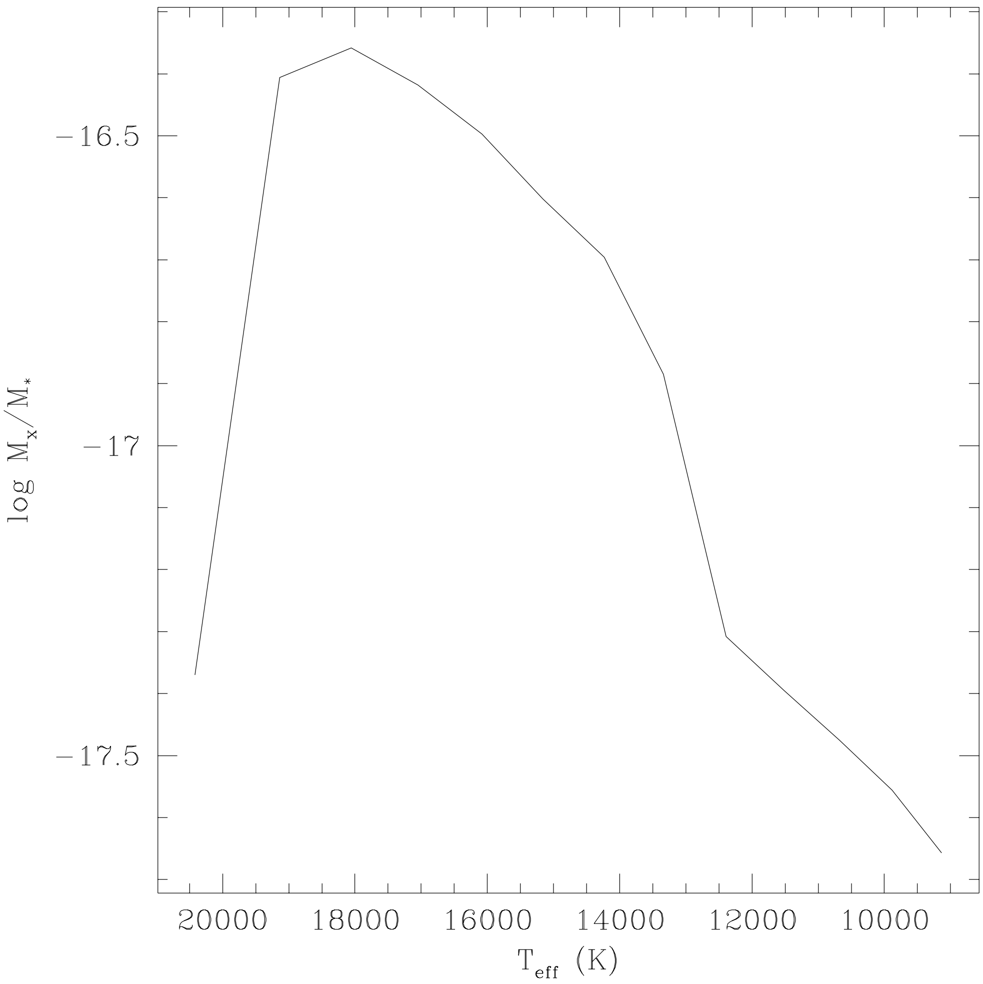

Fig. 4.3.— dm_x/dt as a function of $T_{\rm eff}$ for a 1.1 $M_\odot$ model with the C/O profile specified in equation 4.2.

decreasing linearly with mass to pure C at the 0.99 mass point. For all models, we fix $T_{\rm eff} = 11{,}800$ K.

2.1. The 0.6 $M_\odot$ Models

We first start with models which should remain fluid until they are well past the ZZ Ceti instability strip, the 0.6 $M_\odot$ models. In Figure 4.4, we compare the period weight function for the two extreme profiles; the surface layer masses are given by $M_{\rm He}/M_\star = 10^{-2}$ and $M_{\rm H}/M_\star = 10^{-4}$. The two curves disagree only in the region where they have different C/O profiles, i.e., $\log(1 - M_r/M_\star) < 1$. The dotted curve is the linearly decreasing oxygen profile. It is higher in the core because the changing composition enhances the Brunt-Väisälä frequency through the modified Ledoux term, which makes the modes more sensitive to this region. The increased Brunt-Väisälä frequency in the core of the linear profile results in a period spacing which is 10% shorter than that produced by the constant C/O profile. As a result, the mode periods themselves should be modified at the 10% level. Since such an enhanced Brunt-Väisälä frequency shortens the periods but does not introduce strong mode trapping, this could mimic the effect of changing the total stellar mass, $M_\star$.

2.2. The 1.1 $M_\odot$ Models

We now examine models which should be crystallized in the ZZ Ceti instability strip, using the same two C/O profiles. In figure 4.5, we plot the period weight function in the case of two 1.1 $M_\odot$ models, each with $M_{\rm He}/M_\star = 10^{-3}$, and $M_{\rm H}/M_\star = 10^{-5}$. We have computed the weight function as if the entire model were fluid; in general, some fraction of it will probably be crystallized and

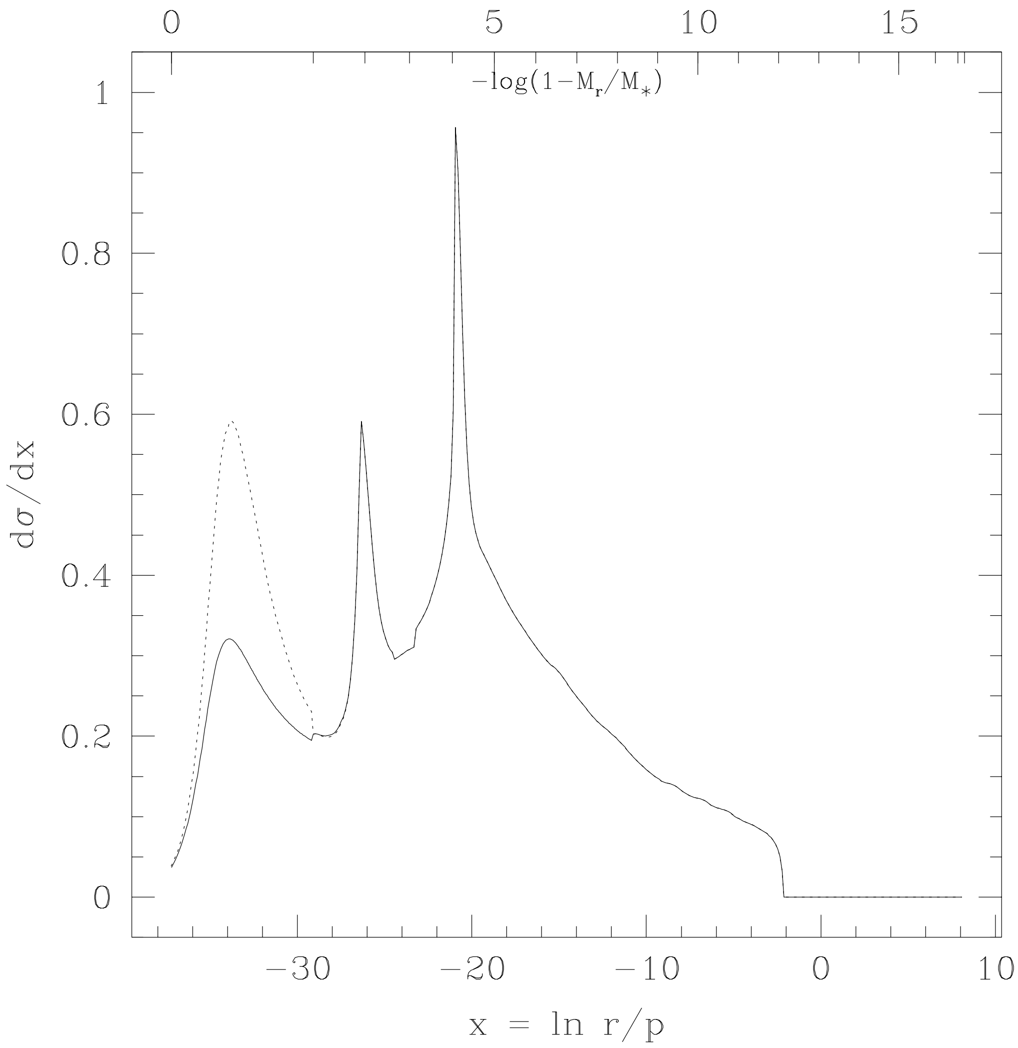

Fig. 4.4.— The period (frequency) weight function for 0.6 $M_\odot$ models with two "extreme" profiles. The dotted line is the model with a linearly decreasing oxygen mass fraction, and the solid line is for the 50:50 uniform C/O mixture.

therefore have zero weight in determining the period.

Clearly, the non-uniform C/O profile makes a huge difference in this case. The period spacing of the linear profile is just 73% that of the flat profile. This is not that much smaller an effect than going from $\ell = 1$ modes to $\ell = 2$ modes! Of course, if we include crystallization in the standard way, then much of this inner region will be excluded; for the present case, the model with the linear profile should be 70% crystallized. If we assume that both models are 70% crystallized, then the difference in period spacing becomes only 5%.

These experiments show that the C/O profile can make a large difference in the period spectra of our white dwarf models. At higher mass, this effect is even larger, except that in a self-consistent analysis the models would tend to be significantly crystallized, which would reduce the effect. This suggests that slightly less massive models might show this effect to the greatest degree, since they would be less crystallized but still fairly massive, with $\mathrm{M}_\star \sim 1.0\,\mathrm{M}_\odot$.

3. "Self-consistent" C/O Profiles

Here I have used the term "self-consistent" for lack of a better term. When this term is used, it generally means that one aspect of the problem is self-consistent, but not necessarily any others. In the present case, I merely mean that since the C/O profiles in actual stars are believed to be the result of an epoch of nuclear burning, we have used the results of such calculations (provided by Salaris et al. 1997) for our C/O profiles. While these calculations are probably not the last word on the subject, they do represent the current "state-of-the-art". For our purposes, the important feature of the profiles is

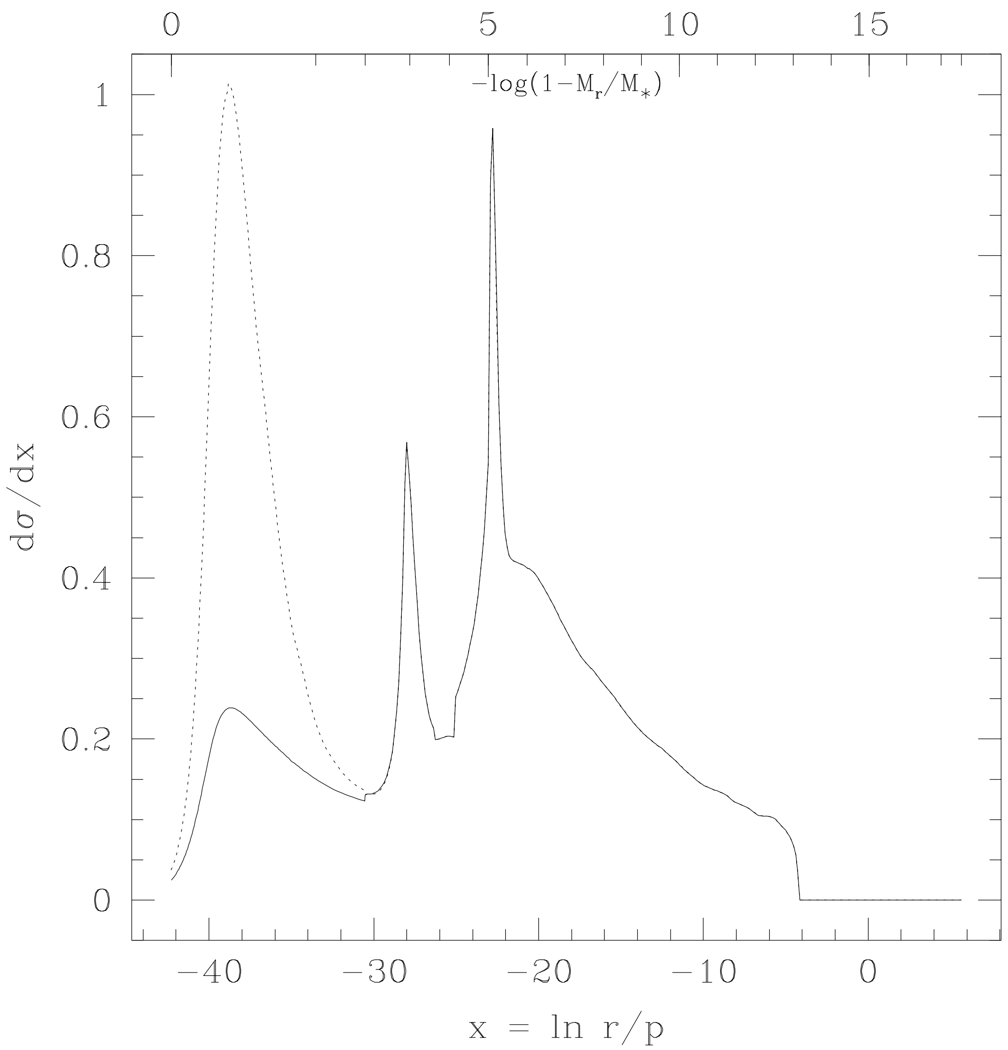

Fig. 4.5.— The period (frequency) weight function for 1.1 $M_{\odot}$ models with two "extreme" profiles. For the purposes of this plot, we are assuming that the entire model is fluid. The dotted line is for the linear oxygen profile and the solid line is for the flat profile.

that they are not flat or piecewise linear as are the previous profiles we have examined. In fact, flat or piecewise linear profiles are what is normally assumed in most asteroseismological treatments (e.g., Bradley, Winget, & Wood 1993; Bradley 1993; Bradley & Winget 1994a, 1994b; Bradley 1996).

In Figure 4.6, we show the two different profiles. The solid line corresponds to the initial profile and also the final profile in the case of no phase separation, and the dashed line is the final profile in the case that the model has crystallized outward to the 69% mass point. For the pulsational analysis, we will therefore be assuming that each of our models is 69% crystallized. Note that the flat portion of the dashed curve in Figure 4.6 in region 0.70–0.99 is a result of the fluid mixing which has occurred as a result of phase-separation; these layers have been mixed and homogenized so that they have the same composition. Both profiles still retain a sharp drop in the oxygen abundance at the ~ 0.99 mass point.

In Figure 4.7, we plot the period weight function for the two C/O profiles in Figure 4.6. The weight functions are plotted as if both models were completely fluid so that the g-modes would be able to sample the deep core. The vertical dashed line indicates the lower limit to g-mode propagation if the models are considered to be 69% crystallized.

Several features present themselves in this plot. First, since these two models differ only in the C/O composition in the core (the mass, temperature, and layer masses are the same), we see that the weight function is identical in the region $-\log(1 - M_r/M_\star) > 2$. Second, the weight function in the core inside the 69% mass point is very different in the two cases. In fact, there is a 10% difference in the asymptotic period spacing of these models due to this

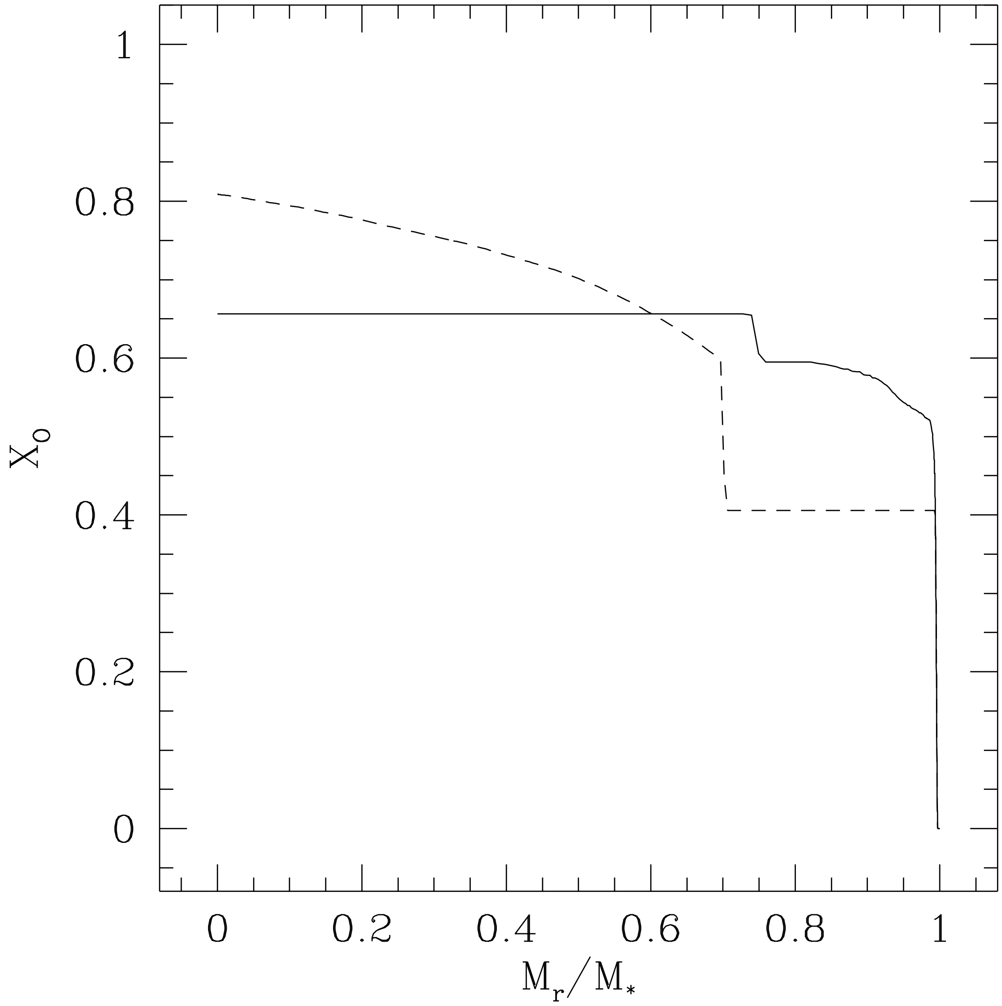

Fig. 4.6.— The difference in profiles due to phase separation for $\sim 1\ M_\odot$ models, as computed by Salaris et al. (1997). The solid line is the initial profile and the dashed line is the profile after crystallization has proceeded to the 69% mass point.

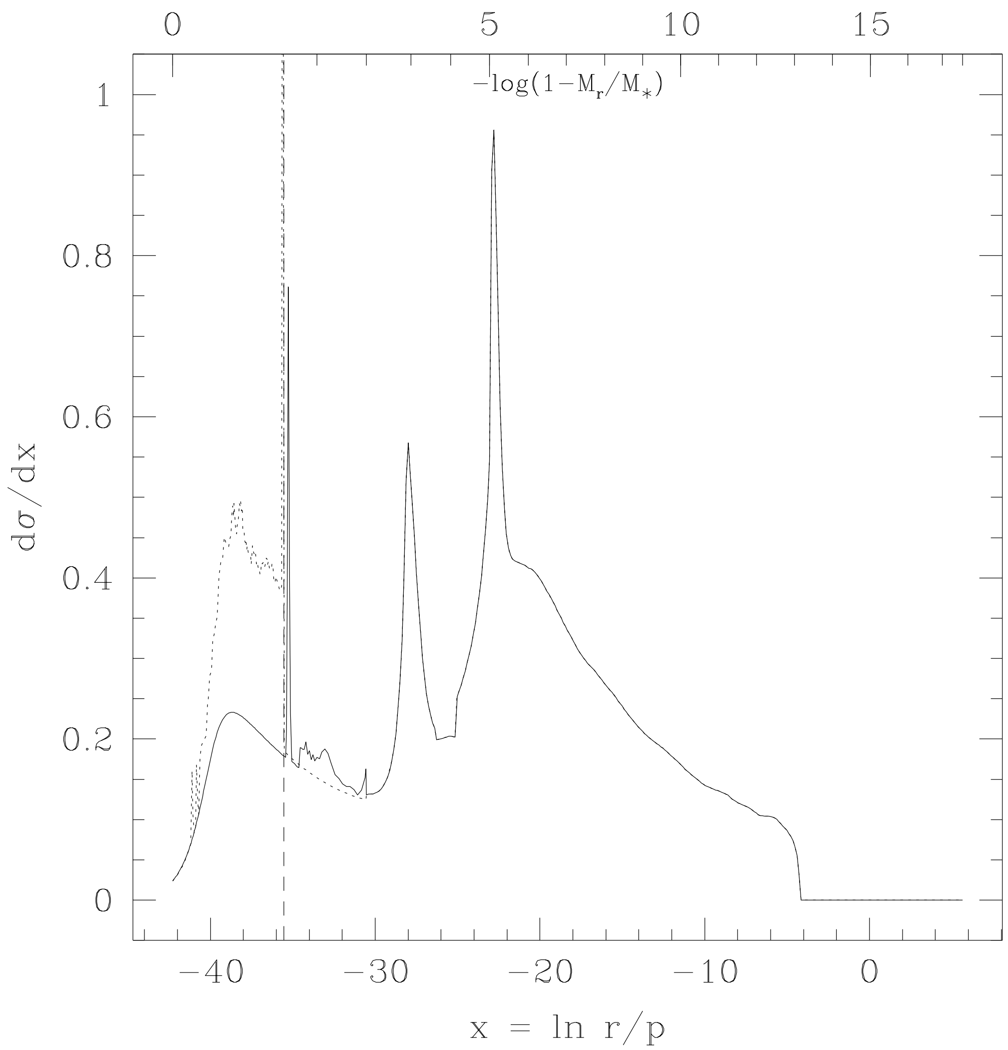

Fig. 4.7.— The period (frequency) weight function for the two different C/O profiles shown in Figure 4.6. The solid line and dotted lines correspond to the cases with and without phase separation, respectively. The vertical dashed line shows the location of the 69% mass point.

region. This shows us that the C/O profile can have a major effect on the pulsations, as we have already seen. In the case considered here, however, this region is off limits since we consider it to be crystallized. Integrating in the fluid region only, we find that there is only a 0.2% change in the asymptotic period spacing between the two cases. In this case, crystallization completely masks any potential changes in the Brunt-Väisälä frequency due to phase separation.

Although crystallization has removed the sensitivity of our models to the composition profiles in the core, it has simultaneously removed the uncertainties of our period determinations which are based upon those unknown profiles. For uncrystallized models, we have shown that differing C/O profiles can still have a substantial effect on the calculated periods.

Chapter 5

Conclusion

We have seen in the previous chapters that the physics of crystallization manifests itself in many different ways in white dwarf stars. In the context of white dwarf cooling, the release of latent heat and the phase separation of carbon and oxygen during crystallization can provide additional sources of energy for the white dwarf stars, allowing them to cool more slowly. Since we use white dwarfs as chronometers for the age of the local Galactic disk ("white dwarf cosmochronometry"), we need to know the magnitude of this effect with respect to our calculated white dwarf ages. From our investigations, we find this increment to our model white dwarf ages to be no more than 1.5 Gyr, with a most likely value of less than 1 Gyr.

Although the physics of crystallization in white dwarf interiors rests on a sound *theoretical* foundation, neither it nor the theory of phase separation have been tested experimentally in conditions simulating white dwarf interiors. To this end, we have explored the consequences which a crystallized core has on the oscillations of our white dwarf models, in the hopes of diagnosing whether crystallization and phase separation occur in actual white dwarf stars. For the star BPM 37093, we have used our results along with a tentative mode identification for the periods in the WET data to obtain a relationship between the thickness of its surface hydrogen layer and its degree of crystallization.

1. Discussion of Results

In Chapter 2, we showed that the standard approach to phase separation (e.g., Isern et al. 1997; Salaris et al. 1997) is valid, and we verified it directly in the case of a zero-temperature model supported only by electron degeneracy pressure (Chandrasekhar 1939). We then demonstrated that phase separation, if it occurs, probably introduces about a ~ 0.6 Gyr increment to the ages which we calculate for the oldest white dwarfs. The maximum value which we were able to produce for this effect was ~ 1.5 Gyr, in which we assumed an artificial profile with a 50:50 C/O ratio throughout the cores of our models; more realistic profiles based on nuclear reaction rates produce cores which are 70–80% oxygen, so that phase separation produces less of an effect. We therefore believe that the ages of the local Galactic disk derived from white dwarf cosmochronometry change by less than one Gyr, depending on whether or not phase separation occurs.

In Chapter 3, we reviewed the basics of nonradial pulsation theory of normal fluid stars. In addition, we derived a dispersion relation for the torsional modes and determined the region of propagation of these modes in models with a crystalline core. However, these modes cannot propagate through the fluid layers, so they should not be detectable at the photosphere; their coupling to other modes should also be quite small, since their angular eigenfunctions are orthogonal to the ordinary spherical harmonics of p- and g-modes. We also showed that the p-mode periods are only affected at the level of a few percent.

For the g-modes, we found that they are effectively excluded from the crystalline cores of our models, so that their region of propagation is limited to the fluid layers only. Using a "hard sphere" boundary condition, we found we could reproduce the periods calculated using the self-consistent global approach to better than 1 part in 10^4. The main effect of a crystallized core in our models is to widen the average period spacing between consecutive radial overtones; the period spacing can be increased by over 30% for crystallized mass fractions greater than 90% in our models.

In previous asteroseismological analyses of the objects GD 358 and PG 1159, we have used the information contained in the variations from the mean period spacings between consecutive radial overtone modes. These variations are produced when a mode has a resonance with the surface hydrogen or helium layer, for example. We then say that it is "trapped" in the layer, but more accurately it simply has an enhanced amplitude in that layer. Clearly, a trapped mode does not sample a model in the same way that an untrapped mode does, and it is this which produces the variations in period spacing. Typically, we use this mode trapping information to determine the masses of the surface hydrogen and helium layers. Since the physics in these layers is unaffected by any crystallization which may be occurring in the cores of our models, we expect to be able to use mode trapping information in the case of our crystallized pulsating models.

As a preliminary example, we attempted to interpret the periods seen in a recent WET run on BPM 37093, a 1.1 $M_\odot$ DAV which should be in the process of crystallizing. For the purpose of this analysis, we assumed the modes were all consecutive radial overtones with $\ell = 2$, $m = 0$, although we do not have firm mode identifications; in the future, we will use the technique described in Robinson et al. (1995) to determine the ℓ values for these modes. We obtained a relation between the hydrogen layer mass and the crystallized mass fraction. For instance, a best-fitting model which is 50% crystallized must have a hydrogen layer mass satisfying $-6 \leq \log M_{\rm H}/M_\star \leq -5$.

In Chapter 4, we considered the pulsational consequences which phase separation might have, with an eye as to how this might be measurable in an asteroseismological sense. In the process of this, we found that gradients in the C/O profiles in the cores of our white dwarf models could have quite significant effects on the periods of g-modes. The C/O profiles computed by Salaris et al. (1997, the solid line in Figure 4.6) were relatively flat throughout most of the core, however, so this effect was greatly minimized; if these profiles accurately represent the true profiles in these stars, we probably cannot tell pulsationally whether or not phase separation has actually occurred in a given star. We should keep in mind that the C/O profiles in actual white dwarfs may *not* be as constant, and that this effect could play a much larger role.

2. The Future

The field of white dwarfs is ripe for progress. This is due partly to the increasing number of large ($\sim$ 8 meter) telescopes and partly due to technological improvements such as adaptive optics, which can give smaller telescopes the same signal to noise as larger ones. This will allow us to make much more detailed observations of white dwarfs than ever before. As an example of this, Van Kerkwijk et al. (1997) used the Keck telescope to obtain time-resolved spectroscopy of the DAV white dwarf G29–38. Due to the high data quality, they were able to measure the difference in phase between the luminosity perturbations and the velocity perturbations at the surface of this star, which may be a key to unlocking the physics which is occurring at the base of its convection zone.

In addition to using large telescopes, surveys using specialized medium and small-sized telescopes promise to dramatically increase the number of known white dwarfs. For instance, the Texas Deep Sky Survey (TDSS) is a survey designed to find white dwarfs over a 100 square degree area of the sky (Claver 1995); when completed, this survey will more than double the number of cool white dwarfs in the last luminosity bin at the turndown of the WDLF in Liebert, Dahn, & Monet (1988), and add hundreds of faint white dwarfs with $\log L/L_{\odot} < -3$. The Sloan Digital Sky Survey is a project which will map 10,000 square degrees of the sky. If we assume the same sensitivity for this survey as for the TDSS (which is an underestimate), then this survey has the potential to discover tens of thousands of faint white dwarfs. This will greatly reduce the observational errors on the observed WDLF to the point where we can obtain information about star formation rates, as well as about the detailed physics of white dwarf interiors and envelopes.

Given this outlook, it is reasonable to imagine that we will find other stars like BPM 37093, which are high-mass pulsators that are presumably crystallized. Since it is possible to make greater progress when a class of objects exists rather than when there is just a single isolated example, we will have more tools at our disposal when we attempt an analysis of these stars. For example, the DAV white dwarfs individually pulsate in several frequencies, but no one of them (at least at one point in time) has enough periods that we can make an asteroseismological fit. Considering the class as a whole, however, Clemens (1993) showed the total set of periods which they exhibit is consistent with a nearly identical population of white dwarfs, all of which had $\mathrm{M}_\star \approx 0.6\,\mathrm{M}_\odot$, $M_{\mathrm{He}}/\mathrm{M}_\star \approx 10^{-2}$, and $M_{\mathrm{H}}/\mathrm{M}_\star \approx 10^{-4}$.

A difficulty in all asteroseismological analyses is mode identification. The technique applied by Robinson et al. (1995) can determine the ℓ value of a mode, but not the m value. In addition, this technique assumes that a given mode in the pulsating star is oscillating with the spatial structure of a pure spherical harmonic at its surface; if this is not the case, the technique may return ambiguous results. At present, the most reliable technique for identifying the m value of a given mode is to observe it as one of the $2\ell + 1$ components of a rotationally split multiplet, all of which are observed to be present in the power spectrum.

If we are ever able to model reliably the amplitudes of the nonlinear sum and difference frequencies, we *will* be able to tell what the m values and what the ℓ values are. This is because any general nonlinear effect, whether it is a mode coupling or a surface nonlinearity effect, will produce nonlinear frequencies which have a different angular structure than the parent frequencies. The payoff will be a unique fit for the physical amplitudes in the star and their ℓ and m values. Brassard, Fontaine, & Wesemael (1995) attack this problem by treating the nonlinear response of the local flux at the stellar surface to the temperature perturbations, i.e., $L \propto T^4$; they have successfully applied this method to some of the ZZ Ceti's. In order for a program such as this to be successful, however, we must correctly identify the most important nonlinear processes which are present in white dwarf pulsations.

A persistent bane of stellar evolution theory has always been the treatment of convection. An even more complicated problem is that of the interaction of pulsations and convection; in most pulsating stars, this problem is prohibitively complicated. For white dwarf stars, however, the situation is more promising. This is because the convective turnover timescale for the rising and sinking fluid parcels is less than 1 sec in models of DAV white dwarfs. Thus convection, while still a nuisance, at least responds nearly instantaneously to the pulsations. We are therefore able to treat the convection zone as continuously reacting to the "slow" pulsations which are of order 100's of seconds. This problem has recently been treated by Wu (1997). Her work revisits the problem of the role of convection in the pulsations of the ZZ Ceti's, and complements and confirms the earlier pioneering work of Brickhill (e.g., Brickhill 1991a, b).

This approach to convection offers us the hope that by understanding the pulsation-convection interactions we may be able to distinguish between different theories of convection. While the analyses of Wu and Brickhill have been based on the mixing length theory of convection, more physical treatments of convection, such as by Canuto, Goldman, & Mazzitelli (1996) and Canuto & Dubovikov (1998), could in principle also be used. Thus, white dwarf stars could provide the critical laboratory for deciding among these theories. This would be of importance to the entire field of stellar evolution.

3. Summing Up

The results presented in this thesis address the fundamental process of crystallization in white dwarf stars. Whether or not it occurs has major ramifications on the theory of white dwarf cooling and hence on Galactic ages determined from the WDLF. We calculated the effect which the associated phenomenon of phase separation could have on white dwarf ages and found it to be of order 1 Gyr or less. We then developed the general theory of white dwarf pulsations in partially crystallized models in the hope that we will be able to observationally determine whether crystallization occurs in the way that we think it does.

We see that the field of white dwarf research offers a great deal of promise for the future; the white dwarf stars have many things to tell us, if only we are patient enough to listen.

Appendices

Appendix A

Spheroidal Oscillation Equations in a Crystalline Medium

1. The Equations

We define ξ_r and ξ_h, the radial and horizontal parts of the total displacement, in terms of the total vector displacement, i.e.,

$$\vec{\xi} = \left[\xi_r(r), \xi_h(r)\frac{\partial}{\partial\theta}, \xi_h(r)\frac{1}{\sin\theta}\frac{\partial}{\partial\phi}\right] Y_\ell^m(\theta,\phi). \tag{A.1}$$

We take the following equations from Hansen & Van Horn (1979). The oscillation variables are

$$z_1 = \frac{\xi_r}{r},$$

$$z_2 = \frac{1}{\mu_0}\left(\lambda\alpha + 2\mu\frac{d\xi_r}{dr}\right),$$

$$z_3 = \frac{\xi_h}{r},$$

and

$$z_4 = \frac{\mu}{\mu_0}\left(\frac{d\xi_h}{dr} - \frac{\xi_h}{r} + \frac{\xi_r}{r}\right),$$

where ξ_r and ξ_h are the radial and horizontal displacements, respectively, as defined in equation A.1, r is the radius, $\lambda = \Gamma_1 p - \frac{2}{3}\mu$, μ is the shear modulus, $\alpha \equiv \frac{1}{r^2}\frac{d}{dr}\left(r^2\xi_r\right) - \hat{\ell}\frac{\xi_h}{r}$, with $\hat{\ell} \equiv \ell(\ell+1)$. These variables are the same as those in Hansen & Van Horn (1979) except that we have divided z_2 and z_4 by $\mu_0 \equiv \mu(r=0)$, so that the equations are dimensionless.[1] The fourth order system of equations (in the Cowling approximation) is then

$$\begin{aligned}
rz_1' &= -(1+2\lambda\delta)z_1 + \mu_0\delta z_2 + \lambda\hat{\ell}\delta z_3, \\
rz_2' &= \frac{1}{\mu_0}(-\sigma^2\rho r^2 - 4\rho g r + 4\pi G\rho^2 r^2 + 4\mu\beta\delta)z_1 - 4\mu\delta z_2 \\
&+ \frac{\hat{\ell}}{\mu_0}(\rho g r - 2\mu\beta\delta)z_3 + \hat{\ell}z_4, \\
rz_3' &= -z_1 + \frac{\mu_0}{\mu}z_4, \\
rz_4' &= \frac{1}{\mu_0}(g\rho r - 2\mu\beta\delta)z_1 - \lambda\delta z_2 \\
&+ \frac{1}{\mu_0}\left\{-\rho\sigma^2 r^2 + 2\mu\delta\left[\lambda(2\hat{\ell}-1) + 2\mu(\hat{\ell}-1)\right]\right\}z_3 - 3z_4,
\end{aligned}$$

where the prime denotes $\frac{d}{dr}$, $\delta \equiv (\lambda + 2\mu)^{-1}$, $\beta \equiv 3\lambda + 2\mu$, g is the acceleration due to gravity, and ρ is the density.

2. Central Boundary Conditions

Since the models we are considering are crystallized in the center, we need to obtain the boundary conditions in the center so that we may begin the outward integrations. If we assume that the solutions go like r^s near the center, we find four solutions: $s = \ell - 2, \ell, -(\ell+1), -(\ell+3)$. Only the first two solutions are regular at the origin, so they span the space of physical solutions. The general

[1]We note that there is a typographical error in the definition of z_4 in Hansen & Van Horn (1979)—an additional factor of $1/r$—but it does not propagate throughout the rest of their formulae.

solution near the center is therefore given by

$$\{z_i\} = a \begin{pmatrix} 1 \\ 2(\ell-1) \\ 1/\ell \\ 2(\ell-1)/\ell \end{pmatrix} r^{\ell-2} + b \begin{pmatrix} \frac{(\ell+1)[\lambda\ell+\mu(\ell-2)]}{2[\lambda\ell(\ell+2)+\mu(\ell^2+2\ell-1)]} \\ \frac{(\ell+1)[\lambda(\ell^2-\ell-3)+\mu(\ell^2-\ell-2)]}{\lambda\ell(\ell+2)+\mu(\ell^2+2\ell-1)} \\ \frac{\lambda(\ell+3)+\mu(\ell+5)}{2[\lambda\ell(\ell+2)+\mu(\ell^2+2\ell-1)]} \\ 1 \end{pmatrix} r^{\ell},$$

where a and b are arbitrary coefficients and where μ and λ in the above formula are taken to have their central values. These two solutions for the eigenfunction near the center are equivalent to the relations given in Crossley (1975), if the Cowling approximation is used.

3. The Solid/Fluid Interface

In practice, we integrate each independent solution outward from the center. With the exception of z_3, the $\{z_i\}$ are continuous at the solid/fluid interface. Since $z_4 = 0$ in the fluid, we choose the ratio of a and b such that z_4 vanishes at this interface. This leaves only one overall normalization constant. Furthermore, $y_1 = z_1$ at the boundary. Since z_2 is also continuous, we have

$$z_2 = \lambda\alpha/\mu_0 = \lambda V_g(y_1 - y_2)/\mu_0,$$

where we have used the oscillation equations in the fluid to express α in terms of the Dziembowski variables $\{y_i\}$. At the fluid/solid interface, if we solve for the $\{y_i\}$ in the fluid in terms of the $\{z_i\}$ in the solid then we find

$$\begin{aligned} y_1 &= z_1, \\ y_2 &= z_1 - \frac{\mu_0}{\lambda V_g} z_2, \end{aligned}$$

where $V_g = gr/c_s^2$, and λ is now $\Gamma_1 P$ since μ is zero in the fluid. Since we now have specified y_1 and y_2 (up to an overall normalization constant which is present in the $\{z_i\}$), we can now integrate the normal oscillation equations in the fluid (in the Cowling approximation) out to the photosphere of the model.

The main difficulty in applying this procedure is that numerical noise can come to dominate the integrations in the crystalline core. The model which Hansen & Van Horn (1979) considered was a pure Fe core model near 10,000 K. As a result, the theory of crystallization suggested it should be about 99.9% crystallized by mass. The technique which we have used would probably not be viable for this case. The problem is that the two independent solutions, while quite different near the center, become almost linearly dependent farther out. Thus, we lose the ability to calculate the "difference" between the two solutions which is needed in order to set z_4 equal to zero at the solid/fluid interface. For our program, numerical noise dominates this process for g-modes in models which are more than 98% crystallized.

In terms of the physics, however, we are somewhat over-dramatizing the situation, since nearly all of the pulsational results in this paper are based on the simple approximation that $y_1 = 0$ at the solid/fluid boundary. From the self-consistent treatment, we have found this to be an extremely good approximation from 0% crystallization to 98% crystallization, and we have no reason to believe this situation will change at higher amounts of crystallization. Using this simplified treatment ($y_1 = 0$ at the solid/fluid boundary), we are therefore able to treat accurately arbitrary degrees of crystallization.

4. The Boundary Conditions on $\Phi'(r)$ at the Crystallization Boundary

The perturbations to the gravitational potential are, of course, generated by the perturbations in the density. They may therefore be written as

$$\Phi'(\mathbf{r}) = G \int dV' \frac{\rho'(\mathbf{r}')}{|\mathbf{r}-\mathbf{r}'|}, \tag{A.2}$$

where we have assumed that the density vanishes at the surface. If we now write $\Phi'(\mathbf{r}) = \Phi'(r) Y_\ell^m(\theta,\phi)$ and $\rho'(\mathbf{r}') = \rho'(r') Y_\ell^m(\theta',\phi')$ and use the usual expansion of $|\mathbf{r}-\mathbf{r}'|$ in surface harmonics, then we arrive at the result of (1976):

$$\Phi'(r) = \frac{4\pi G}{2\ell+1}\left\{ r^{-(\ell+1)} \int_0^r \rho'(r') r'^{\ell+2} dr' + r^\ell \int_r^R \rho'(r') r'^{-\ell+1} dr' \right\}. \tag{A.3}$$

We will assume that there is no motion for $r < r_{\mathrm{x}}$, where r_{x} is the radius of the crystallization boundary. Thus, we have $\rho'(r) = 0$ for $r < r_{\mathrm{x}}$. If we now take a derivative of $\Phi'(r)$ in the region $r_{\mathrm{x}} < r < R$, we find

$$\begin{aligned} \frac{d\Phi'(r)}{dr} &= \frac{4\pi G}{2\ell+1}\left\{ -(\ell+1)\, r^{-(\ell+2)} \int_0^r \rho'(r') r'^{\ell+2} dr' \right. \\ &+ \left. \ell\, r^{\ell-1} \int_r^R \rho'(r') r'^{-\ell+1} dr' + r\rho'(r) - r\rho'(r) \right\}, \end{aligned}$$

where we have assumed that the density is zero at the outer boundary. Evaluating this at $r = r_{\mathrm{x}}$, and remembering that $\rho'(r) = 0$ for $r < r_{\mathrm{x}}$, we find that the first integral vanishes, which, along with the cancellation of the last two terms, leaves only

$$\frac{d\Phi'(r_{\mathrm{x}})}{dr} = \frac{4\pi G}{2\ell+1}\, \ell\, r_{r_{\mathrm{x}}}^{\ell-1} \int_{r_{\mathrm{x}}}^R \rho'(r') r'^{-\ell+1} dr'. \tag{A.4}$$

Finally, using equation A.3 to evaluate $\Phi'(r)$ at $r = r_{\mathrm{x}}$, and combining it with equation A.4, we obtain the final result:

$$\frac{d\Phi'(r_{\mathrm{x}})}{dr} = \frac{\ell}{r_{\mathrm{x}}}\, \Phi'(r_{\mathrm{x}}). \tag{A.5}$$

This is the same boundary condition as is usually encountered in the uncrystallized case for r approaching zero (e.g., see Unno et al. 1989); we see that it is unchanged by the presence of a rigid, crystallized core.

5. Global Conservation of Momentum for $\ell = 1$ Modes

As a note, we mention that the derivation by (1976) that $\ell = 1$ modes conserve the total momentum of the system and are therefore allowable pulsation modes is easily extended to the present case, in which we have a solid, completely rigid core, which is surrounded by a fluid envelope in which there are pulsations.

In the present case, the center of mass of the fluid in the envelope *is* displaced by the pulsations. However, the pressure variations associated with these pulsations in the fluid exert a net force on the crystalline core, causing its center of mass to also move. Considered as a system, the core plus envelope conserves momentum, so that there is no net displacement of the center of mass, and $\ell = 1$ oscillations are again allowed.

Appendix B

Mode Trapping in the Asymptotic Limit

In the asymptotic limit of high k, g-modes in white dwarfs are evenly spaced in period. This is a consequence of the following statement: in the asymptotic limit, g-modes with different k's sample the various regions of a model in the same way. If we turn this statement around, we have the following: g-modes with different k's which *do not* sample the various regions of a given model in the same way will in general not be evenly spaced. This is essentially mode trapping in a nutshell, and it is the viewpoint which we shall exploit in our derivation.

We will need expressions for the eigenfunctions ξ_r and ξ_h in the asymptotic (low-frequency) limit for g-modes for the region in which they are propagating; we take these from Unno et al. (1989):

$$\begin{aligned}\xi_r &= \frac{1}{\rho^{1/2} c_s r}\left|1 - L_\ell^2/\sigma_k^2\right|^{1/2} \frac{a(-1)^{k+1}}{\sqrt{\pi k_r}} \sin\left(\int_r^{r2} k_r dr - \frac{\pi}{4}\right) \\ &= a(-1)^{k+1}[\ell(\ell+1)]^{1/4}\left(\pi\rho r^3 \sigma_k N\right)^{-1/2} \sin\left(\int_r^{r2} k_r dr - \frac{\pi}{4}\right), \quad \text{(B.1)}\end{aligned}$$

$$\begin{aligned}\xi_h &= \frac{1}{\rho^{1/2} r^2 \sigma_k^2}\left|N^2 - \sigma_k^2\right|^{1/2} \frac{a(-1)^{k}}{\sqrt{\pi k_r}} \cos\left(\int_r^{r2} k_r dr - \frac{\pi}{4}\right) \\ &= a(-1)^{k}[\ell(\ell+1)]^{-1/4}\left(\frac{N}{\pi\rho r^3 \sigma_k^3}\right)^{1/2} \cos\left(\int_r^{r2} k_r dr - \frac{\pi}{4}\right), \quad \text{(B.2)}\end{aligned}$$

where these expressions are valid in the region $r1 < r < r2$, where $r1$ and $r2$ are the inner and outer turning points of the g-mode cavity, and a is an overall normalization constant.

We wish to write the frequency weighting function for a mode, as given in Kawaler, Winget, & Hansen (1985), but in the form given in Unno et al. (1989, equation 14.19). The frequency (in the Cowling approximation) is given by

$$\sigma_k^2 = \frac{1}{I}\int_0^R drr^2 \left(\frac{1}{\rho c_s^2}p'^2 + N^2\rho\xi_r^2\right), \tag{B.3}$$

where

$$I = \int_0^R drr^2\rho\left(\xi_r^2 + \ell(\ell+1)\xi_h^2\right).$$

We imagine that in our model, N^2 is smooth enough so different overtones are able to sample it in the same way, and are therefore evenly spaced.

We now imagine perturbing N^2 in a local region by an amount δN^2, so that it acquires a "bump" which mimics the behavior of N^2 in a composition transition zone. Since this formulation for the eigenvalue σ^2 is equivalent to a variational principle, we find that

$$\delta\sigma_k^2 = \frac{1}{I}\int_0^R drr^2\rho\xi_r^2\delta N^2, \tag{B.4}$$

where the changes to σ^2 produced by the changes in the eigenfunctions are second order, by nature of the variational principle. We therefore will use the asymptotic eigenfunctions to evaluate equation B.4.

1. A Particular Model

For the sake of concreteness, we will assume that the transition zone we are trying to model is the hydrogen transition zone, which is at a radius of r_H. For simplicity's sake, we parameterize the bump in the Brunt-Väisälä frequency in this region by

$$\delta N^2 = 2N_0 N_1 \frac{1}{\sqrt{\pi} d_H} e^{-(r-r_H)^2/d_H^2}, \tag{B.5}$$

where N_0 is the "background" unperturbed Brunt-Väisälä frequency which smoothly connects to each side of the transition zone, d_H is a measure of the width of the transition zone, and N_1 measures the strength of the bump in N in units of cm-hz.

Since δN^2 is nonzero only in the immediate vicinity of r_H, we use the following approximate expression valid for $r \sim r_H$ in the argument of the sin function:

$$\begin{aligned} \int_r^{r2} k_r dr &= \int_{r_H}^{r2} k_r dr - \int_{r_H}^{r} k_r dr \\ &\approx \pi \frac{P_k}{\Pi_H} - k_r (r - r_H), \end{aligned}$$

where

$$\Pi_H \equiv \frac{2\pi^2}{\sqrt{\ell(\ell+1)}} \frac{1}{\int_{r_H}^{r2} N dr/r}.$$

With these relations and equations B.1 and B.2 for the eigenfunctions, equation B.4 becomes

$$\delta\sigma_k^2 = \frac{a^2}{I} \frac{2\sqrt{\ell(\ell+1)} N_1}{\sqrt{\pi}\sigma_k d_H} \int_{r1}^{r2} (dr/r) e^{-(r-r_H)^2/d_H^2} \sin^2\left[k_r(r - r_H) + \phi_P\right], \tag{B.6}$$

where

$$\phi_P \equiv \frac{\pi}{4} - \pi \frac{P_k}{\Pi_H}.$$

Since the integrand in B.6 decays rapidly away from the point r_H, we can replace the limits of integration $(r1, r2)$ with $(-\infty, +\infty)$, without adding significantly to the integral. If we now use the identity $\sin^2 y = (1 - \cos 2y)/2$, shift the integration in terms of the new variable $x \equiv r - r_H$, and approximate $1/r$ as $1/R_\star$, then equation B.6 becomes

$$\begin{aligned}
\delta\sigma_k^2 &= \frac{a^2}{I}\frac{\sqrt{\ell(\ell+1)}N_1}{\sqrt{\pi}\sigma_k d_H R_\star}\int_{-\infty}^{\infty} dx e^{-x^2/d_H^2}\left(1-\cos\left[2k_r x + 2\phi_P\right]\right) \\
&= \frac{a^2}{I}\frac{\sqrt{\ell(\ell+1)}N_1}{\sqrt{\pi}\sigma_k d_H R_\star}\sqrt{\pi}d_H\left(1+e^{-k_r^2 d_H^2}\cos 2\phi_P\right) \\
&= \frac{a^2}{I}\frac{\sqrt{\ell(\ell+1)}N_1}{\sigma_k R_\star}\left(1+e^{-k_r^2 d_H^2}\cos 2\phi_P\right), \qquad \text{(B.7)}
\end{aligned}$$

where we have used the tables of Gradshteyn & Ryzhik (1980) to perform the integration.

We now need to evaluate the integral I:

$$\begin{aligned}
I &= \int_{r1}^{r2} dr r^2 \rho\left(\xi_r^2 + \ell(\ell+1)\xi_h^2\right) \\
&\approx \ell(\ell+1)\int_0^{R_\star} dr r^2 \rho \xi_h^2 \\
&\approx a^2\frac{\sqrt{\ell(\ell+1)}}{\pi\sigma_k^3}\int_{r1}^{r2} dr\frac{N}{r}\cos^2\left(\int_r^{r2} k_r dr' - \frac{\pi}{4}\right), \\
&\approx a^2\frac{\sqrt{\ell(\ell+1)}}{2\pi\sigma_k^3}\int_{r1}^{r2} dr\frac{N}{r} \\
&\approx a^2\frac{k}{2\sigma_k^2},
\end{aligned}$$

where in the last step we have used the equation 3.21 for the asymptotic g-mode frequency. Putting this altogether, we arrive at the following expression:

$$\delta\sigma_k^2 = 2\sqrt{\ell(\ell+1)}\frac{\sigma_k N_1}{k R_\star}\left(1+e^{-k_r^2 d_H^2}\cos 2\phi_P\right),$$

so

$$\delta\sigma_k = \frac{\sqrt{\ell(\ell+1)}}{k}\frac{N_1}{R_\star}\left(1+e^{-k_r^2 d_H^2}\cos 2\phi_P\right), \qquad \text{(B.8)}$$

or, in terms of period this becomes

$$\delta P_k = -\frac{\sqrt{\ell(\ell+1)}}{2\pi k}\frac{N_1 P_k^2}{R_\star}\left(1+e^{-k_r^2 d_H^2}\sin(2\pi P_k/\Pi_H)\right), \qquad \text{(B.9)}$$

where we have substituted for ϕ_P in the above expression. Thus, this formula has a trapping period (period difference between trapped modes) of Π_H, which is the result found by Brassard et al. (1992).

We now make substitutions which are valid in the asymptotic limit. Since $k_r \propto 1/\sigma$ and $P_k \sim k\langle\Delta P\rangle$, we can write

$$\delta P_k = A\, k \left(1 + e^{-k^2(\langle\Delta P\rangle/P_H)^2} \sin(2\pi k\langle\Delta P\rangle/\Pi_H)\right), \tag{B.10}$$

where $\langle\Delta P\rangle$ is the average period spacing in the asymptotic limit, k is the radial overtone number, and P_H is defined as the period at which the radial wavelength equals the transition zone thickness, i.e., $k_r d_H = 1$ when $P = P_H$. The constant $A = -\sqrt{\ell(\ell+1)}N_1\langle\Delta P\rangle^2/(2\pi R_\star)$ determines the strength of the trapping.

The period spacing is given by

$$\begin{aligned} \Delta P_k &= P_{k+1} - P_k \\ &\approx \langle\Delta P\rangle + \delta P_{k+1} - \delta P_k \end{aligned}$$

We now choose values of these parameters for comparison with the plots in Brassard et al. (1992). Using $\langle\Delta P\rangle = 30$ sec, $\Pi_H = 200$ sec, and $P_H = 1000$ sec, and choosing $A = -2.5$ sec to set the amplitude of the trapping, we have the result shown in Figure B.1.

The most instructive feature of this figure is that it shows that in the high overtone limit, all the modes sample the bump in the Brunt-Väisälä frequency equally, so they all have a period spacing of $30 - 2.5 = 27.5$ sec. Thus, the finite thickness of the transition zone manifests itself in a decaying trapping amplitude as the period is increased, which is as expected. This effect is one

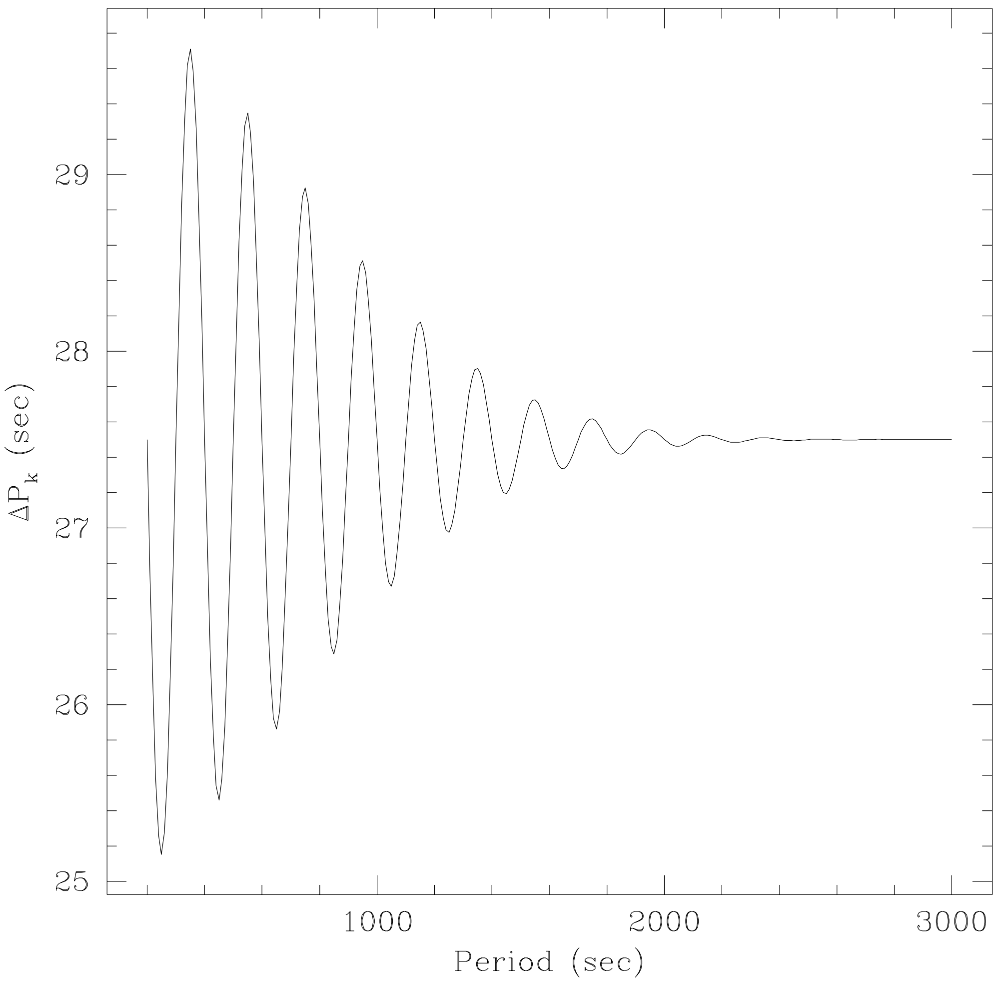

Fig. B.1.— The variation in ΔP_k as a continuous function of the period.

which could exist *in addition* to the effect calculated in Brassard et al.. In a way, it could be thought of as a transient solution.

It would be a simple matter to treat a second perturbation in the Brunt-Väisälä frequency which would take into account the different magnitudes of the Brunt-Väisälä frequency on each side of the transition zone. In this case we would simply take δN to be a constant positive value above the transition zone, and zero elsewhere. This would produce oscillatory behavior in ΔP_k which would not decay with period, with the full trapping behavior being the sum of this plus the transient effect. It would still have the drawback, however, of producing a purely sinusoidal shape to the mode trapping.

The shape of the trapping cycle does not reproduce the sharp bottom and flat top seen in the numerical or analytical models of Brassard et al. (1992). This is not surprising given the severity of our approximations. Since the modes are taken to be in the asymptotic limit, nearby overtones differ mainly in the phase with which they enter the transition zone. Since this phase varies between zero and 2π, we find that ΔP_k appears to vary sinusoidally and therefore symmetrically, and does not exhibit the sharp bottom behavior seen in the numerical models. Thus, the main use of this derivation is for instructive purposes.

I still cannot help but think that it is the bump/spike in the Brunt-Väisälä frequency and not the fact that it has a different baseline value on each side of the transition zone which is the dominant effect in producing mode trapping. If I could treat the problem of a given asymptotic mode being reflected and transmitted by its encounter with the spike, I could obtain formulae relating the amplitudes above and below this region. The period of the mode would then be a weighted average of the $\int N dr/r$ in the two regions, scaled by the square of the amplitude of the mode on each side of the transition zone.

2. A More General Result

The perturbation to the square of the Brunt-Väisälä frequency due to a two-element transition zone is

$$\begin{aligned} \delta N^2 &= \frac{gV}{r}\left(\frac{\partial \ln \rho}{\partial \ln X_1}\right)_{T,p} \frac{d \ln X_1}{d \ln p} \\ &= -g\left(\frac{\partial \ln \rho}{\partial X_1}\right)_{T,p} \frac{dX_1}{dr}, \end{aligned} \tag{B.11}$$

where $V \equiv -d\ln p/d\ln r$, and X_1 is the mass fraction of element one. If we insert this expression into equation B.4, then we obtain

$$\begin{aligned} \delta\sigma_k^2 &= -\frac{1}{I}\int_0^R dr r^2 \rho \xi_r^2 g \left(\frac{\partial \ln \rho}{\partial X_1}\right)_{T,p} \frac{dX_1}{dr} \\ &\approx -2\frac{\sqrt{\ell(\ell+1)}}{k\pi}\frac{g\sigma_k}{R_\star N_0}\int_0^{R_\star} dr \left(\frac{\partial \ln \rho}{\partial X_1}\right)_{T,p} \frac{dX_1}{dr}, \end{aligned} \tag{B.12}$$

or, rewriting in terms of period,

$$\delta P_k = \frac{k\sqrt{\ell(\ell+1)}}{2\pi^2}\frac{g\langle\Delta P\rangle^2}{R_\star N_0}\int_0^{R_\star} dr \left(\frac{\partial \ln \rho}{\partial X_1}\right)_{T,p} \frac{dX_1}{dr}, \tag{B.13}$$

where N_0 is value of the Brunt-Väisälä frequency throughout the transition computed with the Schwarzschild criterion. In terms of our work in the previous section, we have calculated the constant A, which is the net change in to the mean:

$$A = \frac{\sqrt{\ell(\ell+1)}}{2\pi^2}\frac{g\langle\Delta P\rangle^2}{R_\star N_0}\int_0^{R_\star} dr \left(\frac{\partial \ln \rho}{\partial X_1}\right)_{T,p} \frac{dX_1}{dr}. \tag{B.14}$$

It is possible to perform a closed form integration of the integrand in B.14 for many cases of interest. Thus, we do not need to know the exact shape of the profile to calculate its effect on the mean period spacing in the asymptotic limit. In fact, in the limit of very thin transition zone, P and T do not change appreciably from the top to the bottom of the zone (since they must be continuous), so the integrand is an exact differential, and we may integrate to find that

$$A = \frac{\sqrt{\ell(\ell+1)}}{2\pi^2} \, \frac{g\langle \Delta P \rangle^2}{R_\star N_0} \ln \frac{\rho(+)}{\rho(-)}, \tag{B.15}$$

where $\rho(+)$ and $\rho(-)$ are the densities immediately above and below the transition zone, respectively. We note that A will be negative since $\rho(+) < \rho(-)$.

We now return to finite thickness transition zones. In some regions of interest, we may approximate the pressure as due to a gas of completely degenerate electrons plus an ideal (non-degenerate) gas of ions. In this limit, we find that

$$\left(\frac{\partial \ln \rho}{\partial X_1}\right)_{T,p} = \begin{cases} -kT/(32 m_p c_s^2) & \text{O/C transition zone} \\ -kT/(4 m_p c_s^2) & \text{C/He transition zone} \end{cases}, \tag{B.16}$$

where T and c_s^2 are the temperature and sound speed in the transition zone, X_1 is the mass fraction of the lighter element, and m_p is the mass of the proton. Since this expression is independent of X_1, and c_s and T vary relatively slowly through the transition zone, it is approximately constant, so we may take it outside the integral in equation B.14. The remaining integrand is

$$\begin{aligned} \int dr \frac{dX_1}{dr} &= X_1(+) - X_1(-) \\ &= 1 - 0 \\ &= 1, \end{aligned}$$

where $X_1(+)$ and $X_1(-)$ are the abundances of the lighter element above and below the transition zone, respectively.

If we consider the ideal gas EOS for the case of the He/H transition zone, then we have

$$\rho \propto \frac{P}{T(3 + 5X_H)},$$

where X_H is the hydrogen mass fraction. This leads to

$$\int dr \frac{dX_1}{dr} \left(\frac{\partial \ln \rho}{\partial X_1} \right)_{T,p} = -\ln \frac{8}{3}. \tag{B.17}$$

For the case of both a degenerate and an ideal gas EOS, we find that the fractional increase in the period spacing obeys the following relation:

$$\begin{aligned} \frac{\delta \langle \Delta P \rangle}{\langle \Delta P \rangle} &= \frac{A}{\langle \Delta P \rangle} \\ &\propto \frac{g \Pi_0}{R_\star N_0} \frac{T}{c_s^2}, \end{aligned} \tag{B.18}$$

where $\Pi_0 \equiv \sqrt{\ell(\ell+1)} \langle \Delta P \rangle$ is an ℓ-independent function of the Brunt-Väisälä frequency. In an ideal gas, $c_s^2 \propto T$, so the explicit temperature dependence vanishes. Of course, the mean period spacing and the Brunt-Väisälä frequency are both implicit functions of T.

Appendix C

A Possible Shear Instability

In the context of pulsating stars, the word "instability" usually refers to whether a particular mode is being driven or damped; if it is being driven more than it is being damped, we say that the mode is overstable or unstable. When we are looking at fluid motions and we are examining the stability of local fluid elements with respect to vertical, adiabatic displacements, an instability corresponds to a negative Brunt-Väisälä frequency and therefore convection. Many additional instabilities are possible within a fluid which has a nonzero velocity field.

One instability in particular may be of interest for white dwarf pulsations. We have seen in Chapter 3 that g-modes in our white dwarf models exhibit a large amount of shear, i.e.,

$$\frac{d\xi_h}{dr} \approx \frac{\xi_h}{H_P} \gg \frac{\xi_h}{R_\star},$$

where H_P is a pressure scale height. The Richardson number Ri gives us a way of estimating the amount of shear which a stratified fluid can withstand before it becomes unstable and mixes vertically. From Shu (1992), we have

$$\text{Ri} \equiv \frac{-g(\partial\rho/\partial s)_P(ds/dr)}{\rho(dv_h/dr)^2} \tag{C.1}$$

$$= \frac{N^2}{(dv_h/dr)^2}, \tag{C.2}$$

where v_h is the velocity in the horizontal direction and N^2 is the Brunt-Väisälä frequency. The condition for stable flow is

$$\text{Ri} > \frac{1}{4}, \tag{C.3}$$

so instabilities may result if Ri is less than this value locally.

If we specialize to the case where the fluid motions are due to one mode which has $m = 0$, then we have from the definition of the displacement

$$\vec{v}_h = \text{Re}\left(\frac{d\vec{\xi}_h}{dt}\right) \tag{C.4}$$

$$= \text{Re}\left(i\sigma\, e^{i\sigma t}\,\frac{d}{d\theta}Y_\ell^0(\theta,\phi)\ \xi_h(r)\right)\hat{\theta} \tag{C.5}$$

$$= -\sigma\ \sin\sigma t\,\frac{d}{d\theta}Y_\ell^0(\theta,\phi)\ \xi_h(r)\ \hat{\theta}. \tag{C.6}$$

Computing the magnitude of the velocity shear, we find that

$$\frac{dv_h}{dr} = -\sigma\ \sin\sigma t\,\frac{d}{d\theta}Y_\ell^0(\theta,\phi)\frac{d\xi_h}{dr}. \tag{C.7}$$

The important thing to notice about this expression, is that it has both a time dependence and an angular dependence, in addition to the radial dependence in $d\xi_h/dr$. Thus, if there is a finite shear threshold which a given mode is exceeding, it will do so only at certain times and in certain angular regions of our models.

We concentrate now on the magnitude of $\sigma d\xi_h/dr$, since the other terms are of order unity; this will let us know if the shear is large enough for us to concern ourselves with this effect. Thus, we compute

$$\mathrm{Ri} = \frac{N^2}{\sigma^2 (d\xi_h/dr)^2} \tag{C.8}$$

as a function of r throughout our model for a given mode. In our codes, the eigenfunctions are normalized such that $\xi_r/R_\star = 1$ at the surface of our models. In reality, the amplitudes are much smaller. Robinson, Kepler, & Nather (1982) found that the actual range of $\xi_r/R_\star$ was from 10^{-4} to 10^{-5}. Here we adopt the value of 10^{-4}, so we scale ξ_h by this factor in our calculations.

Figure C.1 shows the results for a 672 sec, $\ell = 1$ mode in a 0.6 $\mathrm{M}_\odot$ model with $T_{\rm eff} = 12,000$ K. The horizontal dotted line corresponds to $\mathrm{Ri} = \frac{1}{4}$; the region above this line is stable to a shear instability and the region below it is unstable. The region to the right of $x = 12.5$ is the convection zone, which is already being mixed by a fluid instability, where $x \equiv -\log(1 - M_r/M_*)$. The region between 11.1 and 12.5 is the region which may be susceptible to the shear instability. Remembering the additional dependencies of the shear in equation C.7, we see that this unstable region is actually a function both of the phase of the oscillation cycle σt and the angular position $(\theta,\, \phi)$ in the model.

A possible effect of this instability is to alter the driving of the oscillations. When the instability operates, the offending fluid layers will be mixed in a turbulent manner similar to the mixing which occurs in a convection zone. This will change the way in which these layers either drive or damp the oscillations.

In the models we have examined, the shear-unstable region is directly

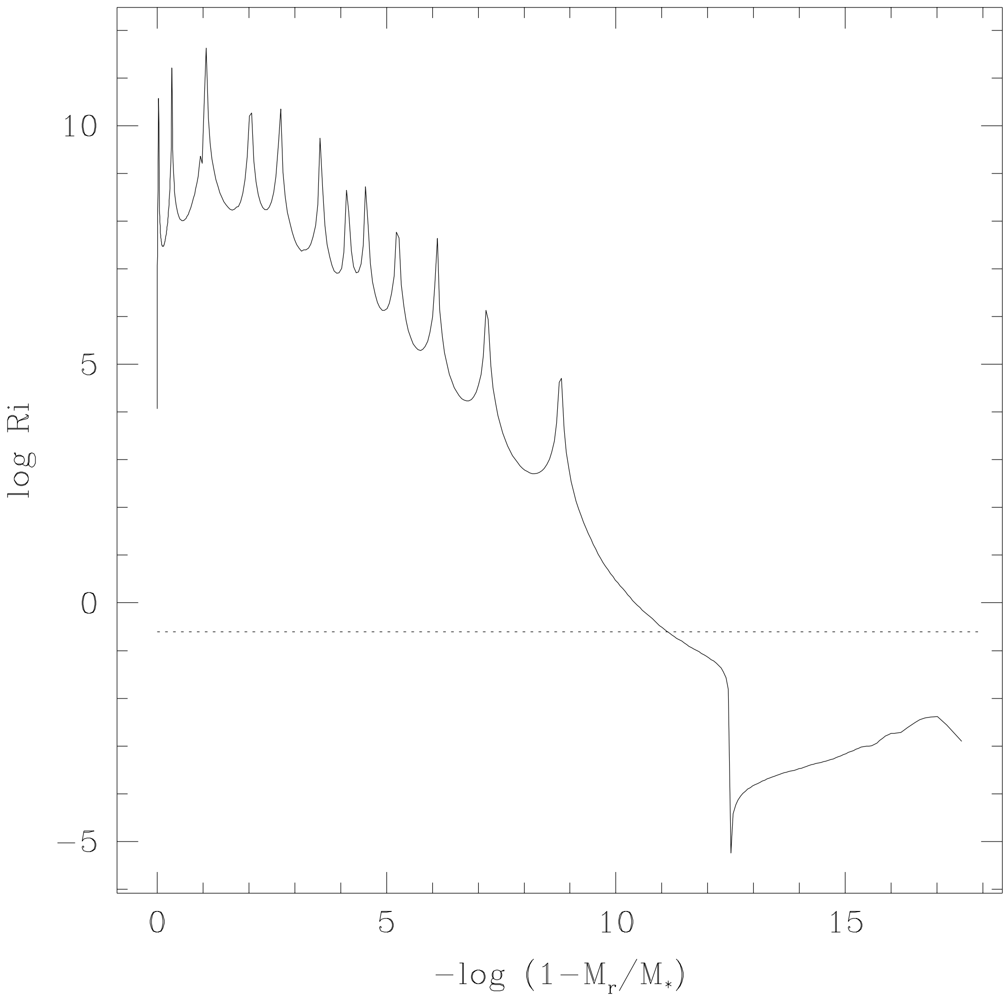

Fig. C.1.— The Richardson number for a 672 sec, $\ell = 1$ mode in a 0.6 $M_\odot$ model with $T_{\rm eff} = 12,000$ K. The horizontal dotted line corresponds to $\mathrm{Ri} = \frac{1}{4}$; the region above this line is stable to a shear instability and the region below it is unstable.

below the convection region. When the instability is operating, it may be useful to think of the convection zone as extending downward into this region, since the turbulent mixing in the shear layers mimics the turbulent mixing which is occurring in the convection zone itself. Restating this, we can say that the mode generates a "self-viscosity" which is time-dependent and which acts to mix this region. Since this effect should have an angular as well as a time dependence, we can imagine a situation in which the mode has a luminosity variation at the surface which is basically a spherical harmonic, but which is clipped (or reduced) in the high amplitude regions. This will generate spatial harmonics (a mixture of spherical harmonics) as well as temporal harmonics.

The situation in which several modes are simultaneously present offers many more interesting possibilities. In this case, the fluid motions do not slowly bump the shear threshold as in the case of a single mode slowly growing in amplitude. Rather, two different modes can suddenly coherently add in a region and exceed the threshold. These modes "crash" against each other, dissipating their local kinetic energies. This would seem to be an amplitude limiting mechanism. Interestingly, even relatively small amplitude modes could dissipate their energy in this way by "piggy-backing" on top of a large amplitude mode. Thus, a single large-amplitude mode could regulate the amplitudes of most or all of the other excited modes.

While Figure C.1 shows that this is at least a superficially plausible idea, we stress that this is only a possible mechanism, and may not be relevant for actual pulsating white dwarf stars. A detailed investigation would be required to determine the exact phenomenology associated with this mechanism.

Appendix D

The Detectability of p-modes

It is an agreed-upon "fact" that the cause of most of the observed pulsations in white dwarf stars is due to g-mode pulsations. In white dwarf models, g-modes are "envelope" modes, and p-modes are "core" modes. That is, the g-modes have more of their kinetic energy concentrated toward the surface than do the p-modes. Thus, we would expect to see g-mode oscillations much more readily than p-mode oscillations, even if there were an identical amount of kinetic energy in both sets of modes. Observationally, p-modes would be difficult to detect since the short timescale variability which they produce can be mimicked and masked by the short term variability of the Earth's atmosphere.

Ignoring the large observational difficulties and conventional wisdom, we ask whether it is plausible for p-modes to exist in white dwarfs at "observable" amplitudes. In the asymptotic limit, the period/frequency weight function is a tracer for the kinetic energy of a mode. In Figure D.1, we plot the weight functions for p- and g-modes for a 0.6 $M_\odot$ DAV model ($T_{\rm eff} = 12,000$ K). We see that the p-mode periods are formed much deeper those of the g-modes. We would therefore not expect the p-modes to be easily observable.

If Figure D.2, we plot the same quantities but for a DBV model. Since this is a hotter model ($T_{\rm eff} = 25,000$ K), it is less degenerate in its interior, so

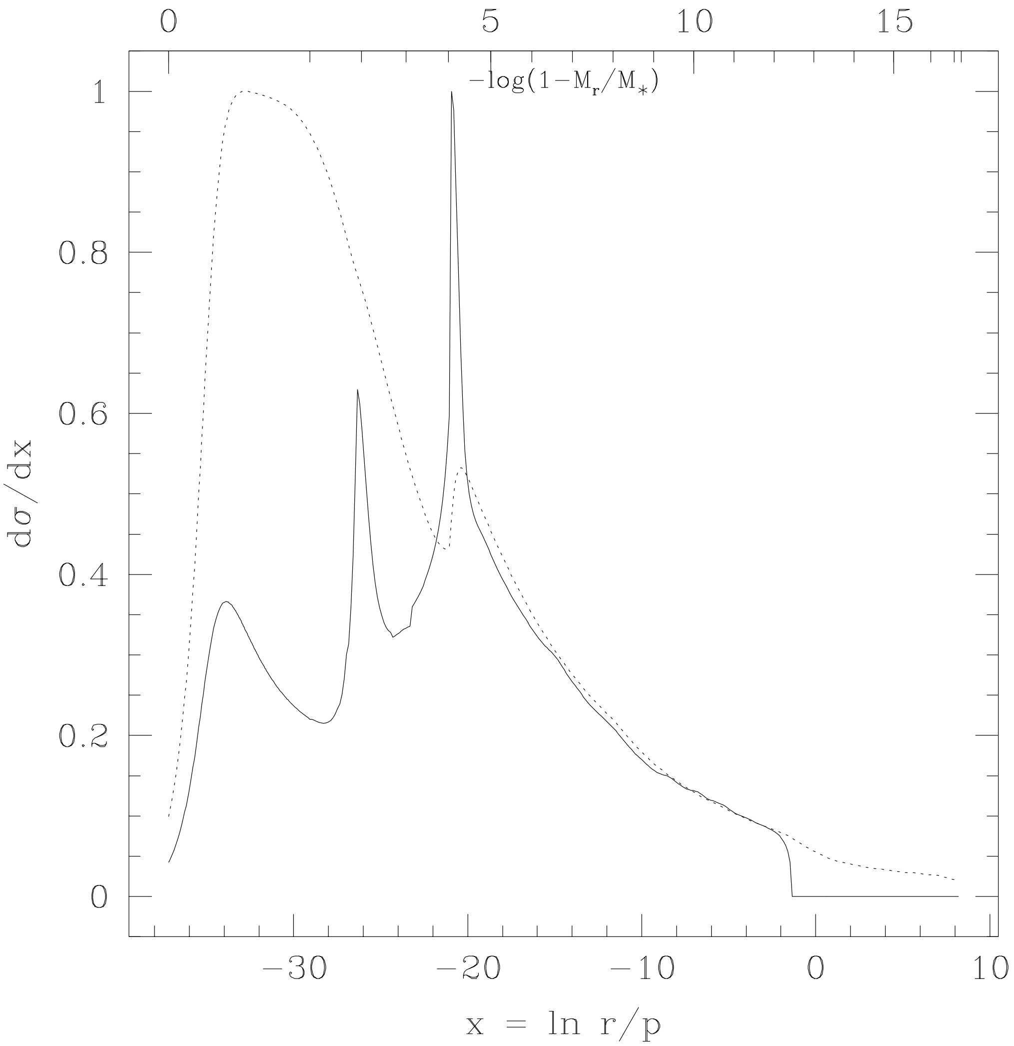

Fig. D.1.— A comparison of the weight functions for *p*-modes (dotted line) and *g*-modes (solid line).

the Brunt-Väisälä frequency is larger in its core. The result is that the g-modes appear to be formed deeper in the model and sample the star in roughly the same manner as the p-modes. This leads us to believe that if the p-modes have roughly the same kinetic energies as the g-modes, then these modes may have observable amplitudes at the surface.

In Table D.1, we have tabulated the results of a nonadiabatic calculation. For this calculation, we scaled the value of the luminosity perturbation at the surface, y_6, so that all the modes have 10^{33} ergs of kinetic energy. We then compared this scaled y_6 for several different g- and p-modes; the modes below the solid line are p-modes, which can be seen from their short periods (< 1 sec). This table shows us that the high overtone p-modes should be just as "observable" as the g-modes. This calculation is made ignoring perturbations to the convective flux, so the value of y_6 at the surface could be quite different than that computed here. Furthermore, we caution that this argument says nothing about the different driving mechanisms for the two classes of modes, so there may be other reasons for p-modes to not be present in white dwarf stars.

In Table D.2, we show the same results for the cooler DAV model. We see again that the p-modes appear to be as detectable as the g-modes, according to the criteria used above. It would apppear that the issue of the visibility of these modes comes down to one of driving. Since the p-modes have much shorter periods, they must be driven in regions of the star which have much shorter thermal timescales. This means they must be driven closer to the surface than the g-modes are, in layers which have much less thermal energy to pump into the pulsation modes. If we assume that the energy available to

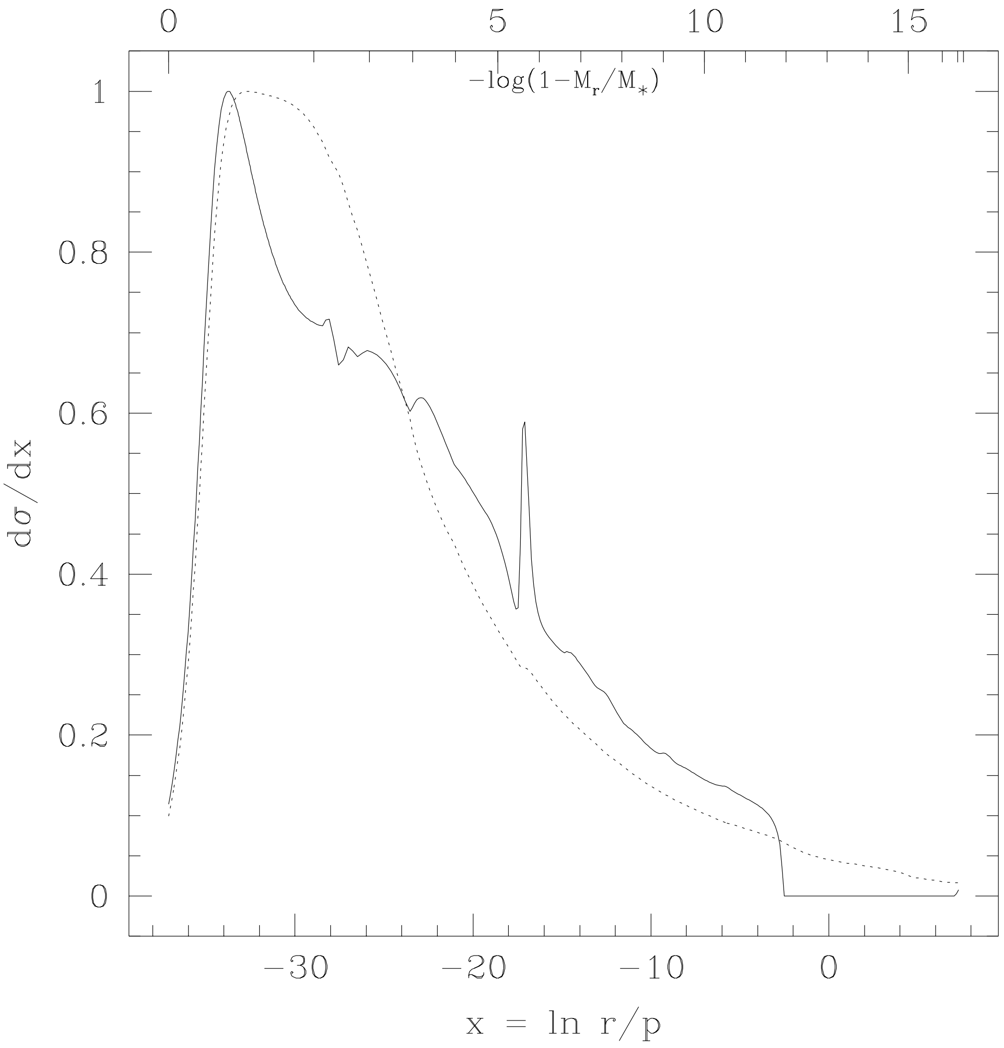

Fig. D.2.— A comparison of the weight functions for p-modes (dotted line) and g-modes (solid line).

Table D.1. Normalized y_6 for p- and g-modes in a DBV model

ℓ	k	Period (s)	y_6
1	12	577.66	0.0011
1	13	620.00	0.0005
1	14	664.55	0.0011
1	15	705.74	0.0054
1	16	740.08	0.0130
1	17	779.56	0.0182
1	17	0.753	0.0009
1	22	0.592	0.0029
1	26	0.505	0.0062
1	33	0.398	0.0154
1	43	0.302	0.0337
1	62	0.199	0.1342

Table D.2. Normalized y_6 for p- and g-modes in a DAV model

ℓ	k	Period (s)	y_6
1	10	583.316	0.0105
1	11	641.665	0.0147
1	12	672.327	0.0157
1	13	721.105	0.0250
1	14	764.813	0.0269
1	20	0.710	0.0040
1	24	0.601	0.0084
1	29	0.503	0.0164
1	37	0.398	0.0331
1	49	0.300	0.0648

drive the modes scales like the mass of the driving region, then there should be 2 to 3 orders of magnitude less energy available for the p-modes, which would reduce their surface luminosity perturbations by at least a factor of 10 compared to the g-modes. In addition, the p-mode periods are of the same order as the convective turnover time for fluid elements in the convection zones of the white dwarf models, so significant and difficult to describe interactions may occur between the convection zone and the p-modes. This might result in either damping or driving of the p-modes.

Finally, in analogy with the Sun, we might expect the convection zones of white dwarfs to stochastically excite p-mode oscillations. In other words, the intrinsic "noise" associated with the fluid motions of the convection zones could dynamically excite p-modes in white dwarfs. The amplitudes of these modes would then decay with time after a number of cycles. However, as with the Sun, we would expect these modes to have very large values of ℓ and therefore have unobservably small amplitudes when integrated over the disk of the star.

Appendix E

Computer Codes

1. Modifications to WDEC—Matt's Version

1.1. Description of Changes

The modifications to include phase separation in Matt's version of the white dwarf evolution code (WDEC) were begun by Eric Klumpe and detailed in his Master's thesis (Klumpe 1995). These included the generation of a new subroutine, `phasep.f`, which calculated the change in chemical composition of the white dwarf core as it crystallized and adjusted the composition of the remaining fluid layers to reflect this chemical change. Klumpe used the phase diagram of Barrat, Hansen, & Mochkovitch (1998) to compute the composition changes. In this present treatment, we use phase diagrams by Segretain & Chabrier (1993) and Ichimaru, Iyetomi, & Ogata (1988).

The above changes address the new mechanical structure of the star after phase separation, but do not address the energetics. By performing the above manipulations. i.e., recalculating the array which contains the compositional profile of the model, we are in effect making the following assumption: the material is able to rearrange itself on timescales which are short compared to the evolutionary timesteps, and this process generates *no corresponding release* *of energy.* In order to self-consistently enforce conservation of energy, we must include an additional energy source which is present during phase separation.

We have used the formalism set out in Isern et al. (1997) and Chabrier (1997) to calculate this release of energy. It was included in the evolution code as a negative neutrino luminosity, with two wrongs for once making a right. A summary of the changes made to the evolution code is given in below, listed by the subroutine in which the modification was made.

calc.f Added the common block `common/density/dens(400),cv1(400)` to store values for the density and heat capacity. This allows calls to be made in phasep2.f directly to the Lamb IEOS code, which takes temperature and density as inputs.

end.f Added calls to xbndry2.f, phasep2.f, and ephase.f. The movement of the crystallization front and the associated release of phase separation energy is taken into account with each iteration of the model, so that the degree of crystallization can dynamically adjust to the release of ps energy.

ephase.f A new subroutine which calculates the total phase separation energy released during a timestep using calls to ieos.f, the Lamb equation of state Code.

gray.f Added a test so that code exits for a $T_{\rm eff} < T_{\rm min} (= 2100$ K). This prevents the code from hanging for $T_{\rm eff} < 2000$ K, so more files can be batch processed.

istatco.f Added in phase separation energy through enxtal2(400), and its derivatives, dphdt and dphdt, all of which are stored in `common/xenergy2`.

We include the phase separation energy as a negative neutrino luminosity.

opacsubs.f Moved and split the common block `common/crystal` to the function opac. The code now correctly implements the opacity limiting defined by the input parameter oradlimit.

openem.f Now opens additional files: `phase_energy.dat`, `phase_energy2.dat`, and `profile.dat` These files are used to store information relating to crystallization and phase separation.

phasep2.f A major modification of Klumpe's phasep.f. Calculates the the new C/O profile as well as the energy released due to phase separation. Also includes the latent heat of crystallization of the last partially crystallized shell, to enable the code to converge more easily.

read2.f Now writes output to file `phase_energy2.dat`. This output includes phase separation information, as well as the luminosity function.

wdxd.f Moved read statement for crystallization and convection control flags from read2.f to wdxd.f. The variable oradlimit is now safely defined before it is used in the opacity calls in read1.f.

xbndry.f Made changes to keep jx from exceeding jb-1, and limit amxc to be equal to the stop mass at complete crystallization. Also set iphasepflag = 0 if completely crystallized. Turns off phase separation routines if core is completely crystallized (iphasepflag=0).

xbndry2.f An altered copy of xbndry.f. It computes amxc, damxcdt, and damxcdp with each iteration of calc.f through the core. damxcdt and damxcdp are the change in $M_{\rm xtal}$ with temperature and pressure, respectively. These are needed for the derivatives of the phase separation energy with respect to these variables.

In addition to changing the evolution code itself, I have altered slightly the format of the header for the input evolutionary models. The line in the input file where the switches controlling crystallization and convection are read was moved so that it now comes directly after the switches for the convective mixing length. This allows the opacity limiting parameter, `oradlimit`, to be defined before it is used in the opacity calls in `read1.f`.

In the following I give the code for the two new routines ephase.f and phasep2.f, which are the most important for calculating the energy released by phase separation and the changing C/O profiles.

1.2. Source Code

```
c
c ******************************************************************************
c  This is a modification by MHM (October/November 1997) of phasep by
c  EWK. On the first call, it calculates the composition profile as a
c  function of the crystallized mass-fraction, and then it calculates
c  the energy released due to this phase separation, also as a function
c  of crystallized mass fraction. On subsequent calls, it uses the
c  current crystallized mass-fraction as computed in xbndry2 to do a
c  spline interpolation for the energy released, and it distributes this
c  energy in such a way that the fractional temperature perturbation
c  (dT/T) should be constant. The composition redistribution algorithm
c  is now able to deal  with nonuniform initial distributions of xc (and
c  xo), although it really only makes physical sense for initial
c  distributions in which xo does not increase with increasing mass.
c  This is because the criterion for mixing the interior fluid layers
c  with an overlying fluid layer is that the result of the mixing is to
c  decrease the carbon content of the innermost fluid layers, so that
c  there is a net movement of carbon outwards, and oxygen inwards. Once
c  a range of shells are considered mixed, the composition is set to be
c  uniform within them. As a final tweak, along with the phase-separation
c  energy I include the latent heat contribution of the partially
c  crystallized shell, i.e., if the 51st shell is 20% crystallized, then
c  I add in 20% of the energy that would be released if it were crystallized,
c  with most of this energy being deposited with a gaussian distribution
c  peaked at the 51st shell (actually, it's centered on the crystallized
c  mass-fraction and interpolated onto the mass grid). Needless to say, this
c  greatly helps convergence since it helps prevent oscillations in the
c  the crystallized mass-fraction. In order to avoid adding a net amount
c  of energy via this procedure, however, a constant baseline is subtracted
c  from this distribution so that no net energy is introduced into the
c  system.
c******************************************************************************
c  This subroutine was added by EWK on July 25, 1995.  Once a shell is
c  crystallized this subroutine will take the C/O abundances of the
c  fluid phase and compute the C/O abundance of the corresponding solid
c  phase using a phase diagram (phzdia.dat for example).  This
c  subroutine will then compute the oxygen depletion and the carbon
c  enhancement for the remaining fluid layers and redistribute these
c  changes throughout the fluid layers in a homogeneous fashion.
c******************************************************************************
c
```

```
      subroutine phasep2
      implicit double precision (a-h, o-z)
      common/shells/ sa(400),ra(400),ba(400),pa(400),ta(400),
     1 ea(400),xca(400),fca(400),s(400),r(400),b(400),
     2 p(400),t(400),e(400),xc(400),sk(400),
     3 rk(400),bk(400),pk(400),tk(400)
      common/contrl/ds,g,sm,wc,it,nite,ja,jb,j,k,l
      common/xbnd/amxc,amxo,gold
      common/crystal/jxlast,jx,firstcall,iphasepflag,
     1               ixtalyes,iconvyes
      common/crystal2/xcinit(400),oradlimit
c       common/compold/xcold(400),xcn(400)
      common/density/dens(400),cv(400)
      common/phasecalc/iphcalc
      common/xenergy2/phengy(400),dphdt(0:400),dphdp(0:400),totph(400),
     1  enxtal2(0:400),dphdm(400),damxdt,damxdp
      common/epflag/epflag1
      common/debug/debug
      common/temp3/temp3(2,12)
      common/jxhist/jxold
c       common/amxchist/amxcold,amxcvold
      common/amxchist/amxcold
c       common/dsave/xx,yy,yy2,sprof,lprof,sprof2,lprof2,dmass
      common/dsave/xx,yy,yy2,xcp,dmass,massx,massf
      common/startx/istartxtal
      common/xcxtal/xcxtal(400),enxtal2a(400),fnxtal
      common/xistat/en2spline(400),xmass(400),en2dd(400)
      common/nxistat/nxsp
      common/blum/bl,bla
      common/once2/once2
      logical debug,once2
      dimension fluid(400), solid (400)
c       common/prep/ aa(19,800),ecv(400),ext(400),exr(400),iprep
      double precision cprof(400),xcprof(0:400,400),
     1  phengy,dmass(400),dudx(400),dphdm,norm,damxdt,damxdp,erelease,
     2  xx(400),yy(400),yy2(400),xcomp,massx(400),massf(400),xcp(400,400),
     3  profile1(400),profile2(400),p1(400),p2(400)


      if (istartxtal.eq.0) then
        if (jx.gt.0) then
          istartxtal=1
        else
          return
```

```
        endif
      endif

c      iphcalc = 1
      jxnew = jb-1
      debug = .false.
      if (epflag1.eq.0) then
        once2 = .false.
        epflag1 = 1
      endif
      fnat = log10(exp(1.0))
      iazeo=0
      star=10**sm
      pi=3.141592635
      totmass=0.0

      if (iphcalc.eq.1) go to 500

      iphcalc = 1
      open(66,file='phase3.dat',status='unknown')
      write(*,199)
      amxcvold=0.0
      amxcold=0.0
199   format('Entering phasep2: calculating phase separation energy'/,x,
     1 'as a function of crystallized mass fraction')
c
c  Compute the composition changes for the shells that have just crystallized.
c
      do 50 ijk = 1, 400
c        xc(ijk) = xcinit(ijk)
        xcinit(ijk) = xc(ijk)
        cprof(ijk) = xcinit(ijk)
        xcprof(0,ijk) = xcinit(ijk)
50    continue
c
      do 300 ixtal = 1, jxnew
c
c  Compute the mass of the shell that is crystallizing
c
      shellmass = 10.**s(ixtal+1) - 10.**s(ixtal)
c      shellmass = (aa(2,ixtal+1)-aa(2,ixtal))/star
c      shellmassc = xc(ixtal)*shellmass
      shellmassc = cprof(ixtal)*shellmass
      shellmasso = shellmass - shellmassc
```

```
c
c  Input the phase diagram
c  iphasepflag=1 for Segretain and Chabrier 1993, A & A, 271, L13
c  iphasepflag=2 for Ichimaru, Iyetomi, and Ogata 1988, 334, L17
      if (iphasepflag.eq.1) then
c        open(60, file = 'phzdia.dat', status = 'old')
        open(60, file = 'phzSeg.dat', status = 'old')
      elseif (iphasepflag.eq.2) then
        open(60, file = 'phzIch.dat', status = 'old')
      endif
      read (60, *) fluid(1), solid(1)
      read (60, *) fluid(2), solid(2)
      i = 2
c  100 if (fluid(i) .lt. xc(ixtal)) then
  100 if (fluid(i) .lt. cprof(ixtal)) then
        i = i + 1
        read (60, *) fluid(i), solid(i)
        goto 100
      endif
      close (60)
c
c  Compute the new carbon mass-fraction
c
c       xcnew = (solid(i)-solid(i-1))*(xc(ixtal)-fluid(i-1))/
c      1        (fluid(i)-fluid(i-1)) + solid(i-1)
      xcnew = (solid(i)-solid(i-1))*(cprof(ixtal)-fluid(i-1))/
     1        (fluid(i)-fluid(i-1)) + solid(i-1)
c put in a kludge to account for mixing with an azeotropic phase diagram
      if (xcnew.gt.cprof(ixtal) .and. iazeo.eq.0) then
        iazeo=1
        dx1=solid(i-1)-fluid(i-1)
        dx2=solid(i)-fluid(i)
        xazeo=(dx2*fluid(i-1)-dx1*fluid(i))/(dx2-dx1)
        write(*,*) 'azeotropic concentration =',xazeo
      endif
      if (iazeo.eq.1) then
        fluidmass  = 0.0
        fluidmassc = 0.0
        do ii=ixtal+2,jb
          dfluidmass = 10**s(ii) - 10.**s(ii-1)
          dfluidmassc= cprof(ii-1)*dfluidmass
          fluidmass = fluidmass + dfluidmass
          fluidmassc= fluidmassc+ dfluidmassc
          fluidmasso = fluidmass - fluidmassc
```

```
          enddo
          shellmassonew = (1.-xcnew)*shellmass
          xazeored=1.-fluidmasso/shellmass
c          write(*,*) ixtal,xazeored
          if (xazeored.gt.xazeo) then
            xcnew=xazeored
          else
            xcnew=xazeo
          endif
        endif
c
c  Compute the new mass-fractions for the fluid layers.  Recall that
c  crystallization reduces the carbon content and enhances the oxygen
c  content of the crystallizing layer.  Because the star is supported by
c  degenerate electron pressure, the positively charged ions go along
c  for the ride and distribute themselves in a way that maintains charge
c  neutrality.  Therefore, for every 8 carbon nuclei (Z = 6, or a total
c  charge of +48) that leave the crystallizing layer 6 oxygen nuclei (Z
c  = 8, or a total charge of +48) replace them.  Because the mass ratios
c  are very similar there is no change in the mass due to
c  crystallization.  (Actually, the mass remains unchanged only to
c  first-order.  The Coulomb interactions can either soften or stiffen
c  the equation of state and this is what links phase separation to the
c  release of gravitational potential energy.)
c
c
        shellmasscnew = xcnew*shellmass
        shellmassonew = shellmass - shellmasscnew
        deltamass = shellmassc - shellmasscnew
c
c        fluidmass = 1. - 10.**s(ixtal+1)
        fluidmass  = 0.0
        fluidmassc = 0.0
        do ii=ixtal+2,jb
         dfluidmass = 10**s(ii) - 10.**s(ii-1)
         dfluidmassc= cprof(ii-1)*dfluidmass
         fluidmass = fluidmass + dfluidmass
         fluidmassc= fluidmassc+ dfluidmassc
c        fluidmass = 1. - aa(2,ixtal+1)/star
c        fluidmassc = xc(jb)*fluidmass
        if (fluidmass .lt. 0.00000001) then
          xcfluid = 1.0
          xofluid = 0.0
        else
```

```
c        fluidmassc = cprof(jb)*fluidmass
       fluidmasso = fluidmass - fluidmassc
       xcfluid = (fluidmassc + deltamass)/fluidmass
       xofluid = 1. - xcfluid
      endif
       if (xcfluid .lt. cprof(ii)) goto 106
      enddo

106   continue
c      if ( ii.gt.jb ) ii=jb
      ii=ii-1
      if ( (ixtal+2).gt.jb ) then
       xcfluid = 1.0
       xofluid = 0.0
      endif

c
c      xc(ixtal) = xcnew
      cprof(ixtal) = xcnew

c      write(66,105) ixtal,jb,ii,fluidmass,fluidmassc,fluidmasso,xcnew,
c     1  xcfluid,xcinit(ixtal),10**s(ixtal)
105   format(3(i4,x),7(e12.5,2x))
      do i = ixtal+1, ii
c        xc(i) = xcfluid
        cprof(i) = xcfluid
      enddo
      do i = 1, jxnew
        xcprof(ixtal,i)=cprof(i)
      enddo
  300 continue


c      do j=1,jb
c        write(66,10) j,xcinit(j),cprof(j),xcprof(0,j),xcprof(18,j)
c      enddo
10    format(i4,x,4(e12.5,2x))

c the follwoing lines calculate the internal energy using the Lamb code
      write(*,*) 'calculating phase separation energy release'
        do i=1,jb-1
c   rho=10**aa(5,i)
c   temp=10**aa(4,i)
c   press=10**aa(6,i)
```

```
c   rad=10**aa(1,i)
c   radp1=10**aa(1,i+1)
          rho=10**dens(i)
          temp=10**t(i)
          press=10**p(i)
          rad=10**r(i)
          radp1=10**r(i+1)
          dmass(i)=4.*pi*rad**2*(radp1-rad)*rho
          ixtal = 2
          je=3
          call ieos(log10(temp),log10(rho),ixflag,je)
          uca     = temp3(ixtal,6)
          eca     = temp3(ixtal,9)
          etca    = temp3(ixtal,11)
          je=4
          call ieos(log10(temp),log10(rho),ixflag,je)
          uox     = temp3(ixtal,6)
          eox     = temp3(ixtal,9)
          etox    = temp3(ixtal,11)
          cvca = etca*10**eca*fnat
          cvox = etox*10**eox*fnat
          dudx(i)=(10**uca - 10**uox)/rho
        totmass=totmass+dmass(i)
        enddo
c      write(*,*) 'totmass =',totmass
      tottutot=0.0
      factor=1.e+46
      do ix=1,jxnew
        utot=0.0
        do i=1,jb-1
          dx=xcprof(ix,i)-xcprof(ix-1,i)
          dutot=dx*dudx(i)
          utot = utot + dmass(i)*dutot
c   if (ix.eq.1) write(66,12) i,dx,dudx(i),dmass(i),dutot,utot,
c     1      xcprof(ix,i),xcprof(ix-1,i)
        enddo
        phengy(ix)=utot
        tottutot=tottutot+utot
        totph(ix)=tottutot
c fmass=aa(2,ix)/star
        fmass=10**s(ix)
        xx(ix)=fmass
        yy(ix)=totph(ix)
c dphdm = (phengy(ix)-phengy(ix-1))/dmass(ix-1)
```

```
        dphdm(ix) = phengy(ix)/dmass(ix)
c write(66,13) ix,fmass,phengy(ix),totutot,dphdm(ix),dx,
c     1   xcprof(ix,ix),xcprof(ix,ix+1)
        write(66,13) ix,fmass,dmass(ix),phengy(ix)/factor,totutot/factor,
     1    dphdm(ix),xcprof(ix,ix),xcinit(ix)
      enddo

11    format(i4,x,f7.5,2x,3(e12.5,2x),2(f8.6,2x))
13    format(i4,x,f7.5,2x,6(e12.5,2x))
12    format(i4,x,7(e12.5,2x))

c Set up spline coefficients for phase-separation energy and composition
c composition profiles (routines from Press et al 1996)
      write(*,*) 'Settine up spline coefficients for phase-separation energy'
      write(*,*) 'and composition profiles'
      nxx = jxnew
      call xspline(xx,yy,nxx,1.d+30,1.d+30,yy2)

      do ixtal=1,nxx+1
        if (ixtal.eq.1) then
          massx(1)=0.0
        else
        massx(ixtal)=10**s(ixtal-1)
        endif
        do i=1,nxx
          massf(i)=10**s(i)
          xcp(ixtal,i)=xcprof(ixtal-1,i)
c   xcp(i,ixtal)=xcprof(ixtal-1,i)
        enddo
      enddo

500   continue

      if (jxold .eq. 0) then
          fmass1 = 0.0
        else
          fmass1=10**amxcold
      endif
      fmass2=10**amxc
      call xlocate(massx,nxx+1,fmass2,jcryst)
      write(*,*) 'jx jxold jcryst nxx jb',jx,jxold,jcryst,nxx,jb

      do n=1,nxx
        profile1(n)=xcp(jcryst,n)
```

```
          profile2(n)=xcp(jcryst+1,n)
        enddo
        big=1.03+30
        call xspline(massf,profile1,nxx,big,big,p1)
        call xspline(massf,profile2,nxx,big,big,p2)
        do n=1,jb
          fmass =  10**s(n)
          call xsplint(massf,profile1,p1,nxx,fmass,xcomp1)
          call xsplint(massf,profile2,p2,nxx,fmass,xcomp2)
          xcomp=xcomp1+(xcomp2-xcomp1)*(
     1      (fmass2-massx(jcryst))/(massx(jcryst+1)-massx(jcryst)) )
          if (xcomp.gt.1.0) xcomp=1.0
          if (xcomp.lt.0.0) xcomp=0.0
          xc(n)=xcomp
          if (sa(n).le.s(jb)) then
            fmassa= 10**sa(n)
          call xsplint(massf,profile1,p1,nxx,fmassa,xcomp1)
          call xsplint(massf,profile2,p2,nxx,fmassa,xcomp2)
          xcomp=xcomp1+(xcomp2-xcomp1)*(
     1        (fmass2-massx(jcryst))/(massx(jcryst+1)-massx(jcryst)) )
          if (xcomp.gt.1.0) xcomp=1.0
          if (xcomp.lt.0.0) xcomp=0.0
          xcxtal(n)=xcomp
          endif
108     format(5(e12.5,x))
        enddo

        norm=0.0
        totmass=0.0
        do n=1,jb-1
          rho=10**dens(n)
          rad=10**r(n)
          radp1=10**r(n+1)
          dmass(n)=4.*pi*rad**2*(radp1-rad)*rho
          totmass=totmass+dmass(n)
          norm=norm + dmass(n)*cv(n)*10**t(n)
        enddo
c        write(*,*) 'totmass = ',totmass

c calculate latent heat release due to partial crystallization
c of a shell and add it into enxtal2 in hopes of preventing numerical
c oscillations (MHM)
          rho=10**dens(jx)
          temp=10**t(jx)
```

```
          ixtal = 1
          je=3
          call ieos(log10(temp),log10(rho),ixflag,je)
          ucaliq     = temp3(ixtal,6)
          je=4
          call ieos(log10(temp),log10(rho),ixflag,je)
          uoxliq     = temp3(ixtal,6)
          ixtal = 2
          je=3
          call ieos(log10(temp),log10(rho),ixflag,je)
          uca     = temp3(ixtal,6)
          je=4
          call ieos(log10(temp),log10(rho),ixflag,je)
          uox     = temp3(ixtal,6)
          dlatentdm = (xc(jx)*(10**uca-10**ucaliq) +
     1            (1.-xc(jx))*(10**uox-10**uoxliq))/rho
        dlatent = -dlatentdm*star*(10**amxc-10**s(jx))
c artificially reduce the amount of latent heat by a factor of 5
        dlatent = dlatent/2.0

      dphdt(0)=0.0
      dphdp(0)=0.0
      enxtal2(0)=0.0
      deltam=1.e-05
      fmass2p=fmass2+deltam
        call xsplint(xx,yy,yy2,nxx,fmass1,energy1)
        call xsplint(xx,yy,yy2,nxx,fmass2,energy2)
        call xsplint(xx,yy,yy2,nxx,fmass2p,energy2p)
        erelease=energy2-energy1
c multiply by factor to correct for nonconstancy of \epsilon_{phase}
c        fc=(1.+.5*(10**bl-10**bla)/10**bl)
c why not use the "exact" expression for fc?
        fc=b(jb)/(.5*(b(jb)+10**bl))
c        fc=1.0
c erelease=erelease*fc
c erelease=erelease-dlatent
        dextaldm=(energy2p-energy2)/deltam
c erelease=(totph(jx)-totph(jxold))+dphdm(jx)*star*(10**amxc-10**s(jx))
c  try an alternate way of computing derivatives
       damxdp2=(4.*pi*log(10.)/(6.67d-8*star**2))*10**(p(jx)+4.*r(jx)-s(jx))
       deltat=.001
       dpfcdt=(phasec(t(jx)+deltat)-phasec(t(jx)))/deltat
       dpfodt=(phaseo(t(jx)+deltat)-phaseo(t(jx)))/deltat
       dpfdt = xc(jx)*dpfcdt + (1-xc(jx))*dpfodt
```

```
       damxdt2=-damxdp2*dpfdt
       damxdt=damxdt2
       damxdp=damxdp2
      do n=1,jx-1
        enxtal2(n)=0.0
        dphdp(n)=0.0
        dphdt(n)=0.0
      enddo
      do n=1,jb-1
c form=exp(-(dfloat((n-jx))/1.318)**2)
        anorm=3.5*dmass(jx)/star
        form1=exp(-((10**s(n)-10**amxc)/anorm)**2)
        form2=(dmass(n)/star)*form1/(sqrt(pi)*anorm)
c the following line subtracts out the latent heat from the entire core
        enxtal2(n)= -(cv(n)*10**t(n)/norm)*(fc*erelease+dlatent)
c this line adds in the latent heat contribution to the shells which
c are in the process of crystallizing (MHM), so there is no net contribution
        enxtal2(n)=enxtal2(n)+dlatent*form2/dmass(n)
        dphdt(n)  = -(cv(n)*10**t(n)/norm)*dextaldm*damxdt*form1
        dphdp(n)  = -(cv(n)*10**t(n)/norm)*dextaldm*damxdp*form1
c dphdt(n)  = -(cv(n)*10**t(n)/norm)*dphdm(n)*damxdt*star
c dphdp(n)  = -(cv(n)*10**t(n)/norm)*dphdm(n)*damxdp*star
        if (jx.eq.jxold) then
          dphdt(n)  = 0.0
          dphdp(n)  = 0.0
        endif
        ratio=enxtal2(n)/(cv(n)*10**t(n))
        en2spline(n)=enxtal2(n)
        xmass(n)=10**s(n)
c write(66,530) n,xca(n),xc(n),enxtal2(n),form2,dphdt(n),dphdp(n)
      enddo

      nxsp=jb-1
c      call xspline(xmass,en2spline,nxsp,big,big,en2dd)
c      call xsplint(xmass,en2spline,en2dd,nxsp,fmass,xcomp1)
      do n=1,jb
        if (sa(n).le.s(jb)) then
          fmassa=10**sa(n)
          call xsplint(xmass,en2spline,en2dd,nxsp,fmassa,xtal)
          enxtal2a(n)=xtal
        endif
      enddo

      ertot=0.0
```

```
      do i=1,jb-1
        ertot=ertot+enxtal2(i)*dmass(i)
      enddo
      write(*,111) '   ps energy released = ',-erelease
      write(*,111) ' latent heat released = ',dlatent
      write(*,111) 'total energy released = ',ertot
      Write(*,*) 'fc bl bla = ',fc,dlog10(b(jb)),bl
111   format(a,e12.5)
c      write(*,109) damxdt,damxdp,dphdt(jx),dphdp(jx)
c      write(*,110) damxdt2,damxdp2,dpfcdt,dpfodt,dpfdt
109   format('damxdt damxdp dphdt dphdp = ',4(e12.5,x))
110   format('damxdt2 damxdp2 dpfcdt dpfodt dpfdt = ',5(e12.5,x))
530   format(i3,x,6(e12.5,2x))

      print *, 'Exiting phasep2'
c      stop
      return
      end
```

```
c ****************************************************************************
      subroutine ephase(nshint)
      implicit double precision(a-h,o-z)
c..................................................................
c  calculate phase separation integral from Isern et al. (preprint,
c  March 5, 1997) MHM (May 1997)
c..................................................................
      double precision mu_e,kb,lsun,dmass(400),ratio(400),
     1  temperature(400),norm
      integer epflag1
      common/shells/ sa(400),ra(400),ba(400),pa(400),ta(400),
     1 ea(400),xca(400),fca(400),s(400),r(400),b(400),
     2 p(400),t(400),e(400),xc(400),sk(400),
     3 rk(400),bk(400),pk(400),tk(400)
      common/compold/xcold(400),xcn(400)
      common/density/dens(400),cv(400)
      common/phaseen/utot,totutot
      common/vca/sg,modnr
c      common/temp/s1,r1,s2,r2,b2,p2,t2,ea2,xc2,xo2,fca2,f2,q2,w2,c
c      common/xx/sin,sout,smid,grid1,grid2,ucent,cste,kon,kom
c      common/surf/u(2,3),v(2,3),ww(2,3),rm,bm,is,ks,ls,ms,kstart,npass
      common/xbnd/amxc,amxo,gold
c      common/d/ ml(3,70),nmax,kind,lmax,nsuff,nlim,nlim1,jjj,iter,lmam,
c     1 nlum,ko,nhp
      common/xenergy/enxtal(400),gtime

      common/prep/ aa(19,800), ecv(400), ext(400), exr(400),iprep
      common/epflag/epflag1
      integer nshint
      common/debug/debug
      common/once2/once2
      common/temp3/temp3(2,12)
      logical debug,once2

c      debug = .true.
      debug = .false.
      if (epflag1.eq.0) then
        once2 = .false.
        epflag1 = 1
      endif
      fnat = log10(exp(1.0))

      z1=6.
      a1=12.
```

```
      z2=8.
      a2=16.
      mu_e=2.
      kb=1.380658e-16
      uint=0.0
      utot=0.0
      pi=3.141592635
      rgas=8.3145e+07
      lsun=3.8268e+33
      totmass=0.0
      nel=nlim
      ntot=nlim+nshint

      write(*,*) 'Entering ephase.f'

      do n=1,nshint-1
        dx=xc(n)-xca(n)
c rho=10**(aa(5,n))
c temperature(n)=10**(aa(4,n))
c press=10**(aa(6,n))
c rad=10**(aa(1,n))
c radp1=10**(aa(1,n+1))
        temperature(n)=10**t(n)
        press=10**p(n)
        rad=10**r(n)
        radp1=10**r(n+1)
        rho=10**dens(n)
        gammae=(2.272e+05)*(rho/mu_e)**(1./3.)/temperature(n)
        fac=z1**(5./3.)/a1-z2**(5./3.)/a2
        duint=-.9*rgas*temperature(n)*gammae*dx*fac
        dmass(n)=4.*pi*rad**2*(radp1-rad)*rho
        totmass=totmass+dmass(n)
        dvol=4.*pi*rad**2*(radp1-rad)
        uint=uint+dmass(n)*duint

c the next lines calculate the internal energy using the Lamb code
        ixtal = 2
        je=3
        call ieos(dlog10(temperature(n)),dlog10(rho),ixflag,je)
        uca     = temp3(ixtal,6)
        eca     = temp3(ixtal,9)
        etca    = temp3(ixtal,11)
        je=4
        call ieos(dlog10(temperature(n)),dlog10(rho),ixflag,je)
```

```
        uox     = temp3(ixtal,6)
        eox     = temp3(ixtal,9)
        etox    = temp3(ixtal,11)
        cvca = etca*10**eca*fnat
        cvox = etox*10**eox*fnat
c        cv(n) = (xcn(n)*cvca + (1.-xcn(n))*cvox)
c cv(n) = aa(8,n)
c dutot=dvol*(xcn(n)*10**uca + (1.-xcn(n))*10**uox)
        dutot=dx*(10**uca - 10**uox)/rho
        utot = utot + dmass(n)*dutot
c write(63,10) rad,press,temperature(n),rho,xca(n),
c     1    xc(n),uca,uox

      enddo
10    format(8(e12.5,2x))
      norm=0.0
      if (utot.gt.0.0) utot=0.0
      do n=1,nshint-1
        norm=norm + dmass(n)*cv(n)*temperature(n)
      enddo
      do n=1,nshint-1
c the negative sign in the line below makes this a thermal energy *source*
        enxtal(n)=-(cv(n)*temperature(n)/norm)*utot
c enxtal(n)=enxtal(n)/1000.
c ratio(n)= log10(1.+abs(enxtal(n)/(cv(n)*temperature(n))))
        ratio(n)= enxtal(n)/(cv(n)*temperature(n))
c rad=10**(aa(1,n))
        rad=10**r(n)
c press=10**(aa(6,n))
        press=10**p(n)
        write(63,10) 10**s(n),press,temperature(n),10**dens(n),cv(n),
     1    xc(n),enxtal(n),ratio(n)
        xcold(n)=xcn(n)
      enddo
      toten=toten+uint
      totutot=totutot+utot
      write(63,*) 'phase separation energy this time step = ',uint
      write(63,*) 'total phase separation energy so far = ',totutot
      write(63,*) 'total integrated energy = ',utot
      write(*,*) 'ps energy released (analytic)  = ',uint
      write(*,*) 'ps energy released (Lamb code) = ',utot
      write(*,*) 'log luminosity = ',dlog10((dabs(utot)/10**gtime)/(3.826e+33))

      bl=dlog10(aa(3,ntot)/lsun)
```

```
      radius=aa(1,ntot)
c      write(*,*) 'lum radius = ', aa(3,ntot),radius
      tel=bl/4.-radius/2.+9.18458
      factor=1.e45
c      write(64,161) modnr,sg,p2,t2,ucent,radius,tel,bl,10.d0**amxc,
c     1  utot/factor,totutot/factor
161   format(i4,1p,e12.5,0p,f7.3,2f7.4,f8.4,f7.4,2f9.4,2x,e12.5,
     1  2x,e14.7)
      return
      end
```

2. Modifications to the Pulsation Codes

2.1. Description of Changes

The changes made in the pulsation code cjhanro.f, written by Carl Hansen, are fairly minor. In the new code, cjhxtal.f, all that has been done is to set $y1 = 0$ at the boundary between the solid core and the liquid above it. In essence, we have moved the inner boundary condition out from the center to a point determined by the crystallized mass fraction, which is read in from the file `period.dat`. Thus, the modes are excluded from the crystalline core in this approach. This approach was found to be completely justified for g-mode oscillations, and this code has been used to obtain almost all the pulsational results in this thesis.

The other pulsation code, cjhxbndy4.f, is also a modification of cjhanro.f, but with more extensive changes, as is shown by the table below. This code is more self-consistent in that it solves the problem of pulsation for the entire model, including the response of the crystallized core to the g-mode oscillations. I accomplished this by recasting the problem as one with modified boundary conditions at the solid/liquid interface. For a given frequency, I integrate the oscillation equations outward from the core to the solid/liquid interface, thus obtaining a relation between $y1$ and $y2$. This reduces the problem to the case described in the above paragraph. Instead of imposing $y1 = 0$ at the solid/liquid boundary, I impose the relation between $y1$ and $y2$ and allow the code to continue the integration out to the photosphere. The summary of the changes which I made to the different subroutines in cjhanro.f in order to accomplish this is given in the following listing.

rkfanro Reads in fracm. This is the crystallized mass fraction, which is given by the third entry on the first line of period.dat.

init Reads in extra quantities mu (μ) and alambda (λ) from tape29.dat. These are needed for pulsation of crystalline core in subroutine xbound.

xbound A new subroutine. Given $y1$ and a frequency, it returns the value of $y2$ at the solid/fluid interface, which is the self-consistent result of letting the crystal core respond to the perturbations.

load A new subroutine. It returns the central boundary conditions for oscillations of the crystalline core for the two possible independent solutions.

xbderiv A new subroutine. It returns the value of the RHS for the equations of oscillation of the crystalline core.

odeint A routine from Numerical Recipes, by Press et al. (1992). This routine does a Runge-Kutta integration of the equations in the crystalline core as specified in xbderiv. Also uses rkqs and rkck from Numerical Recipes.

bump Calls xbound, does full problem including discriminant calculation as well as actually iterating to a solution. We do this since the complete problem is now in the Cowling approximation, so we call bump both times.

grind Also calls xbound. grind is called only once. This routine is called after the solution has converged using bump, so that other auxiliary quantities may be calculated (still in the Cowling approximation).

In the following section, we give the source code for the three main routines which calculate the eigenfunction in the crystalline solid: **xbound**, **xbderiv**, and **load**.

2.2. Source Code

```
c*************************************************************************
      subroutine xbound(y1amp,y2amp)
      implicit double precision(a-h,o-z)
      parameter (nmax=50,nsav=200,vmax=50,EPS1=1.e-16)
      double precision xp(nsav),yp(vmax,nsav),EPS1
      common/misc/l,lhat,lindex,nsurf
      common/dmisc/period,grav,pi,pi4,p43,eps,verg,eig,eigt,y3i,y3t,
     1  amass
      common/crys/mu(650),alambda(650),delta(650),beta(650),
     1  rhos(650),rs(650),gs(650),xs(650),y5s(650),y2s(650),nxtal
      common/path/dxsav,xp,yp
      common/ipath/kmax,kount
      common/ray/iray
      common/saveval/y2ampold,eigtold,lold
      common/solid/ysol(2,200),xisol(200),eigen(2,200),ekinsol(200),nsol
      double precision mu
      double precision l,lhat,lindex
      double precision h1,hmin,y(nmax),y1(nmax),y2(nmax),
     1 yp1(vmax,nsav),yp2(vmax,nsav),ypsum(vmax,nsav),ysum(nmax)
      INTEGER nbad,nok
      EXTERNAL xbderiv,rkqs

c check to see if frequency has changed enough to warrant recalculating
c y2amp
      if ( abs((2.*pi/sqrt(eigt)-(2.*pi/sqrt(eigold)))).lt.200.
     1  .and. l.eq.lold .and. iray.ne.1 ) then
        y2amp=y2ampold
        return
      else
      nvar=4
      kmax=200
      dxsav=0.2
      x1=xs(1)
      x2=xs(nxtal)
      h1=(x2-x1)/100.
      hmin=0.
c solve for first soln (z goes like r**(l-2))
      call load(1,y)
      call odeint(y,nvar,x1,x2,EPS1,h1,hmin,nok,nbad,xbderiv,rkqs)
      do i=1,nvar
        y1(i)=y(i)
        do j=1,kount
```

```
          yp1(i,j)=yp(i,j)
        enddo
      enddo
c      write(*,*) 'y1',(y1(i),i=1,nvar)
c      write(*,10) (xp(i),yp(1,i),yp(2,i),yp(3,i),yp(4,i),i=1,kount)
c solve for second soln (z goes like r**l)
      call load(2,y)
      call odeint(y,nvar,x1,x2,EPS1,h1,hmin,nok,nbad,xbderiv,rkqs)
      do i=1,nvar
        y2(i)=y(i)
        do j=1,kount
          yp2(i,j)=yp(i,j)
        enddo
      enddo
c add solutions to make y4=0 and y1=1 at the solid/fluid interface
      den=y1(1)*y2(4)-y2(1)*y1(4)
      a1=y2(4)/den
      a4p=-y1(4)/den
      do j=1,kount
       do i=1,nvar
         ypsum(i,j)=a1*yp1(i,j)+a4p*yp2(i,j)
       enddo
      enddo
      do i=1,nvar
        ysum(i)=a1*y1(i)+a4p*y2(i)
      enddo
c      write(*,*) 'x2 ysum',x2,(ysum(i),i=1,nvar)

c      write(*,10) (xp(i),ypsum(1,i),ypsum(2,i),ypsum(3,i),ypsum(4,i),
c     1  i=1,kount)
10    format(5(e14.7,x))
      alamliq=alambda(nxtal+1)+(2./3.)*mu(nxtal+1)
c      y2amp=y1amp*(1.-mu(1)*ysum(2)/(alamliq*y2s(nxtal)))
      y2amp=y1amp*(ysum(1)-mu(1)*ysum(2)/(alamliq*y2s(nxtal)))
      y2ampold=y2amp
      eigold=eigt
      lold=l
      write(*,*) 'calculating solid/liquid boundary'

c store final solution in ysol and convert to Dziembowski variables
      if (iray.eq.1) then
        write(*,*) 'storing eigenfunction ysol'
        nsol=kount
        do i=1,kount
```

```
         xx=xp(i)
         call xlocate(xs,nsurf,xx,j)
         if (j.gt.nxtal) then
           write(*,*) 'went past crystallized layer: stop'
           stop
         endif
         g1=gs(j)+(xx-xs(j))*(gs(j+1)-gs(j))/(xs(j+1)-xs(j))
         r1=rs(j)+(xx-xs(j))*(rs(j+1)-rs(j))/(xs(j+1)-xs(j))
         rho1=rhos(j)+(xx-xs(j))*(rhos(j+1)-rhos(j))/(xs(j+1)-xs(j))
         y51=  y5s(j)+(xx-xs(j))*( y5s(j+1)- y5s(j))/(xs(j+1)-xs(j))
        xisol(i)=xp(i)
        rfac=1./r1**lindex
        ysol(1,i)=ypsum(1,i)*rfac
        ysol(2,i)=(ypsum(3,i)*eig*r1/g1)*rfac
        eigen(1,i)=r1*ysol(1,i)
        eigen(2,i)=(g1*ysol(2,i)/eig)
ekinsol(i)=rho1*r1**3*y51*(eigen(1,i)**2+lhat*eigen(2,i)**2)/1.d+40
c ekinsol(i)=y51
c write(*,15) y5s(j),y5s(j+1),y51
15      format(3(e12.5,x))
        enddo
      endif

      endif
      write(*,*) 'l per y1liq y2liq',l,2.*pi/sqrt(eigt),y1amp,y2amp

c      stop
      return
      end
```

```
c*********************************************************************
      subroutine xbderiv(xx,yy,dyy)
      implicit double precision(a-h,o-z)
      parameter (nmax=10)
      dimension yy(nmax),dyy(nmax)
      common/misc/l,lhat,lindex,nsurf
      common/dmisc/period,grav,pi,pi4,p43,eps,verg,eig,eigt,y3i,y3t,
     1  amass
      common/crys/mu(650),alambda(650),delta(650),beta(650),
     1  rhos(650),rs(650),gs(650),xs(650),y5s(650),y2s(650),nxtal
      double precision mu,mu1,lam1
      double precision l,lhat,lindex

      call xlocate(xs,nsurf,xx,j)
      if (j.gt.nxtal) then
        write(*,*) 'went past crystallized layer: stop'
        stop
      endif
      rho1=rhos(j)+(xx-xs(j))*(rhos(j+1)-rhos(j))/(xs(j+1)-xs(j))
      g1=gs(j)+(xx-xs(j))*(gs(j+1)-gs(j))/(xs(j+1)-xs(j))
      r1=rs(j)+(xx-xs(j))*(rs(j+1)-rs(j))/(xs(j+1)-xs(j))
      mu1=mu(j)+(xx-xs(j))*(mu(j+1)-mu(j))/(xs(j+1)-xs(j))
      lam1=alambda(j)+(xx-xs(j))*(alambda(j+1)-alambda(j))/(xs(j+1)-xs(j))
      delta1=delta(j)+(xx-xs(j))*(delta(j+1)-delta(j))/(xs(j+1)-xs(j))
      beta1=beta(j)+(xx-xs(j))*(beta(j+1)-beta(j))/(xs(j+1)-xs(j))
      y51=y5s(j)+(xx-xs(j))*(y5s(j+1)-y5s(j))/(xs(j+1)-xs(j))
c      anorm1=alambda(nxtal)*y2s(nxtal)
c      anorm2=mu(nxtal)/rs(nxtal)
      anorm1=mu(1)
      anorm2=mu(1)

      dyy(1)=y51*(-(1.+2.*lam1*delta1-lindex)*yy(1)+delta1*yy(2)*anorm1+
     1  lam1*lhat*delta1*yy(3))
      dyy(2)=y51*( (-eigt*rho1*r1**2-4.*rho1*g1*r1 +
     1  4.*pi*grav*rho1**2*r1**2+4.*mu1*beta1*delta1)*yy(1)/anorm1 -
     2 (4.*mu1*delta1-lindex)*yy(2) +
     3 lhat*(rho1*g1*r1-2.*mu1*beta1*delta1)*yy(3)/anorm1
     4 + lhat*yy(4)*anorm2/anorm1 )
      dyy(3)=y51*( -1.*yy(1)+lindex*yy(3)+(1./mu1)*yy(4)*anorm2 )
      dyy(4)=y51*( (rho1*g1*r1-2.*mu1*beta1*delta1)*yy(1)/anorm2 -
     1  lam1*delta1*yy(2)*anorm1/anorm2 +
     2  (-rho1*eigt*r1**2+2.*mu1*delta1*(lam1*(2.*lhat-1.) +
     3  2.*mu1*(lhat-1.)))*yy(3)/anorm2 + (lindex-3.)*yy(4) )
c      write(*,10) rho1*g1*r1,mu1*beta1*delta1,lam1*delta1,anorm1,anorm2
```

```
10    format(5(e12.5,x))
      return
      end
```

```
c***********************************************************************
      subroutine load(iflag,y)
      implicit double precision(a-h,o-z)
      double precision mu,y(4)
      common/crys/mu(650),alambda(650),delta(650),beta(650),
     1  rhos(650),rs(650),gs(650),xs(650),y5s(650),y2s(650),nxtal
      common/misc/l,lhat,lindex,nsurf
      double precision l,lhat,lindex,muc,lamc

      muc=mu(1)
      lamc=alambda(1)
      if (iflag.eq.1) then
        y(1)=1.0
c        y(2)=2.*(-1. + l)*muc
        y(2)=2.*(-1. + l)
        y(3)=1./l
c        y(4)=2.*(-1. + l)*muc/l
        y(4)=2.*(-1. + l)/l
      elseif (iflag.eq.2) then
c        y(1)=(1. + l)*(l*lamc - 2.*muc + l*muc)/
c     1   (2.*muc*(2.*l*lamc + l**2*lamc - muc + 2.*l*muc + l**2*muc))
        y(1)=(1. + l)*(l*lamc - 2.*muc + l*muc)/
     1   (2.*(2.*l*lamc + l**2*lamc - muc + 2.*l*muc + l**2*muc))
        y(2)=(1. + l)*(-3*lamc - l*lamc + l**2*lamc - 2.*muc - l*muc
     1   + l**2*muc)/(2.*l*lamc + l**2*lamc - muc + 2.*l*muc + l**2*muc)
c        y(3)=(3*lamc + l*lamc + 5*muc + l*muc)/
c     1   (2.*muc*(2.*l*lamc + l**2*lamc - muc + 2.*l*muc + l**2*muc))
        y(3)=(3*lamc + l*lamc + 5*muc + l*muc)/
     1   (2.*(2.*l*lamc + l**2*lamc - muc + 2.*l*muc + l**2*muc))
        y(4)=1.
      else
        write(*,*) 'unable to set inner BCs in load'
        stop
      endif
      return
      end
```

3. Modifications to WDEC—Paul's Version

3.1. Code Changes

The modifications to Paul's version of the WDEC are quite minor. The only notable change is the added ability to converge to a pre-specified set of temperatures.

This modified version of WDEC is called `wdxdfit.f` and uses the control file `temperatures.con`. This file contains a list of temperatures (one on a line) for which the code is supposed to produce models. An example of this file is the following:

```
13400.0
13200.0
13000.0
12800.0
12600.0
12400.0
```

Using this file, WDEC will attempt to produce 6 models, with the last model having $T_{\rm eff} = 12400$ K.

There are two instances in which this is a desirable capability to have. First, if one wants to produce a model at a given temperature (to match spectroscopic determinations, say), then this is a convenience. Second, if one wants to produce a grid of models such that "nearby" models differ in only one of the parameters, then it is necessary to hold all the other parameters constant. For instance, if we wish to explore the effect of $M_\star$ and $M_{\rm H}$ on the pulsations, but wish to fix the temperature at $T_{\rm eff} = 11800$ K, then we also need this capability. In addition, it is easier to produce an evenly spaced grid of models in temperature.

It is not always possible to converge to the desired temperature if the model is badly off the equation of state near a particular temperature. When this happens, there may not be a linear relation between small changes in the timestep Δt and small changes in $T_{\rm eff}$. If this is the case, then `wdxdfit.f` may become trapped in a periodic trek through the space of Δt and $T_{\rm eff}$ and never converge to the desired solution. In the present version of this code, the only way out of this is to type `^C`.

3.2. Extensions to the Envelope EOS's

Since most of the models used in the pulsational part of this thesis are designed to apply to high mass DAV's, the conditions in the envelopes of our models were in general at higher densities than for 0.6 $M_\odot$ models. As a result, we were closer to the edges of our equations of state, and in some cases we were off them.

In order to calculate g-mode periods, the most important quantity is the Brunt-Väisälä frequency. Fortunately, the Brunt-Väisälä frequency is such a sensitive function of the equilibrium quantities that any irregularities in it give an instant diagnostic clue as to what is going on. By examining the Brunt-Väisälä frequency, we found that we were off the envelope EOS (EEOS) for both C and He when we assumed thick He layers (i.e., 10^{-3}) for our 1.1 $M_\odot$ models. In addition, we found entries in the EOS for both He and H for which the thermodynamic quantities χ_ρ and χ_T were artificially set to zero, which effectively rendered these grid points useless.

In order to treat both these problems, we used the Lamb interior EOS to extend and correct the envelope tables. This is justified since all the changes and additions were to the high density edge of the envelope EOS's, so the approximations assumed by the interior EOS should be valid there.

In Figure E.1, we plot the various EEOS regions, as well as the interior EOS region for oxygen, denoted by IEOSO. The solid histogram lines in the first three panels, labelled EEOSH, EEOSHE, and EEOSC, correspond to the limiting region in which the envelope EOS is defined for H, He, and C, respectively. The dashed line corresponds to the region in which the EOS's were defined before our extensions. The fourth panel, labeled IEOSO, gives the region in which the interior EOS of O is defined. In all the panels, the curve which is drawn shows the points covered by a typical 1.1 $M_\odot$ model with $T_{\rm eff} \sim 12,000$ K; when this curve is inside the 0.99 mass point in the model it is drawn as a dotted line, and when it is outside this point it is drawn as a solid line. Thus, we see that if we choose the core/envelope boundary to be at this mass point, then we would have been unable to treat the envelope properly for C, HE, and even H, if these elements were present at the base of the envelope.

In the following section, we give the source code for the program with which we made the extensions, **eos_extend.f**. It is a front end for the Lamb EOS code which reads in the old EOS tables from standard input and writes the extended tables to standard output. Additional documentation is given at the top of the source code itself.

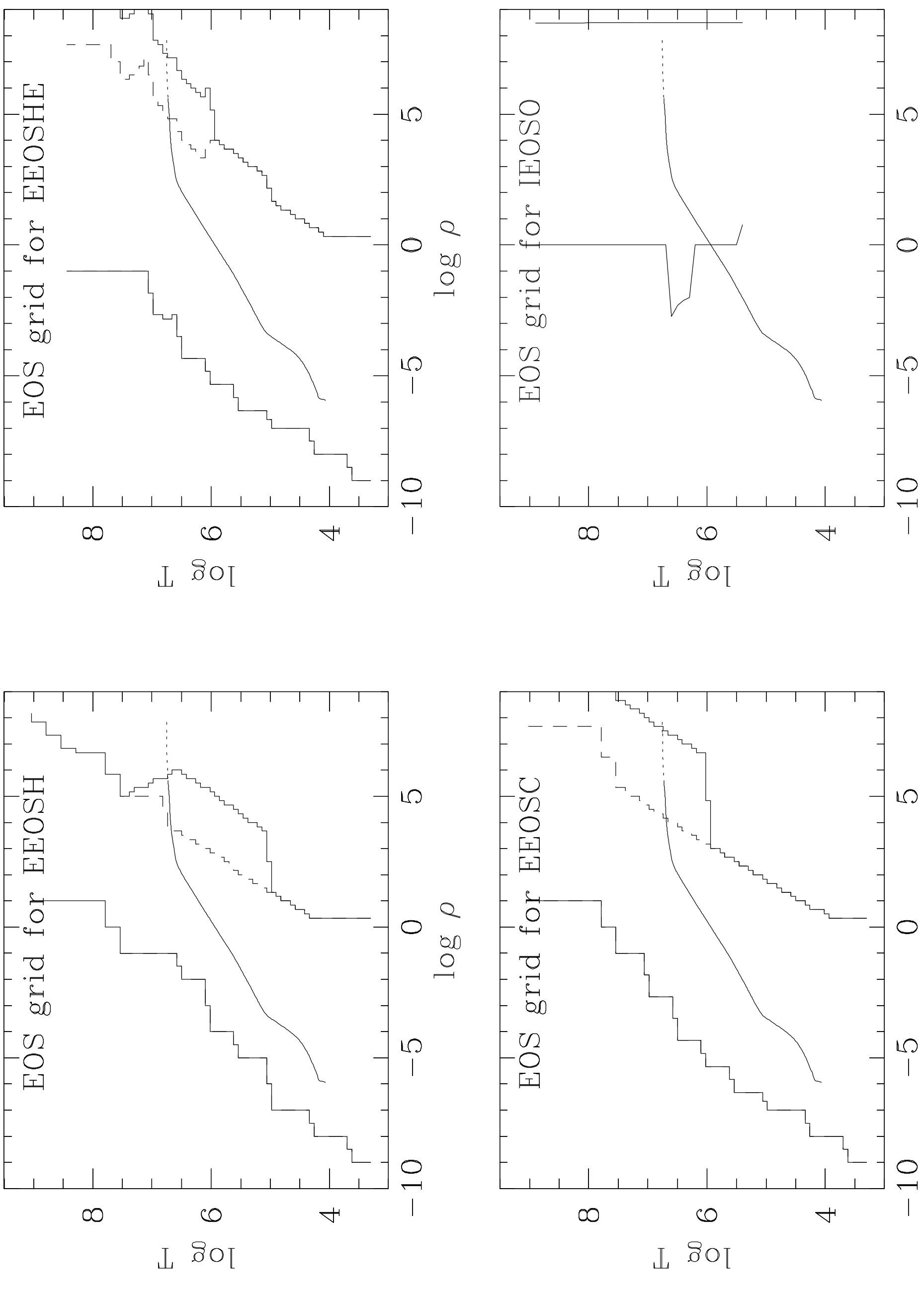

Fig. E.1.— The regions spanned by the various envelope and interior equations of state.

3.3. Source Code

```
c********************************************************************
c Extend the envelope equations of state for hydrogen, helium, and
c carbon using the Lamb ieos code. These extensions are to the high
c density edges of the eos's, so the Lamb code should be valid there.
c The program reads in the files (EEOSH.orig, EEOSHE.orig, EEOSC.orig)
c from standard input and writes the extended eos to standard output.
c je=1,2,3 for H,He,C, respectively. rhoadd is the orders of magnitude
c in extension to make to the eos's, and tthresh is the log T above
c which to make this extensions. Nothing is done to the part of the
c tables with log T < tthresh. The Lamb ieos code is included as
c the subroutine ieos(). In addition, this code replaces lines in the
c eos which had \Chi_T and \Chi_rho = 0; these quantities are necessary
c for the healthy functioning of wdxdl and wdxdfit. This was mainly
c necessary at the high density edges of the eos's or in the regions where
c the eos's had already been extended once before, at high temperatures.
c********************************************************************
      program eos_extend
      implicit double precision(a-h,o-z)
      double precision a(100,8)

      tthresh=6.0
      drho=1./3.
c      rhoadd=3.0
      rhoadd=2.0
      nadd=nint( rhoadd/drho +1.)
c je=1 for hydrogen je=2 for helium and je=3 for carbon
      je=1
c      je=2
c      je=3

      read (*,*) nisot
      write(*,5) nisot
5     format(i5)
      do i=1,nisot
        read (*,*) nisobar
        newiso=nisobar+nadd
c        write(*,5) newiso
        do j=1,nisobar
          read(*,*) (a(j,k),k=1,8)
c          write(*,10) (a(j,k),k=1,8)
        enddo
        t=a(nisobar,1)
```

```
        if (t.gt.tthresh) then
          write(*,5) newiso
          do j=1,nisobar
            if (dabs(a(j,4)).lt.1.d-06) then
c         write(*,*) 'Adding line'
              call testeos(a(j,1),a(j,2),a(j,2),drho,je)
            else
              write(*,10) (a(j,k),k=1,8)
            endif
          enddo
          rhomin=a(nisobar,2)+drho
c     rhomin=a(nisobar,2)
          rhomax=rhomin+rhoadd
c   write(*,*) 'Adding the following',nadd,' lines:'
          call testeos(t,rhomin,rhomax,drho,je)
        else
          write(*,5) nisobar
          do j=1,nisobar
            if (dabs(a(j,4)).lt.1.d-06) then
c       write(*,*) 'Adding line'
              call testeos(a(j,1),a(j,2),a(j,2),drho,je)
            else
              write(*,10) (a(j,k),k=1,8)
            endif
          enddo
        endif
c write(*,10) (a(nisobar,k),k=1,8)
10      format(8(x,1pe12.5))
      enddo
      stop
      end
```

```
c***********************************************************************
      subroutine testeos(t,rhomin,rhomax,drho,je)
      implicit double precision(a-h,o-z)
      common/debug/debug
      common/vars/x,efermi,beta,eta0,theta,gamma,phi,rho0
      common/once/once
      common/temp/temp(2,12)
      logical debug,once

      debug = .true.
      once = .false.
      ixflag = 0
      fnat = log10(exp(1.0))

      ixtal=1
      do d=rhomin,rhomax+0.001,drho
        call ieos(t,d,ixflag,je)
        p      =temp(ixtal,1)
        pd     =temp(ixtal,4)
        pt     =temp(ixtal,5)
        u     = temp(ixtal,6)
        ud    = temp(ixtal,7)
        ut    = temp(ixtal,8)
        e     = temp(ixtal,9)
        ed    = temp(ixtal,10)
        et    = temp(ixtal,11)
        eta    = temp(ixtal,12)
c cv = et*10**e*fnat
        cv = et*10**e
        chirho=pd
        chit=pt
        vt=chit/chirho
        gamma3=1+chit*10**(p-d-t)/cv
        gamma1=chirho+chit*(gamma3-1)
        datg=(gamma3-1.)/gamma1
        write(*,201)t,d,p,u,chit,chirho,datg,eta
      enddo
c        write(*,200) (temp(ixtal,i),i=1,12)
200     format(2(x,f4.2),11(x,1pe12.5),x,i2)
201     format(11(x1pe12.5),x,i2)
c201     format(2(x,f4.2),11(x,1pe12.5),x,i2)

      end
```

Bibliography

Abrikosov, A. A. 1960, Zh. Eksp. i Teor. Fiz, 39, 1798

Aizenman, M., Smeyers, P., & Weigert, A. 1977, A&A, 58, 41

Alterman, Z., Jarosch, H., & Pekeris, C. L. 1959, Proc. Roy. Soc., A, 252, 80

Barrat, J. L., Hansen, J. P., & Mochkovitch, R. 1988, A&A, 199, L15

Bergeron, P., Wesemael, F., Lamontagne, R., Fontaine, G., Saffer, R. A., & Allard, N. F. 1995, ApJ, 449, 258

Bildsten, L. & Cutler, C. 1995, ApJ, 449, 800

Bradley, P. A. 1993, PhD thesis, The University of Texas at Austin

Bradley, P. A. 1996, ApJ, 468, 350

Bradley, P. A. & Winget, D. E. 1994a, ApJ, 430, 850

Bradley, P. A. & Winget, D. E. 1994b, ApJ, 421, 236

Bradley, P. A., Winget, D. E., & Wood, M. A. 1993, ApJ, 406, 661

Brassard, P., Fontaine, G., Wesemael, F., & Hansen, C. J. 1992, ApJS, 80, 369

Brassard, P., Fontaine, G., Wesemael, F., Kawaler, S. D., & Tassoul, M. 1991, ApJ, 367, 601

Brassard, P., Fontaine, G., & Wesemael, F. 1995, ApJS, 96, 545

Brickhill, A. J. 1991a, MNRAS, 251, 673

Brickhill, A. J. 1991b, MNRAS, 252, 334

Burkert, A., Truran, J. W., & Hensler, G. 1992, ApJ, 391, 651–658

Canuto, V. M. & Dubovikov, M. 1998, ApJ, 493, 834

Canuto, V. M., Goldman, I., & Mazzitelli, I. 1996, ApJ, 473, 550

Chaboyer, B., Demarque, P., Kernan, P. J., & Krauss, L. M. 1998, ApJ, 494, 96

Chabrier, G. 1998, In Proceedings of IAU Symposium 189 on Fundamental Stellar Properties: The Interaction between Observation and Theory, ed. T. R. Bedding, A. J. Booth, & J. Davis, volume 189 (Dordrecht: Kluwer), 381

Chabrier, G., Segretain, L., Hernanz, M., Isern, J., & Mochkovitch, R. 1993, In White Dwarfs: Advances in Observation and Theory, ed. M. A. Barstow (Dordrecht: Kluwer Academic Publishers), 115

Chandrasekhar, S. 1939, An Introduction to the Study of Stellar Structure (Chicago: University of Chicago Press)

Chiappini, C., Matteucci, F., & Gratton, R. 1997, ApJ, 477, 765

Claver, C. F. 1995, PhD thesis, The University of Texas at Austin

Clemens, J. C. 1993, PhD thesis, The University of Texas at Austin

Clemens, J. C. 1995, Baltic Astronomy, 4, 142

Cowling, T. G. 1941, MNRAS, 101, 367

Crossley, D. J. 1975, Geophys. J. Roy. Astr. Soc., 41, 153

D'Antona, F. & Mazzitelli, I. 1978, A&A, 66, 453

D'Antona, F. & Mazzitelli, I. 1989, ApJ, 347, 934

Epstein, I. 1950, ApJ, 112, 6

Gabriel, M. & Scuflaire, R. 1979, Acta Astronomica, 29, 135

García-Berro, E., Hernanz, M., Isern, J., Chabrier, G., Segretain, L., & Mochkovitch, R. 1996, Astronomy and Astrophysics Supplement Series, 117, 13

García-Berro, E., Hernanz, M., Mochkovitch, R., & Isern, J. 1988, A&A, 193, 141

Garnavich, P. M., Kirshner, R. P., Challis, P., Tonry, J., Gilliland, R. L., Smith, R. C., Clocchiatti, A., Diercks, A., Filippenko, A. V., Hamuy, M., Hogan, C. J., Leibundgut, B., Phillips, M. M., Reiss, D., Riess, A. G., Schmidt, B. P., Schommer, R. A., Spyromilio, J., Stubbs, C., Suntzeff, N. B., & Wells, L. 1998, ApJ, 493, L53

Goosens, M. & Smeyers, P. 1974, Ap&SS, 26, 137

Gradshteyn, I. S. & Ryzhik, I. M. 1980, Table of Integrals, Series, and Products (San Diego, New York, Berkeley, Boston, London, Sydney, Tokyo, Toronto: Academic Press, Inc.)

Hamada, T. & Salpeter, E. E. 1961, ApJ, 134, 683

Hansen, C. J. & Van Horn, H. M. 1979, ApJ, 233, 253

Hernanz, M., García-Berro, E., Isern, J., Mochkovitch, R., Segretain, L., & Chabrier, G. 1994, ApJ, 434, 652

Höflich, P., Wheeler, J. C., & Thielemann, F. K. 1998, ApJ, 495, 617

Iben, I., J. & Macdonald, J. 1985, ApJ, 296, 540

Iben, I., J. & Tutukov, A. V. 1984, ApJ, 282, 615

Ichimaru, S., Iyetomi, H., & Ogata, S. 1988, ApJ, 334, L17

Iglesias, C. A. & Rogers, F. J. 1993, ApJ, 412, 752

Isern, J., Mochkovitch, R., García-Berro, E., & Hernanz, M. 1997, ApJ, 485, 308

Kanaan, A. N. 1996, PhD thesis, The University of Texas at Austin

Kanaan, A., Kepler, S. O., Giovannini, O., & Diaz, M. 1992, ApJ, 390, L89

Kawaler, S. D., Winget, D. E., & Hansen, C. J. 1985, ApJ, 295, 547

Kepler, S. O., Nather, R. E., & Metcalfe, T. S. 1998, Baltic Astronomy, 7, 175

Kirzhnits, D. A. 1960, Soviet Phys.—JETP, 11, 365

Klumpe, E. W. 1995, Masters thesis, The University of Texas at Austin

Lamb, D. Q. & Van Horn, H. M. 1975, ApJ, 200, 306

Lamontagne, R., Wesemael, G., Fontaine, G., & Demers, S. 1997, In White Dwarfs, Proceedings of the 10th European Workshop on White Dwarfs, ed. J. Isern, M. Hernanz, & E. García-Berro (Dordrecht, Boston, London: Kluwer Academic Publishers), 143

Landau, L. D. & Lifshitz, E. M. 1975, Theory of Elasticity (Oxford, New York, Toronto, Sydney, Paris, Braunschweig: Pergamon Press)

Liebert, J., Dahn, C. C., & Monet, D. G. 1988, ApJ, 332, 891

Mazzitelli, I. & D'Antona, F. 1986, ApJ, 308, 706

McDermott, P. N., Van Horn, H. M., & Hansen, C. J. 1988, ApJ, 325, 725

Mestel, L. 1952, MNRAS, 112, 583

Mestel, L. & Ruderman, M. A. 1967, MNRAS, 136, 27

Metcalfe, T. S. 1998, Masters thesis, The University of Texas at Austin

Mochkovitch, R. 1983, A&A, 122, 212

Ogata, S. & Ichimaru, S. 1987, Phys. Rev. A, 36, 5451

Oswalt, T. D., Smith, J. A., Wood, M. A., & Hintzen, P. 1996, Nature, 382, 692

Press, W. H., Teukolsky, S. A., Vetterling, W. T., & Flannery, B. P. 1992, Numerical Recipes in Fortran 77 (Cambridge, New York, Melbourne: Cambridge University Press)

Provencal, J. L., Shipman, H. L., Hog, E., & Thejll, P. 1998, ApJ, 494, 759

Riess, A. G., Nugent, P., Filippenko, A. V., Kirshner, R. P., & Perlmutter, S. 1998, ApJ, 504, 935

Robinson, E. L., Mailloux, T. M., Zhang, E., Koester, D., Stiening, R. F., Bless, R. C., Percival, J. W., Taylor, M. J., & Van Citters, G. W. 1995, ApJ, 438, 908

Robinson, E. L., Kepler, S. O., & Nather, R. E. 1982, ApJ, 259, 219

Salaris, M., Dominguez, I., García-Berro, E., Hernanz, M., Isern, J., & Mochkovitch, R. 1997, ApJ, 486, 413

Salpeter, E. 1961, ApJ, 134, 669

Schmidt, M. 1959, ApJ, 129, 243

Schwank, D. C. 1976, Ap&SS, 43, 459

Schwarzschild, K. 1958, Structure and Evolution of the Stars (Princeton: Princeton University Press)

Segretain, L. & Chabrier, G. 1993, A&A, 271, L13

Segretain, L., Chabrier, G., Hernanz, M., García-Berro, E., Isern, J., & Mochkovitch, R. 1994, ApJ, 434, 641

Shu, F. S. 1992, The Physics of Astropysics: vol. II Gas Dynamics (Mill Valley, CA: University Science Books)

Stevenson, D. J. 1977, Proc. Ast. Soc. Australia, 3, 167

Stevenson, D. J. 1980, J. Phys. Suppl., 41, C2–61

Unno, W., Osaki, Y., Ando, H., Saio, H., & Shibihashi, H. 1989, Nonradial Oscillations of Stars (Tokyo: University of Tokyo Press)

Van Horn, H. M. 1968, ApJ, 151, 227

Van Horn, H. M. & Savedoff, M. P. 1976, In Proceedings of Solar and Stellar Pulsation Conference, ed. A. N. Cox & R. G. Deupree (LASL Report: LA-6544-C), 109

Van Kerkwijk, M. H., Clemens, J. C., Wu, Y. Q., & Kleinman, S. J. 1997, IAU Symposia, 185, E86

Weidemann, V. & Koester, D. 1983, A&A, 121, 77

Weidemann, V. & Yuan, J. W. 1989, In White dwarfs; Proceedings of IAU Colloquium 114th, Hanover, NH, ed. G. Wegner (Berlin, New York: Springer-Verlag), 1

Winget, D. E., Hansen, C. J., Liebert, J., Van Horn, H. M., Fontaine, G., Nather, R. E., Kepler, S. O., & Lamb, D. Q. 1987, ApJ, 315, L77

Winget, D. E., Kepler, S. O., Kanaan, A., Montgomery, M. H., & Giovannini, O. 1997, ApJ, 487, L191

Winget, D. E., Nather, R. E., Clemens, J. C., Provencal, J., Kleinman, S. J., Bradley, P. A., Wood, M. A., Claver, C. F., Frueh, M. L., Grauer, A. D., Hine, B. P., Hansen, C. J., Fontaine, G., Achilleos, N., Wickramasinghe, D. T., Marar, T. M. K., Seetha, S., Ashoka, B. N., O'Donoghue, D., Warner, B., Kurtz, D. W., Buckley, D. A., Brickhill, J., Vauclair, G., Dolez, N., Chevreton, M., Barstow, M. A., Solheim, J. E., Kanaan, A., Kepler, S. O., Henry, G. W., & Kawaler, S. D. 1991, ApJ, 378, 326

Winget, D. E., Nather, R. E., Clemens, J. C., Provencal, J. L., Kleinman, S. J., Bradley, P. A., Claver, C. F., Dixson, J. S., Montgomery, M. H., Hansen, C. J., Hine, B. P., Birch, P., Candy, M., Marar, T. M. K., Seetha, S., Ashoka, B. N., Leibowitz, E. M., O'Donoghue, D., Warner, B., Buckley, D. A. H., Tripe, P., Vauclair, G., Dolez, N., Chevreton, M., Serre, T., Garrido, R., Kepler, S. O., Kanaan, A., Augusteijn, T., Wood, M. A., Bergeron, P., & Grauer, A. D. 1994, ApJ, 430, 839

Winget, D. E., Van Horn, H. M., & Hansen, C. J. 1981, ApJ, 245, L33

Wood, M. 1993, Bull. American Astron. Soc., 183, 5002

Wood, M. 1995, In White Dwarfs: Proceedings of the 9th European Workshop on White Dwarfs, ed. D. Koester & K. Werner (Berlin, Heidelberg: Springer-Verlag), 41

Wood, M. A. 1990, PhD thesis, The University of Texas at Austin

Wood, M. A. 1992, ApJ, 386, 539–561

Wood, M. A. & Oswalt, T. D. 1998, ApJ, 497, 870

Wood, M. A. & Winget, D. E. 1989, In White dwarfs; Proceedings of IAU Colloquium 114th, Hanover, NH, ed. G. Wegner (Berlin, New York: Springer-Verlag), 282

Wu, Y. 1997, PhD thesis, California Institute of Technology

Xu, Z. W. & Van Horn, H. M. 1992, ApJ, 387, 662

Vita

Michael Houston Montgomery was born in Nashville, Tennessee, on May 10, 1966, the son of James Houston Montgomery and Lois Lee Montgomery. After graduating from Victoria High School, Victoria, Texas, in 1984, he attended The University of Texas at Austin, graduating with a Bachelor of Science in Physics in May, 1988 and receiving a National Science Foundation Graduate Fellowship. He attended the Department of Physics at Princeton University in the Fall of 1988, and received a Master of Arts in 1992. In the Fall of 1992, he entered the Department of Astronomy at The University of Texas at Austin. He received a Master of Arts in Astronomy from The University of Texas at Austin in 1994.

Permanent address: 11206 Hidden Bluff Dr.
Austin, Texas 78754

This dissertation was typeset with LaTeX[‡] by the author.

[‡]LaTeX is a document preparation system developed by Leslie Lamport as a special version of Donald Knuth's TeX Program.